KU LEUVEN

FACULTY OF SCIENCE

Micro-SQUIDs with controllable weak links via electromigration

Wout KEIJERS

Supervisor: prof. dr. J. Van de Vondel
Mentor: V. Zharinov

Thesis presented in
fulfillment of the requirements
for the degree of Master of Science
in Physics

Academic year 2016-2017

Acknowledgments

First and foremost I would like to thank my supervisor, Joris Van de Vondel, for entrusting me to fly solo into this uncharted research territory. Even though this led to an abundance of questions on my side, meaning more work for him, he was always eager to discuss the matter at hand. For this I admire Joris' patience, when I was bothering him with my obvious questions. His joy and enthusiasm for experimental physics was contagious and even motivational for me. I am thankful for the excellent example he has provided as a physicist and professor.

In addition, I would like to express my great appreciation to my daily advisor, Vyacheslav Zharinov, for his guidance, his incomparable expertise in electromigration and our enjoyable academic and non-academic discussions.

The next in line to thank is Jeroen Scheerder, for everything he has done for me during my master thesis work. His help ranged from the frequent search for the 'always-seem-to-be-lost' banana plugs to assistance in academic writing. As I am starting the pursuit of a PhD in a few months, Jeroen has been a commendable example as an exemplary PhD student. In case my PhD pursuit leads me to functionalized graphene, I would be humbled and honored to follow in his footsteps.

Many thanks to Xavier Baumans and Joseph Lombardo, for their expertise and guidance during the experiments conducted in Liège.

Furthermore, I would like to express my gratitude to the readers of my thesis, for taking time out from their busy schedule to serve as my external reader.

Also, the other members of the group of Joris Van de Vondel, Tomas and Ritika, with whom I had the pleasure of working: I truly appreciate the helpful discussions and the suggestions provided.

I recognize that this research would not have been possible without the supporting personnel working in the physics department, and express my gratitude to those people.

Finally, I would like to express my sincere gratitude to my parents, for coping with me not lifting one finger in the house chores during my time at the keyboard. A simple "thank you" does not even begin to make up for their efforts and continuous support during my studies. But it is a start. Thank you.

Wout Keijers - juni 2017

Contents

Summary

Since their discovery in 1964 [1], superconducting quantum interference devices (SQUIDs) have been extensively used in applications, mostly as magnetic field sensors. SQUIDs are widely spread over various fields, from defect detection in engineering to the measurements of weak magnetic fields produced by the human brain. In more recent literature, D. Halbertal *et al.* [2] reported a thermal imaging technique based on a nano-SQUID mounted on a tip, with a sensitivity four orders of magnitude smaller than previous temperature sensing devices.

The scaling down of these devices led to low noise performance, which resulted in the flourishing of a new research area devoted to nano-SQUIDs. This thesis deals with modifying the weak links of a thin film aluminum micro-SQUID beyond the limit of current lithography techniques; electromigration, used as a fabrication technique, alters the properties of the weak links. Since these weak links dictate the SQUID's properties, its sensitivity and working range can be altered. The combination of electromigration and SQUIDs has yet to be reported in literature.

SQUIDs are the most sensitive magnetometers known today. The simple setup of a direct current SQUID (the other variant is the radio frequency SQUID, which is not discussed in this thesis) consist of two Josephson junctions in parallel connected by a superconducting loop. The main properties of the SQUID are determined by the size of the loop and the details of the Josephson junctions. The unique properties of the Josephson junctions are summarized by the Josephson relations, for which he was awarded the Nobel prize in Physics in 1973 [3]. In this work, the aforementioned junctions are classified as 'Dayem bridges', since they do not rely on tunneling contact as is the case in Josephson's derivation, but still exhibit the Josephson effect.

The controlled breakdown of the junctions is regulated by a unique piece of software, available at the KU Leuven, created by my daily supervisor, V. Zharinov. This software controls the voltage and current over/through the structure. Applying a current that is sufficiently large, the substantial current crowding in the junction induces a so-called 'electron wind force', responsible for knocking the thermally activated ions out of their lattice equilibrium position and move them elsewhere. The electron wind force originates from the frequent collisions between the conduction electrons and the lattice ions. As a result, it is capable of reducing constriction sizes to single atom contact. This software will be used to reduce the weak links cross section, connected in parallel in the SQUID structure.

The aim of this work is to design a superconducting quantum interference device on the micro-scale (1), reducing the weak link cross section via electromigration (2), and investigating the effect of this gradual decline of weak link cross section on the superconducting properties of the SQUID (3). A micro-SQUID is designed and fabricated using e-beam lithography (EBL) and molecular beam epitaxy (MBE) techniques. Since the design of the SQUID consists of two weak links in

parallel, the next step is to experimentally verify that this design is indeed compatible with parallel electromigration. This experimental verification is performed by in-situ electromigration, where a scanning electron microscope is employed to observe the dynamics of the electromigration process in-situ. Hereafter, the evolution of the superconducting properties of the SQUID using low temperature measurements are investigated as a result of modifying the weak links via electromigration.

The results of this thesis include (1) the successful design and fabrication of a thin film aluminum micro-SQUIDs using nanopatterning techniques, (2) the in-situ observation of parallel electromigration of the nanopatterned SQUID structure and (3) the experimental observation of the SQUID's properties modified after electromigration in a step-like fashion. Conclusions drawn from these results cover first of all the possibility to locally break down the two junctions arranged in parallel, using the SQUID structure designed in the framework of this thesis (goal 1 and 2 form the previous paragraph). Second, the properties of a SQUID can be modified via electromigration (goal 3 from the previous paragraph). Such modifications include the reduction of critical current, the introduction of asymmetry and the modification of the inductance parameter, an important parameter describing the SQUIDs performance. The asymmetry of the weak links measured in the low temperature measurements corresponds to the observed asymmetry in the in-situ EM measurement. Furthermore, the behavior of the SQUID's critical current can be understood from the numerical calculations of the asymmetric SQUID model while taking into account the kinetic inductance. Moreover, it is observed that when electromigration has sufficiently reduced the junction cross section, the SQUID can be operated in the dissipative state, where magnetic flux readout from voltage is possible. Hence, the goals discussed in the previous paragraphs are achieved.

Sparked by the pioneering work executed in this thesis, theoretical simulations and experiments on electromigrated niobium SQUIDs are currently being performed. These set of research data provides a very interesting and complete set of results, which will be submitted to a scientific journal in the coming months.

Summary in Layman's Terms

A superconducting quantum interference device (SQUID) is a sensor able to detect extremely weak electromagnetic signals. For example, it is capable of detecting magnetic fields 10 billion times smaller than the magnetic field moving the needle in a compass. As a result of this unmatched sensitivity, SQUIDs are used in a variety of research areas, such as brain signal detection in the medical sector, material defect detection in engineering and geological mapping of the earth's magnetic field. Even beyond magnetic field detection, it shows promising applications in nanoelectronics, such as a memory device or as qubits and logic gates in quantum computing. From a fundamental physics point of view, this is an extremely fascinating device. Its working principle relies on quantum mechanics, which extend to macroscopic length scales in the superconducting state.

In the superconducting state, the entire ensemble of mobile electrons, giving a metal its electrical conductivity, is described by a single wave function. Only below extremely cold temperatures, usually below -200 °C, is this superconducting state reached. This extraordinary state of matter exhibits truly fascinating phenomena, due to its wave-like nature. It comes to no surprise that the levitating trains attract the largest crowds in table-top physics demonstrations; the phenomenon of superconductivity remains prominent in captivating everyone's attention.

The operating principle of a SQUID is based on the unique features related to the aforementioned single wave function describing the superconducting state. When two superconductors are weakly connected, by a narrow constriction for example, a Josephson junction is formed, for which Josephson predicted its behavior and was awarded the Nobel prize in Physics in 1973. Connecting two of these junctions in a parallel arrangement, a SQUID is created. Much like waves on the surface of a pond, the wave function describing the ensemble of mobile electrons in one branch can interfere with the wave function in the other branch. The dependence of the interference on the magnetic flux going through the SQUID loop is responsible for the SQUIDs magnetic field sensitivity.

The scaling down of these devices to the micro- and even nano-regime, which has become an emerging research area attracting a lot of attention in the recent years, allows us to investigate small magnetic systems. However, the minimum size of the constriction width making up the weak links is limited by current nanoscale fabrication techniques. This work goes beyond the limit of current techniques using a method called controlled electromigration; applying high currents through a narrow constriction allows us to displace the atoms in a very controlled fashion, thus effectively reducing the weak link cross section.

The SQUID investigated in this work is 100 times smaller than the width of a human hair. It is designed in the framework of this thesis and fabricated using conventional nanoscale fabrication techniques. After fabrication, the weak links of the SQUID are gradually reduced in cross section via electromigration. The use of controlled electromigration to reduce the SQUID's weak link cross section has not yet been reported in literature. This thesis studies the effect of the SQUID's superconducting properties as the weak links are progressively electromigrated.

List of Abbreviations and Symbols

Abbreviations

AFM	Atomic Force Microscope
BCS	Bardeen Cooper Schrieffer
DC	Direct Current
EBL	Electron Beam Lithography
EM	Electromigration
ESD	Electrostatic Discharge
EWF	Electron Wind Force
GL	Ginzburg Landau
IMBL	Ion and Molecular Beam Lab
MBE	Molecular Beam Epitaxy
MRI	Magnetic Resonance Imaging
MTF	Mean Time to Failure
LHC	Large Hadron Collider
RF	Radio Frequency
SEM	Scanning Electron Microscope
SQUID	Superconducting Quantum Interference Device
TAPS	Thermally Assisted Phase Slips

Symbols

A	SQUID hole area
$\boldsymbol{A}$	Vector potential
α	SQUID critical current asymmetry parameter / GL parameter
α'	Temperature resistivity coefficient
$\boldsymbol{B}$	Magnetic flux density
β_L	SQUID inductance parameter
β_L	SQUID kinetic inductance parameter
β	GL parameter
C_v	Vacancy concentration
D_v	Vacancy diffusivity
D_i	Diffusivity related to path i
e	Elementary charge of the electron
E_a	Process activation energy barrier
η	SQUID inductance asymmetry parameter

$\boldsymbol{E}$	Electric field
f	Vacancy relaxation factor
F_s	Helmholtz free energy of the superconducting state
F_n	Helmholtz free energy of the normal state
ΔF	Helmholtz free energy barrier
h	Planck's constant
$\hbar$	Reduced Planck's constant
$\boldsymbol{H}$	Applied magnetic field
H_c	Thermodynamic critical field
$\boldsymbol{I}$	Current
I_0	Josephson junction critical current
$I_{1,2}$	Current through each branch of the SQUID
I_c	Critical current of the SQUID
$\boldsymbol{J_v}$	Vacancy flux
$\boldsymbol{j}$	Current density
$\boldsymbol{j}_s$	Supercurrent density
J	Circulating current in the SQUID loop
J^*	EM critical current density
k_B	Boltzmann constant
K	Coupling constant
L	Inductance or length of the constriction
L_K	Kinetic inductance
m	Mass of Cooper pair
m_0	Free electron mass
m^*	Effective electron mass
μ_0	Permeability of vacuum
n	Density of conduction electrons
n_c	Cooper pair density
n_d	Density of defects
n_s	Superelectron density
λ	Penetration depth
$\boldsymbol{p}$	Momentum
P	Power dissipated
φ	Phase difference over Josephson junction
ψ	Order parameters of the superconducting state
Φ	Magnetic flux
Φ_0	Magnetic flux quantum
Φ_{ext}	Flux due to the externally applied field
l	Length
q	Cooper pair charge
R	Resistance
R_0	Resistance at room temperature
R_m	Rate of mass transport
R_θ	Thermal resistance
ρ	Resistivity
ρ_0	Resistivity at room temperature
ρ_d	Resistivity of defects
S	Cross section
σ	Conductivity

t	Time or thickness thin film
T	Temperature
T_0	Room temperature
T_c	Superconducting critical temperature
τ	Characteristic time
θ	Phase of the superconducting order parameter
V	Electric potential
w	Width of the thin film line
ξ	Coherence length of the superconducting condensate
Z^*	Effective charge number
Ω	Atomic volume or attempt frequency

Chapter 1

Introduction

1.1 SQUIDs

Superconductivity was first measured by Heike Kamerlingh Onnes on April 8, 1911, in Leiden. He discovered that materials in this remarkable superconducting phase exhibit truly extraordinary properties. Examples of these include zero electrical resistivity and the expulsion of the magnetic field. A theoretical basis, describing this extraordinary phase, is presented by the Ginzburg Landau formalism. This theory states that these aforementioned properties arise from the macroscopic wave function, $\psi = |\psi|e^{i\theta}$, describing the superconducting state with a well defined phase. In 2003, the Nobel prize in physics was awarded to A. A. Abrikosov and V. L. Ginzburg together with A. J. Leggett for their work on the development of the theory of superconductivity and superfluidity. Many applications, ranging from Maglev trains, Magnetic Resonance Imaging (MRI) and the magnetic fields needed for the Large Hadron Collider (LHC) to microwave filters and fault current limiters are all relying on the intriguing properties of the superconducting phase. This extraordinary phase produces an even more remarkable device: The SQUID.

Superconducting Quantum Interference Devices, abbreviated as SQUIDs, are the most sensitive magnetometers known today. Two main types of SQUIDs exist: the direct current (DC) SQUID and the radio frequency (RF) SQUID. The DC type is more sensitive and will be investigated in this work. The DC SQUID was invented in 1964 by Robert Jaklevic, John J. Lambe, James Mercereau, and Arnold Silver of Ford Research Labs [1]. It consists of two Josephson junctions in parallel, weakly connecting two superconducting banks. The operating principle of the DC SQUID relies on the unique relation between the current flowing through the junction and the change of phase of the wave function across the junction. Besides this unique current-phase relation of the Josephson junction, a second superconducting phenomenon is responsible for the DC SQUID behavior. This second property follows naturally from the condition that the superconducting wave function must be single valued: the fluxoid quantization and its dependence on the magnetic flux passing through the SQUID loop. These two properties, unique to superconductors, are the pillars of the SQUID's working principle.

The first idea to scale down the Josephson junctions was thought of by Voss *et al.* in the 1980's [4]. His aim was to scale down the junction dimensions in order to achieve low noise performance. He created niobium DC-SQUIDs to reach an energy resolution close to the limit of the uncertainty principle. These nanoscale superconducting quantum interference devices, known as nano-SQUIDs,

are emerging as an active research field in the recent years. The idea is to be able to measure the magnetic moment associated with a nano-object. The holy grail in this field is the measurement of single atomic spins. Other sensor applications are based on any physical quantity that can be converted in a magnetic flux threading the SQUID loop. Such examples include a single photon detector, macromolecule detection and scanning SQUID microscopy. Since its working principle relies on quantum mechanics, it qualifies as a sensor in the upcoming field of quantum metrology. In computing and even quantum computing applications, the SQUID is employed as a memory device and logic gate. More recently, the group of D. Halbertal *et al.* reported a nano-thermometer based on a nano-SQUID residing on the apex of a sharp pipette. This non-contact thermal imaging technique provides a thermal sensing that is four order of magnitude more sensitive than previous devices - below 1 μKHz$^{-1/2}$ [2]. An overview on the (potential) use of nano-SQUIDs in applications are presented in [5].

1.2 Outline of this Work

The device studied in this work has nanoscale, 'bow-tie' shaped, weak links connecting the two superconducting banks. The washer hole size is roughly 600×700 nm^2. Since this area is rather close to 1 μm^2, the device is classified as a micro-SQUID. This micro-SQUID is fabricated using conventional e-beam lithography and molecular beam epitaxy techniques. The result after fabrication is a nano-patterned aluminum thin film on a SiO_2 substrate, presented in Figure 1.1.

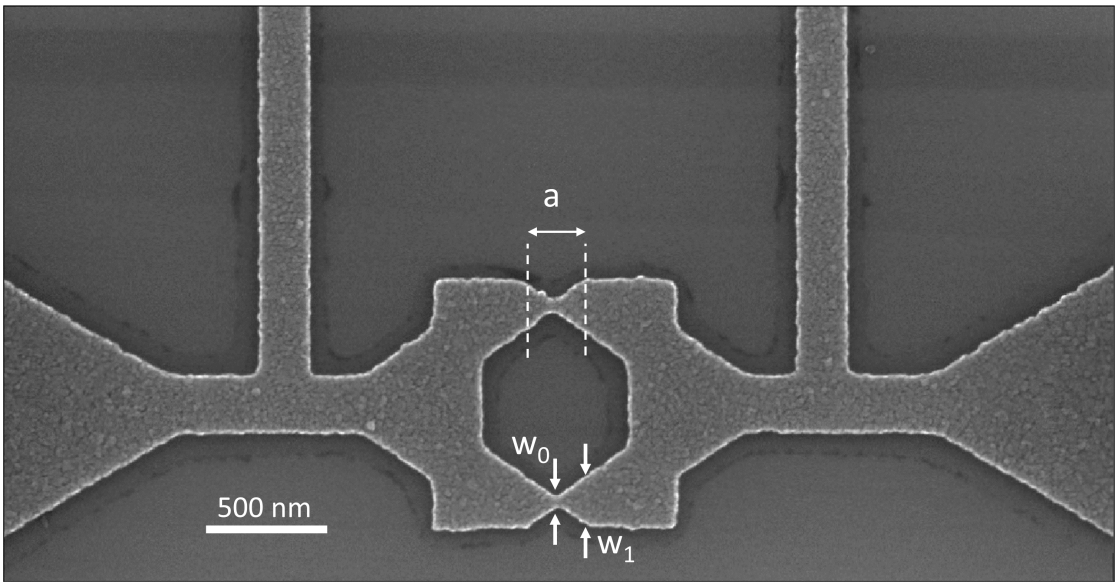

Fig. 1.1: *Nano-patterned thin film aluminum on SiO_2 substrate. The 'bow-tie' shaped constriction was designed with dimensions of $a = 250$ nm, $w_1 = 200$ nm and $w_0 = 33$ nm. The probing voltage leads, indicated as $V+$ and $V-$, and the current leads, indicated as $I+$ and $I-$, all have widths of 200 nm. Image taken with a scanning electron microscope.*

This thesis marks the first investigation of the superconducting properties of a SQUID where the weak link cross sections are reduced using electromigration. Electromigration is a gradual displacement

of the metallic ions in the lattice due to high current densities. Usually, electromigration is a menace in high power devices and for the scaling down of nanoelectronics in general. However, in this work, electromigration is used as a technique to control junction cross section to dimensions not reached by conventional e-beam lithography techniques. A controlled electromigration software, created by my daily supervisor, V. Zharinov, is able to reduce constriction dimensions towards the quantum point contact. The reduction of the weak link cross section allows us to study the properties of a SQUID towards two superconducting banks only connected by two quantum point contacts. Since these weak links determine the properties of the SQUID, such as its sensitivity and its working range, modifying these links using a novel fabrication technique could produce interesting results.

The nano-patterned aluminum thin film was designed in the framework of this thesis. This design is shown to be compatible with electromigration while still exhibiting the SQUID characteristics.

The results of this thesis can be summarized as follows: (1) the successful design and fabricated of aluminum thin film micro-SQUIDs (2) parallel electromigration of the micro-SQUID's weak links observed in-situ in the imaging chamber of a SEM (3) the characterization of the SQUID device performance while gradually reducing the weak link cross section by means of electromigration.

The outline of this work is as follows:

Chapter 2 introduces the theoretical background. The first part deals with the physics of electromigration. The second part is devoted to a general introduction to superconductivity based on the Ginzburg Landau formalism. More details are given on the phenomena related to the working principle of the SQUID. The physics of the SQUID itself and its asymmetric variant are also discussed here.

Chapter 3 presents the experimental methods and devices used in this work. Sample fabrication, characterization, controlled electromigration and superconductivity measurements are discussed.

Chapter 4 deals first with the needed steps towards the fabrication of the micro-SQUID. Second, the electromigration software is demonstrated on gold structures. Third, bow-tie shaped aluminum junctions are observed to reduce their cross section via electromigration. Lastly, in-situ electromigration in the imaging chamber of the SEM located in Liège presents the weak links' reduction in cross section in the micro-SQUID.

Chapter 5 treats the superconductivity measurements. This chapter is kicked off by determining the superconducting parameters of thin film aluminum structures. Next, the superconducting properties of the SQUID are characterized. First, the virgin SQUID is characterized, later, the effect of gradually reducing the weak link cross section via electromigration on the SQUID's superconducting properties is investigated.

Chapter 6 finalizes this work by presenting the conclusions of this thesis. Furthermore, this chapter provides an outlook for further experimental investigations, both here at the KU Leuven and at L'Université de Liège. Moreover, theoretical simulations will be performed at the University of Antwerp.

Chapter 2

Theoretical Introduction

The first part of this chapter, Section 2.1, discusses the physics of electromigration. The second part, Section 2.2, presents a theoretical introduction to superconductivity.

2.1 Electromigration

This section discusses the main physical phenomena related to electromigration. First, some general concepts related to metals are provided in Section 2.1.1. Next, electromigration in the context of atomic diffusion is discussed in Section 2.1.2. Then, Section 2.1.3 discusses the electromigration driving force, the so-called 'wind force'. Finally, the mean time to failure described by Black's model and parallel electromigration is discussed, given in Sections 2.1.4 and 2.1.5, respectively. This theoretical introduction is based on the review papers of A. Scorzoni [6], D. G. Pierce [7], R. L. de Orio [8] and R. L. de Orio's PhD dissertation [9].

2.1.1 General Electrical Properties of Metals

When atoms come together to form a metal, the electrons from the outer atomic shell become delocalized. These electrons are free to roam the space between the ions. They are responsible for the high electrical conductivity of metals. The ions are arranged in a well defined lattice exhibiting long range order.

Drude Model

Three years after Thomson discovered the electron in 1897, Paul Drude formulated a 'kinetic gas theory' for charged particles [10]. He assumed that due to the positive background of ions, the coulomb repulsion between electrons is screened. Drude described the electrons as free particles that lose momentum through collisions with the atoms and gain momentum from the electric field, leading to the Drude equation:

$$\frac{d\boldsymbol{p}}{dt} = (-e)\boldsymbol{E} - \frac{\boldsymbol{p}}{\tau}. \tag{2.1}$$

Here, $\boldsymbol{p}$ is the momentum of the electron, $(-e)$ its charge, $\boldsymbol{E}$ the electric field and τ the characteristic time between collisions. In the stationary state ($d\boldsymbol{p}/dt = 0$), the momentum is $\boldsymbol{p} = -e\boldsymbol{E}\tau$. From the

stationary state solution, the current density can be found:

$$\boldsymbol{j} = (-e)n\frac{\boldsymbol{p}}{m^*} = \frac{ne^2\tau}{m^*}\boldsymbol{E}, \tag{2.2}$$

with n the density of electrons and m^* the electron mass. Labeling the proportionality constant as the (Drude-) conductivity, the well known Ohm's law [1] $\boldsymbol{j} = \sigma\boldsymbol{E}$ is found, or equivalently,

$$V = IR. \tag{2.3}$$

Where V is the electric potential (from $\boldsymbol{E} = -\boldsymbol{\nabla}V$), I the current and R the resistance ($R = \rho l/S$, with ρ the resistivity, S the cross section and l the length of the conductor, and $\rho = 1/\sigma$ with σ the conductivity). Drude's microscopic model is thus capable of producing Ohm's empirical law.

From equations (2.2) and (2.3), it can be seen that the time between scattering events τ relates inversely proportional to the resistance R. This can intuitively be understood; the more frequent the collisions are, the more 'drag' an electron experiences. This scattering occurs whenever an atom is out of place for any reason. Sources of scattering include defects such as impurities, grain boundaries and surfaces. Also thermal vibrations cause the electrons to scatter. These thermal vibrations displace the atom out of its equilibrium position, oscillating at the Debye frequency. The higher the temperature, the higher the vibration amplitude, leading to a decreased scattering time and increased resistance.

Temperature Dependence

In this simple Drude model, the relaxation time is a constant. Therefore, there is no temperature dependence on the drude-conductivity. In general, τ depends on the concentration of phonons. This dependence influences the temperature dependence of the electrical conductivity. An empirical relation to describe the temperature dependence of the metallic resistivity in the vicinity of room temperature is

$$\rho = \rho_0 \left(1 + \alpha' \left(T - T_0\right)\right), \tag{2.4}$$

with ρ_0 its resistivity at temperature T_0 and α' the resistivity temperature coefficient. The increase of resistivity at these temperatures can be explained by an increase of electron-phonon scattering events. More rigorous models describing the temperature dependence include the semi-classical Boltzmann transport equation.

Joule Heating

The electron phonon interaction discussed above is a inelastic scattering event; the electron loses energy to the phonon bath. An increase in phonons or vibrations imply a higher temperature. Joule heating is the process by which heat is generated due to the passage of current through a conductor. Since the electrical resistivity depends on temperature, pushing a current through a metallic conductor induces Joule heating and thus changes its resistance. Equation (2.4) can be rewritten as $R = R_0(1 + \alpha'\Delta T)$ with R_0 the resistance at reference temperature T_0 ($\Delta T = T - T_0$). Using a solution of the Fourier law, $\Delta T = R_\theta P$, with R_θ the thermal resistance and $P = RI^2$ the dissipated electrical power, the previous equation can be rewritten as

[1] *often quoted as a law, whereas it is a definition, not a law. This linear relation is only a first order approximation.*

$$R = R_0(1 + \alpha' R_\theta P) \tag{2.5}$$
$$= R_0(1 + \alpha' R_\theta R I^2) \tag{2.6}$$
$$\Leftrightarrow R(I) = \frac{R_0}{1 - \alpha' R_\theta I^2 R_0}. \tag{2.7}$$

This simple model (equation 2.7) presents the resistance value for a self-heated metallic conductor by a current.

2.1.2 Atomic Diffusion

To introduce the concept of electromigration, some context is given first. Electromigration is essentially a biased atomic diffusion phenomenon, where the bias originates from the applied electric field. This section briefly discusses electromigration in the context of other driving forces related to atomic diffusion. While the atomic transport equations can be expressed in terms of either vacancies or atoms, vacancy tracking is elected in the following model [8]:

$$\boldsymbol{J}_v = -D_v \left(\boldsymbol{\nabla} C_v - \frac{|Z^*|e}{k_B T} C_v \rho \boldsymbol{j} - \frac{Q^*}{k_B T^2} C_v \boldsymbol{\nabla} T + \frac{f\Omega}{k_B T} C_v \boldsymbol{\nabla} \sigma \right), \tag{2.8}$$

where J_v is the vacancy flux, D_v is the vacancy diffusivity, C_v the vacancy concentration, Z^* the effective charge number, ρ the resistivity, $\boldsymbol{j}$ the current density, Q^* is the heat flow, f is the vacancy relaxation factor, Ω the atomic volume, σ the hydrostatic pressure and k_B the Boltzmann constant, e the elementary charge and T the temperature. The terms are, from left to right, diffusion induced by the gradient of the vacancies, next the electromigration term itself, and lastly the driving forces due to gradients of temperature and mechanical stress gradients. The diffusivity factor, D_v, itself depends on temperature:

$$D_v = D_0 exp\left(-\frac{E_a}{k_B T} \right), \tag{2.9}$$

with E_a the ionic binding energy, presenting typical Arrhenius behavior.

As can be seen from formula (2.8), multiple counteracting physical processes are active.The net flow of vacancies (or ions) is a result of the interplay between these terms. However, for high current densities and long wires, where the Blech effect can be neglected (which induces ion backflow due to stress), the electromigration term dominates.

Diffusivity Paths

There are several paths through which the ion can diffuse in the lattice, each corresponding to its own diffusivity constant D_i. Paths where the diffusivity is high are typically at the surface and along grain boundaries. At these locations, the binding energy of the ion is less compared to the ion in bulk, allowing them to be excited by thermal fluctuations more easily and subsequently carried away due to the wind force, which will be explained in the next section. The link between binding energy and diffusivity can be seen in equation (2.9). Figure 2.1 illustrates two different grain boundary orderings in thin film metallic wires. Since the bulk ion mobility is less than the ion mobility along a grain boundary, the wire depicted on the right is expected to be more robust to electromigration.

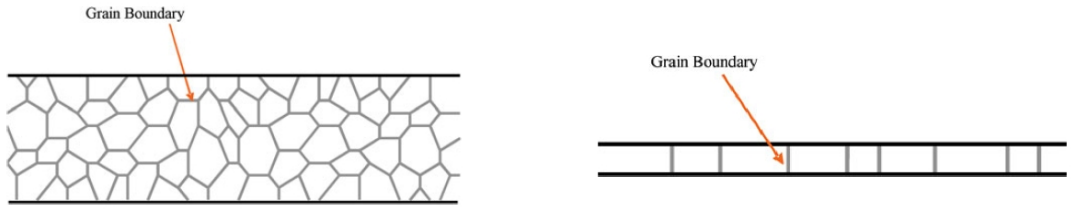

Fig. 2.1: *Grain ordering in polycrystalline metallic wires. The structure on the right presents a 'bamboo'-like ordering of the grain boundaries. Figures taken from [11].*

2.1.3 Electron Wind Force

Each lattice atom resides in a local potential minimum. This bound lattice atom can overcome this activation energy barrier E_a by thermal energy, resulting in an Arrhenius like distributed number of activated atoms (equation (2.9)). Typically, atomic diffusion is a random process, there is no preferred direction of the atom to 'jump'. However, when a large current density is present, the electron current biases the atomic jump in the direction of the electron flow. The force associated with this momentum transfer is called the 'electron wind force' or $\boldsymbol{F}_{EWF}$. The net flow of ionic mass in the direction of the electron flow is called electromigration.

Similar to the Drude model presented earlier, scattering time, and thus the collision frequency, is related to the number of phonons and defects present in the material. The theoretical basis for this wind force was derived by Huntington and Grone [12]:

$$\boldsymbol{F}_{EWF} = -\frac{n\rho_d m_0}{n_d m^*} e\boldsymbol{j}, \tag{2.10}$$

with n the density of conduction electrons, ρ_d the resistivity of defects, m_0 the free electron mass, m^* the effective electron mass, n_d the density of defects, $\boldsymbol{j}$ the current density, and e the charge of the electron. They were the first to introduce the electron wind force, an expression for the friction force on the atoms in bulk conductors exerted by the electron flow.

2.1.4 Black's Model

Aluminum high power devices and integrated circuits carrying high current densities (at least 10^5 A/cm^2) are prone to a common failure mode: Open circuits as a consequence of electromigration. A crack is usually observed in the aluminum conductor, resulting in failure of the device. Electromigration as a failure mechanism has been studied since the 60's. James Black was the first to introduce an expression for the mean time to failure of a metal line subjected to electromigration. He considered that the mean time to failure, MTF, is inversely proportional to the rate of mass transport, R_m:

$$MTF \propto \frac{1}{R_m}. \tag{2.11}$$

The rate of mass transport which takes place in the migration of aluminum by momentum transfer between thermally activated ions and the electrons should, according to Black, be a function of the momentum of the electron, the frequency of electrons striking the activated ions and the number of activated ions or 'targets' available per volume. The rate of mass transport can be expressed as:

$$R \propto \text{(electron momentum)} \\ \text{(frequency of striking electrons)} \\ \text{(number of thermally activated atoms)}$$

Note the similarity with the electromigration term in equation (2.8), where $\boldsymbol{j}$ contains the electron momentum, ρ and $\boldsymbol{j}$ their striking frequency and D_v the number of thermally activated atoms (equation 2.9). Black only considers this term of the total diffusion equation, neglecting the other terms. Nevertheless, Assuming the electron momentum and their striking frequency is proportional to the current density and furthermore assuming that the number of thermally activated atoms follow an Arrhenius law, Black's model is obtained [13], [14]:

$$MTF = \frac{A}{j^2} exp\left(\frac{E_a}{k_B T}\right), \tag{2.12}$$

where A contains information such as the material properties and the geometry of the wire, E_a the activation energy, k_B the Boltzmann constant and T the temperature.

To understand this failure mechanism, the concept of divergence is a key factor. Without divergence, a uniform transport would exists and no mass net mass would be removed at a certain location. Thermal gradients or spatial variations of grain sizes create a non-zero divergence value; the flux of total ions entering a certain volume is not equal to the number of ions exiting this volume. This indicates the presence of region where mass is removed (void formation) and other regions where mass is deposited. The removal of mass is responsible for the crack/void formation discussed in the papers of J. Black leading to failure of the aluminum interconnects [13], [14].

2.1.5 Parallel Electromigration

A relevant paper in the framework of this thesis is the paper by Johnston et al. [15]. This paper performs electromigration on 16 junctions in parallel. A criterion is also introduced here, determining the success of parallel electromigration and thus avoiding an uncontrolled junction breakdown. This criterion is:

$$\frac{\partial P_1}{\partial R_{j1}} < \frac{\partial P_2}{\partial R_{j1}}, \tag{2.13}$$

where R_{j1} is the resistance of the first junction, R_{j2} the resistance of the second junction which lies in parallel with the first and P_1 and P_2 the power dissipated in the first and second junction, respectively. The criterion states that as R_{j1} increases due to electromigration, the power P_2 dissipated in the second junction must increase at a greater rate than P_1. When this criterion is fulfilled, the electromigration naturally balances between the junctions and they evolve together. Only when the resistance connecting both junctions is smaller than the resistances of the junction itself, is this criterion met.

2.2 Superconductivity

Microscopic thin film aluminum direct current superconducting quantum interference devices (DC micro-SQUIDs) are investigated. In order to understand the working principle of this device, an

introduction to superconductivity will be presented in this section. Extra attention will be paid to the superconducting phenomena crucial for the operation of a SQUID. The discussion is opened with a brief historical overview of the broad field of superconductivity (Section 2.2.1). Next, a section on the theory of superconductivity discusses the Ginzburg-Landau formalism (Section 2.2.2), followed by a section devoted to superconductors with reduced dimensions (Section 2.2.3). The next two sections discuss the essential phenomena related to the working principle of a SQUID (Sections 2.2.4 and 2.2.5). At this point the equations governing the SQUID's behavior are introduced (Section 2.2.6). In addition, the more general case of a SQUID with asymmetric junctions is discussed (Section 2.2.7). The section on superconductivity is finalized by the introduction of phase slips. This discussion (Section 2.2) is based on the works of V.V. Schmidt [16] , M. Tinkham [17], C. P. Poole *et al.* [18] and R. Kleiner *et al.* [19].

2.2.1 History

> *"Mercury has passed into a new state, which on account of its extraordinary electrical properties may be called the superconductive state."*
> - Heike Kamerlingh Onnes

Superconductivity was first discovered in 1911 in Leiden by Kamerlingh Onnes and co-workers [20]. After Kamerlingh had developed a method to liquefy helium, he was able to test various theories on the behavior of metallic electrical resistivity at low temperatures. He quickly discovered that below a 'critical' temperature T_c, the resistivity of some metals suddenly vanishes. He first observed this remarkable 'superconducting' state in mercury. The original plot of this measurement is presented in Figure 2.2. This figure illustrates that Kamerlingh was a true experimentalist; below the critical temperature he indicates a resistance of $10^{-5}\ \Omega$, not zero. In this 'superconducting' state, the resistivity is so small that persistent currents in a superconducting ring flow without any dissipation or weakening for more than a year, when the experiment was finally halted.

Besides the remarkable electrical properties of the superconducting state appearing below T_c, the Meissner effect is the second defining characteristic of superconductivity. This effect was discovered by W. Meissner and R. Ochsenfeld in 1933 [21]. They discovered that in the superconducting state, all magnetic flux is expelled from a bulk superconductor, making them perfect diamagnets. This diamagnetism results from screening currents at the surface, creating an opposing magnetic field. However, the field expulsion of this superconducting state does not behave as a perfect conductor. Cooling a superconductor in magnetic field will expel the field and not trap it as is the case for an ideal conductor. This field cooling of the superconducting state shows its unique diamagnetic behavior. Since the superconducting state is solely described by the thermodynamic quantities T and H, a thermodynamic theory can be formulated.

The first phenomenological model that succeeded in describing the persistent current and flux repulsion was derived in 1935 by the London brothers [22]. They assumed that a certain number, n_s, of charge carriers behave like a superfluid and flows without friction. In 1950, V. Ginzburg and L. Landau provided an important extension to the London theory [23], in which a spatially constant density of the superconducting charge carriers was no longer assumed. In this theory, the superconducting state is described by a macroscopic wave function. For a long time, a microscopic theory was lacking, until Bardeen, Cooper and Schrieffer created their 'BCS' theory in 1957 [24]. It was later (1959) also shown by Gor'kov that for temperatures near T_c the GL theory can be derived from the

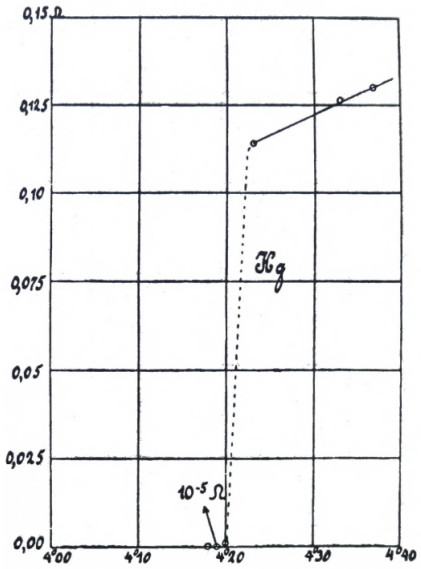

Fig. 2.2: *Original plot of resistance (Ω) versus temperature (K) for mercury [20].*

BCS theory [25]. In 1972, Bardeen, Cooper and Schrieffer were awarded the Nobel Prize in physics for their BCS theory. They recognized that at the transition to the superconducting state, the phonon mediated electrons condense pairwise into so-called Cooper pairs. These pairs form a coherent matter wave with a well-defined phase. During the turn of 1986/87 the gold rush for high temperature superconductors set in. These efforts soon led to the discovery of multiple superconductors with a critical temperature above the boiling point of liquid nitrogen. To this day, the quest for room-temperature superconductivity continues.

More specific historical events related to the devices used in this work include the experimental discovery of the magnetic flux quantum and the theoretical prediction of the Josephson current. In 1961, two independent groups experimentally verified the existence of the flux quantum. The two groups, namely Doll and Näbauer in Munich [26] and Deaver and Fairbank in Stanford [27] published their results of flux quantization in superconducting hollow cylinders, which indicated that the flux through the cylinder appears as integer multiples of a flux quantum. One year later, in 1962, Brian D. Josephson predicted for the first time a weak supercurrent caused by the tunneling of Cooper pairs between two superconductors separated by a barrier [3]. This Josephson current exhibits various interesting properties which are extensively applied in nanoscale devices for quantum metrology. Josephson received in 1973 the Nobel Prize for his discovery. Both phenomena described above are crucial for the correct operation of a SQUID.

2.2.2 Ginzburg Landau Theory

The Ginzburg-Landau (GL) theory [25, 23] was the first quantum (phenomenological) theory of superconductivity. The GL theory starts from the argument that the transition to the superconducting state in absence of a magnetic field is described by a second order phase transition. A second prerequisite states that the superconducting state is more ordered than the normal state. This implies the existence of a superconducting (complex) order parameter $\psi = |\psi|e^{i\theta}$, which is zero for $T > T_c$

and non-zero for $T < T_c$. A second order phase transition also implies that the order parameter changes gradually below T_c, while it is discontinuous at the transition temperature T_c.

This order parameter, ψ, can be interpreted as an effective wave function (pseudo wave function). This is the central hypothesis behind the GL theory; there exists a macroscopic wave function of the form $\psi(\boldsymbol{r},t) = |\psi(\boldsymbol{r},t)|e^{i\theta(\boldsymbol{r},t)}$ that describes the entire ensemble of the superconducting electrons. Validation for this interpretation became clear when Gor'kov derived the GL theory from the BCS theory [24]. In 1957, when the BCS theory was developed, for the first time the superconducting state had a theory at the microscopic level. This BCS theory claims that electrons with opposite momenta and spin can form a bound state mediated by electron-phonon coupling, the Cooper pair. Due to the opposite spin of the superconducting electrons, the total spin is zero and the Cooper pair is of bosonic nature. Since the Pauli exclusion principle does not apply to bosons, these Cooper pairs can occupy the same quantum state, giving the superconducting state its remarkable properties. The complex order parameter, ψ, derived in the GL theory describes the superconducting electrons. The local density of these superconducting electrons[2], n_s, is given by

$$n_s/2 = |\psi(\boldsymbol{r})|^2. \tag{2.14}$$

The GL theory is based on an expansion of the free energy in powers of the order parameter and its gradient. This implies that the GL theory is only valid for small values of the order parameter, thus at a temperature sufficiently close to the critical temperature, T_c. The GL expansion of the superconductor's Helmholtz free energy is [17]:

$$F_s = F_n + \alpha|\psi^2| + \frac{\beta}{2}|\psi|^4 + \frac{1}{m}\left|\left(\frac{\hbar}{i}\boldsymbol{\nabla} - q\boldsymbol{A}\right)\psi\right|^2 + \mu_0\frac{\boldsymbol{H}^2}{2}, \tag{2.15}$$

with F_n the free energy in the normal state, α and β the two expansion coefficients of the GL theory, $m = 2m^*$ with m^* the effective mass of the superconducting electron, $q = 2e$ with e the elementary charge, $\hbar$ the reduced Planck's constant ($\hbar = h/2\pi$), $\boldsymbol{A}$ the vector potential and $\boldsymbol{h}$ the magnetic field associated with this potential, related through $\boldsymbol{B} = \boldsymbol{\nabla} \times \boldsymbol{A}$. A closer look is taken at each term individually.

- The expansion terms $\alpha|\psi|^2 + \frac{1}{2}\beta|\psi|^4$ represent the typical Landau form for the expansion of a second order phase transition.
- The term $\frac{1}{m}\left|\left(\frac{\hbar}{i}\boldsymbol{\nabla} - q\boldsymbol{A}\right)\psi\right|^2$ represents an increase in energy due to spatial variations of the superconducting order parameter. The form of this term is equivalent to the kinetic energy in quantum mechanics. It describes the kinetic energy of a free particle of twice the electron mass and twice its charge moving in a vector potential field.
- The final term, $\frac{1}{2}\mu_0\boldsymbol{H}^2$, represents the energy needed to repel the magnetic field out of the interior of the superconductor.

A simple analysis of the free energy given by equation 2.15 in absence of fields and gradients produces

$$F_{s0} - F_n = \alpha|\psi|^2 + \frac{1}{2}\beta|\psi|^4, \tag{2.16}$$

[2] *A 'superconducting' electron is an electron bound in a Cooper pair. Thus for each Cooper pair there exists two superconducting electrons. The local Cooper pair density, n_c, is $|\psi(\boldsymbol{r})|^2$.*

which can be interpreted as a series expansion in n_s or $|\psi|^2$, where higher order terms are neglected. Considering the previous discussion on the order parameter, the superconducting phase is obtained when the minimum of the free energy occurs at a non-zero value of the order parameter. This implies that the theory only has physical meaning if the β coefficient has a positive value. However, for the α coefficient, there are two scenarios: If α is positive, the minimum free energy is obtained for $|\psi|^2 = 0$, corresponding to the normal state. If α is negative, the minimum occurs when

$$|\psi|^2 = |\psi_\infty|^2 \equiv -\frac{\alpha}{\beta}, \tag{2.17}$$

in which ψ_∞ is the conventional notation for the strength of the order parameter infinitely deep in the interior of the superconductor. These two scenarios for α positive and negative are illustrated in Figure 2.3.

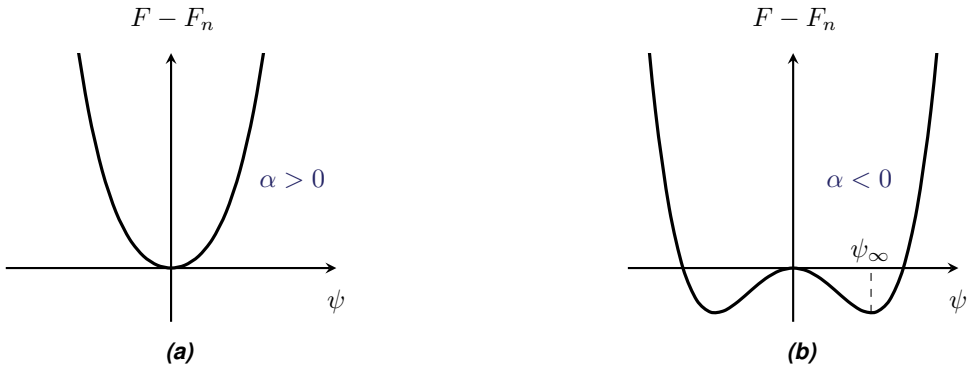

Fig. 2.3: *Ginzburg Landau free energy difference $F - F_n$ as a function of ψ for* ***(a)*** *$\alpha > 0$ ($T > T_c$) and* ***(b)*** *$\alpha < 0$ ($T < T_c$). ψ is taken real for simplicity.*

Furthermore, the coefficient α can be expanded in a Taylor series of the temperature. β can be considered to be independent of temperature. A first order expansion of α in temperature allows us to write $\alpha(T)$ as:

$$\alpha(T) = \alpha(0)\left(\frac{T}{T_c} - 1\right). \tag{2.18}$$

These rather abstract coefficients α and β can now be connected with the definition of the so-called thermodynamic critical field H_c, defined using the difference between the normal state free energy and the superconducting state free energy in zero magnetic field ($F_n - F_{s0} = \mu_0 H_c^2/2$). Filling in the value for the order parameter at the minimum given in (2.17) back into equation (2.16) and relating this to the critical field gives

$$\mu_0 H_c^2 = \frac{\alpha^2}{\beta}. \tag{2.19}$$

Furthermore, placing the first order expansion of α (equation (2.18)) into equation (2.17), it is found that $|\psi|^2 \propto (1 - T/T_c)$, for temperatures in the vicinity of, but below, T_c.

Ginzburg Landau Equations

Using the variational principle and starting from the assumed series expansion of the free energy in terms of ψ and $\nabla\psi$ (equation (2.15)), the two fundamental GL equations are derived:

$$\frac{1}{m}\left(\frac{\hbar}{i}\boldsymbol{\nabla} - q\boldsymbol{A}\right)^2 \psi + \beta|\psi|^2\psi = -\alpha(T)\psi, \tag{2.20}$$

$$\boldsymbol{j}_s = \frac{q\hbar}{2im}\left(\psi^*\boldsymbol{\nabla}\psi - \psi\boldsymbol{\nabla}\psi^*\right) - \frac{q^2}{m}|\psi|^2\boldsymbol{A}, \tag{2.21}$$

with $\boldsymbol{j}_s$ the supercurrent density. This system of coupled differential equations must be supplemented with proper boundary conditions. A trivial and frequently used boundary condition is that the supercurrent (equation (2.21)) can not flow out of the superconductor into the vacuum, i.e. that value of the supercurrent component perpendicular to the superconductor surface is zero:

$$\left(i\hbar\boldsymbol{\nabla} + q\boldsymbol{A}\right)|_{\boldsymbol{n}}\,\psi = 0, \tag{2.22}$$

where $\boldsymbol{n}$ is the unit vector normal to the surface of the superconductor. Equation (2.21) can be rewritten using the phase and modulus notation of the complex order parameter, $\psi = |\psi|e^{i\theta}$. This produces

$$\boldsymbol{j}_s = \frac{q}{m}|\psi|^2\left(\hbar\boldsymbol{\nabla}\theta - q\boldsymbol{A}\right) = q|\psi|^2\boldsymbol{v}_s, \tag{2.23}$$

in which the superfluid velocity operator $\boldsymbol{v}_s = 1/m\,(\boldsymbol{p} - q\boldsymbol{A})$ is used, with $\boldsymbol{p}$ the momentum operator $\boldsymbol{p} = -i\hbar\boldsymbol{\nabla} = \hbar\boldsymbol{\nabla}\theta$. A more transparent form of the supercurrent is found in equation (2.23), where the supercurrent density is expressed as the charge of the Cooper pairs, times their local density and velocity. The GL theory also introduces two characteristic lengths related to the spatial variations of the magnetic field an the order parameter $|\psi|$. These lengths scales are the penetration depth λ and the Ginzburg-Landau coherence length ξ, respectively. Using simplified examples, the physical significance of these parameters will be discussed in more detail.

Coherence Length ξ

The Ginzburg Landau coherence length is defined as

$$\xi(T) = \sqrt{\frac{\hbar^2}{2m|\alpha(T)|}}. \tag{2.24}$$

It describes the length scale over which variations in the magnitude of the order parameter can occur. This can be understood by considering the following: By introducing $f = \psi/\psi_\infty$ with ψ_∞ defined in equation (2.17), the first GL equation (2.20), in absence of magnetic fields, can be written as

$$\xi^2(T)\frac{d^2f}{dx^2} + f + f^3 = 0. \tag{2.25}$$

Furthermore, taking $g = f - 1$ and expanding equation (2.25) in terms of g the following equation is obtained:

$$\xi^2(T)\frac{d^2g}{dx^2} = 2g. \tag{2.26}$$

Solutions of this second order differential equation can be written as

$$g(x) \propto exp(-\sqrt{2}x/\xi(T)^2), \tag{2.27}$$

revealing that variations of ψ from ψ_∞ will decay over a length scale of the order of $\xi(T)$.

Since $\alpha(T)$ depends on temperature, this characteristic length scale varies as function of temperature. In the vicinity of T_c, equation (2.18) indicates $\alpha \propto (T_c - T)$. Therefore, the coherence length depends on temperature as $\xi \propto (T_c - T)^{-1/2}$. It can be seen that the coherence length diverges close to T_c.

Penetration Depth λ

Another important characteristic length scale in a superconductor besides the coherence length is the penetration depth λ:

$$\lambda(T) = \sqrt{\frac{m}{|\psi|^2 q^2 \mu_0}}. \tag{2.28}$$

The physical meaning of this length scale can be understood by the following derivation. Taking the curl on both sides of the first equality in equation in (2.23), taking into account that the curl of divergence is zero and using $\boldsymbol{\nabla} \times \boldsymbol{A} = \boldsymbol{B}$,

$$\boldsymbol{\nabla} \times \boldsymbol{j}_s = -\frac{q^2}{m}|\psi|^2 \boldsymbol{B}. \tag{2.29}$$

Next, using the Maxwell relation $\boldsymbol{\nabla} \times \boldsymbol{B} = \mu_0 \boldsymbol{j}$ and again taking the curl on both sides of (2.29):

$$\boldsymbol{\nabla} \times (\boldsymbol{\nabla} \times \boldsymbol{j}_s) = -\frac{\mu_0 q^2 |\psi|^2}{m} \boldsymbol{j}_s. \tag{2.30}$$

Next, recalling the vector calculus identity, $\boldsymbol{\nabla} \times (\boldsymbol{\nabla} \times \boldsymbol{j}_s) = \boldsymbol{\nabla}(\boldsymbol{\nabla} \cdot \boldsymbol{j}_s) - \boldsymbol{\nabla}^2 \boldsymbol{j}_s$, using the continuity equation ($\boldsymbol{\nabla} \cdot \boldsymbol{j}_s = 0$) and the definition of the penetration depth (2.28):

$$(\boldsymbol{\nabla}^2 - \lambda^{-2}) \boldsymbol{j}_s = 0. \tag{2.31}$$

Again taking the curl of the previous equation and using equation (2.29), the equation for the magnetic field is found:

$$(\boldsymbol{\nabla}^2 - \lambda^{-2}) \boldsymbol{B} = 0. \tag{2.32}$$

Since the magnetic field deep inside the superconductor must be zero, one boundary condition is readily obtained. The second boundary condition states that the field (sufficiently far) outside of the sample is the applied field. Considering a semi-infinite space occupied by a superconductor ($x > 0$) and where the other half is vacuum ($x < 0$), the boundary conditions and the fact that magnetic field lines must close ($\boldsymbol{\nabla} \cdot \boldsymbol{B} = 0$) imply that the field lines are tangent to the interface surface. Without loss of generality, the magnetic field can be written as $\boldsymbol{B} = B(x)\hat{\boldsymbol{z}}$. Solutions of the two above equations describing the supercurrent (2.31) and the magnetic field (2.32) are exponential functions decaying over a length scale of λ:

$$\boldsymbol{j}_s(x) \propto exp(-x/\lambda) \tag{2.33}$$

$$\boldsymbol{B}(x) \propto exp(-x/\lambda) \tag{2.34}$$

Since the definition of the penetration depth (equation (2.28)) contains only constants and the order parameter, ψ, its temperature dependence originates from the order parameter. From equations (2.17) and (2.18) it follows that the penetration depth varies with temperature as $\lambda(T) \propto (T_c - T)^{-1/2}$. Similar to the coherence length, the penetration depth diverges close to T_c.

Ginzburg Landau Parameter κ and Type I/II Superconductors

The penetration depth and coherence length not only provide the important length scales of the superconducting condensate, their ratio subdivides the class of superconducting materials into two types. Depending on this ratio, defined as the Ginzburg Landau parameter $\kappa = \frac{\lambda(T)}{\xi(T)}$, the superconductor is classified as Type I or Type I when

$$\kappa < \frac{1}{\sqrt{2}} \rightarrow \text{Type I superconductor},$$
$$\kappa > \frac{1}{\sqrt{2}} \rightarrow \text{Type II superconductor}.$$

For type I superconductors below a critical externally applied field H_c, the superconductor is said to be in the Meissner state where all flux is expelled from the interior. At applied fields higher than the critical field, the magnetic flux penetrates the superconductor and superconductivity is destroyed. In type II superconductors, the Meissner state only appears below of first critical field H_{c1}. Besides its first critical field, two more more critical fields exist for type II superconductors. between the first and second critical field, $H_{c1} < H < H_{c2}$, the sample is said to be in the mixed state. In this region, flux is able to penetrate the sample in quantized units of the flux quantum Φ_0 (the flux quantum will be elaborated later, in Section 2.2.4). This state is also referred to as the 'vortex state'. Between the second and third critical field, $H_{c2} < H < H_{c3}$, the interior of the sample is normal, while its surface layer is superconducting. Lastly, above its third critical field H_{c3}, superconductivity is fully destroyed.

Clean and Dirty Limit

Depending on the purity of the superconductor, the electronic mean free path varies. This mean free path length is compared to the BCS coherence length ξ_0. Two extreme cases are examined: First, in the clean limit ($l_{el} \gg \xi_0$), $\lambda(T)$ and $\xi(T)$ are

$$\lambda(T) = 0.71\frac{\lambda(0)}{\sqrt{1-\frac{T}{T_{c0}}}}, \quad \text{(2.35a)} \qquad \xi(T) = 0.74\frac{\xi_0}{\sqrt{1-\frac{T}{T_{c0}}}}, \quad \text{(2.35b)}$$

with $\lambda(0)$ defined in equation (2.28) at zero K. Second, in the dirty limit ($l_{el} \ll \xi_0$),

$$\lambda(T) = 0.64\lambda(0)\sqrt{\frac{\xi_0}{l_{el}(1-\frac{T}{T_{c0}})}}, \quad \text{(2.36a)} \qquad \xi(T) = 0.855\sqrt{\frac{\xi_0 l_{el}}{1-\frac{T}{T_{c0}}}}. \quad \text{(2.36b)}$$

In the previous equations, l_{el} is the value for the mean free electron path length and ξ_0 is the BCS coherence length, defined as $\xi_0 = \frac{\hbar v_F}{\pi\Delta(0)}$, with v_F the Fermi velocity and $\Delta(0)$ the width of the bandgap at zero K.

Linearized Ginzburg Landau equations

Saving us the torment of solving a pair of coupled non-linear partial differential equations (2.20 and 2.21), the linearized GL equation is introduced. By dropping the term $\beta|\psi|^2\psi$ in the first GL equation (2.20), the linearized GL equation is obtained:

$$\frac{1}{m}\left(\frac{\hbar}{i}\boldsymbol{\nabla} - q\boldsymbol{A}\right)^2\psi = -\alpha(T)\psi. \quad (2.37)$$

Since the superconducting order parameter, ψ, is small near the phase boundary, the linearized GL equation is a justified approximation near $T_c(H)$. The linearized GL equation will be discussed in more detail in the next section 2.2.3.

2.2.3 Superconductivity on the Mesoscale

Linearized GL Equation on the Mesoscale

The linearized GL equation, given by equation (2.37), is mathematically equivalent to the Schrödinger equation for a free particle of charge q, mass $m/2$ and in a vector potential $\boldsymbol{A}$, where $\boldsymbol{A}$ enters the Schrödinger equation through the canonical momentum operator $\boldsymbol{p} = -i\hbar\boldsymbol{\nabla} - q\boldsymbol{A}$. The α from equation (2.37) can be rewritten using the coherence length defined in equation (2.24):

$$-\alpha(T) = \frac{\hbar^2}{2m\xi^2(T)}, \tag{2.38}$$

with $-\alpha$ playing the same role for the superconducting wave function as the energy E for the Schrödinger wave function. The lowest E value corresponds to the maximum temperature at which the superconducting state can nucleate. Solving the Schrödinger equation in the presence of a magnetic field H, the lowest energy level corresponds to the lowest Landau level (E_{LLL}). This E_{LLL} reads:

$$E_{LLL}(H) = \frac{\hbar\omega}{2}, \tag{2.39}$$

where ω is the cyclotron frequency $\omega = \frac{q\mu_0 H}{m}$. Equating this lowest Landau level to $-\alpha$:

$$\frac{\hbar^2}{2m\xi^2(T)} = \frac{\hbar\omega}{2}. \tag{2.40}$$

Solving previous equation for the magnetic field, the critical field is obtained as a function of temperature:

$$\mu_0 H_{c2}(T) = \frac{\Phi_0}{2\pi\xi^2(T)}. \tag{2.41}$$

Previous formula indicates that the critical field, H_{c2}, depends linearly on temperature ($H_{c2}(T) \propto (T_c - T)$).

Tinkham Formula

The Tinkham formula [17, 28] describes the critical temperature as a function of magnetic field for a thin film of thickness w in a parallel magnetic field:

$$T_c(H) = T_{c0}\left[1 - \frac{\pi^2}{3}\left(\frac{w\xi(0)\mu_0 H}{\Phi_0}\right)^2\right] \tag{2.42}$$

However, the previous equation will be used for fields applied perpendicular to the thin film. In the case of a thin line of width w, a field applied perpendicular to the thin film is similar to a field applied in parallel to a film of thickness w. The same formula can thus be used for both [29].

Note that there is a discrepancy between the Tinkham formula (2.42) and the equation derived from the linearized GL equation (2.41). While the relation between critical field and temperature is linear in (2.41), the critical temperature in the Tinkham formula (2.42) is dependent on the square of the

applied field. This discrepancy can be understood from perturbation theory for sufficiently small fields [30]. These calculations present an energy shift in magnetic field $\Delta E = k_1 LH + k_2 SH^2$, where L is the orbital quantum number, S the area of the superconductor penetrated by the magnetic field and and k_1 and k_2 are constants. Due to the one-dimensional thin strip geometry, the states having a non-zero orbital momentum quantum number are suppressed. Therefore, the $L = 0$ state is strongly favored in these one dimensional geometries. The energy shift and thus the critical temperature is proportional to the field squared for thin strip geometries.

Pearl Length

In thin films, where the thickness is less or comparable to the penetration depth ($t \lesssim \lambda$), an effective penetration depth is introduced. The spatial distribution of the currents and magnetic field is governed by the Pearl length in thin films. This Pearl length, or effective penetration depth, λ_{eff}, is calculated as [31]:

$$\lambda_{eff} = \frac{2\lambda^2}{t}, \tag{2.43}$$

with λ the bulk value for the penetration depth and t the thickness of the thin film.

2.2.4 Fluxoid Quantization

A fascinating and crucial phenomenon for the working principle of the devices discussed in this work is the magnetic flux quantization in superconductors. Consider a hole through a bulk superconductor, presented schematically in Figure 2.4. When an external magnetic field is applied perpendicular to the plane of the figure, supercurrents are generated to exclude the magnetic field out of the interior of the superconductor. From equation (2.23), the phase gradient of the superfluid can be written as

$$\boldsymbol{\nabla}\theta = \frac{m}{\hbar|\psi|^2 q}\boldsymbol{j}_s + \frac{q}{\hbar}\boldsymbol{A}. \tag{2.44}$$

Furthermore, taking the contour integral of this equation along a contour C, as depicted in Figure 2.4:

$$\oint_C \boldsymbol{\nabla}\theta = \oint_C \frac{m}{\hbar|\psi|^2 q}\boldsymbol{j}_s + \oint_C \frac{q}{\hbar}\boldsymbol{A}. \tag{2.45}$$

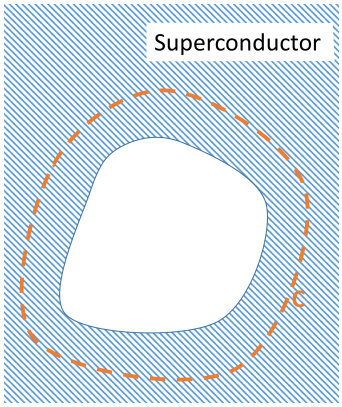

Fig. 2.4: *A superconductor (dashed area) with a hole. The dashed line marks the contour C around the hole through the interior of the superconductor.*

Since the wave function, $\psi = |\psi|e^{i\theta}$, must be single valued, the change of the angle θ after every full circle along any path in the interior of the superconductor has to be a multiple of 2π. This single valued restraint imposes a condition on the integral on the left hand side of equation (2.45): $\oint_C \boldsymbol{\nabla}\theta \cdot d\boldsymbol{l} = 2\pi n$, with n an integer ($n \in \mathbb{Z}$). Filling this restriction back into equation (2.45) and recalling Stokes's theorem

$$\oint_C \boldsymbol{A} \cdot d\boldsymbol{l} = \int_S (\boldsymbol{\nabla} \times \boldsymbol{A}) \cdot d\boldsymbol{S} = \oint_C \boldsymbol{B} \cdot d\boldsymbol{S} = \Phi, \tag{2.46}$$

the quantization of the fluxoid can be seen:

$$n\frac{h}{q} = \Phi + \mu_0\lambda^2 \oint_C \boldsymbol{j}_s \cdot d\boldsymbol{l}, \tag{2.47}$$

where the expression on the right hand side denotes the 'fluxoid'. Only at the surface layer of the superconductor, with a characteristic thickness of λ, does a non-zero magnetic field and supercurrent exist. When proceeding deeper into the interior of the superconductor, these quantities decrease exponentially and are essentially zero in the bulk of the superconductor. This allows to take a closed contour integral along C well into the interior of the superconductor while neglecting contributions from the supercurrent. In this case, the following relation is obtained:

$$\Phi = n\frac{h}{q} = n\Phi_0, \tag{2.48}$$

with

$$\frac{h}{q} = \frac{h}{2e} \equiv \Phi_0, \tag{2.49}$$

where Φ_0 is the magnetic flux quantum. This flux quantum is calculated solely from fundamental constants and its value is:

$$\Phi_0 = 2.067 \cdot 10^{-15}\ \mathrm{Tm}^2\,. \tag{2.50}$$

As was mentioned in Section 2.2.1, the experimental verification of the existence of the flux quantum was performed in 1961. This was the first experimental manifestation of the complex wave function $\psi = |\psi|e^{i\theta}$. Furthermore, these experiments determined the charge of the superconducting charge carriers q. This charge was found to be $2e$, corresponding to the charge of a Cooper pair predicted by the BCS theory.

2.2.5 Josephson Effect and Weak Links

This section discusses the Josephson effect and the junctions displaying this effect. First, Feynman's derivation from 1965 of the Josephson relations is followed [32]. In this derivation, tunnel junctions are considered. However, the Josephson relations hold whenever there are two superconducting baths weakly connected. Second, weak links connecting two superconducting baths are discussed. The Josephson relations are a second manifestation of the existence of a complex order parameter.

Feynman's Derivation

To introduce the equations describing the Josephson effect, the derivation of Feynman is followed [32]. Consider two superconductors, with the superconducting state described by two wave functions, ψ_1 and ψ_2, for superconductor 1 and 2, respectively. When these superconductors are separated by a sufficiently thick barrier, their time-dependent wave functions are described by two independent Schrödinger equations:

$$i\hbar\frac{d\psi_1}{dt} = H_1\psi_1, \tag{2.51a}$$

$$i\hbar\frac{d\psi_2}{dt} = H_2\psi_2. \tag{2.51b}$$

Each Hamiltonian, H_i, determines the time evolution of his respective wave function, ψ_i, independent of the other superconductor. Assume there is a voltage V applied over the two superconductors. It is plausible to assume that the zero potential point is located in the middle of the barrier. As a result,

superconductor 1 will be at a potential of $-\frac{1}{2}V$ and superconductor 2 at $\frac{1}{2}V$. Since a Cooper pair consists of two electrons, the potential energy of the Cooper pairs are respectively eV and $-eV$ in superconductor 1 and 2. Assuming now that the barrier is sufficiently small ($\lesssim 1$ nm) to induce coupling between the superconductors, the following equations

$$i\hbar\frac{d\psi_1}{dt} = eV\psi_1 + K\psi_2, \tag{2.52a}$$
$$i\hbar\frac{d\psi_2}{dt} = -eV\psi_2 + K\psi_1, \tag{2.52b}$$

describe the coupled superconductors with a potential, V, applied. In the previous equations, K represents the coupling constant for the wave functions across the barrier. Considering the previous discussion on the Ginzburg Landau formalism, the wave functions of both superconductors can be written in the following form:

$$\psi_1 = \sqrt{n_{c1}}e^{i\theta_1}, \tag{2.53a}$$
$$\psi_2 = \sqrt{n_{c2}}e^{i\theta_2}, \tag{2.53b}$$

$$\varphi = \theta_2 - \theta_1, \tag{2.54}$$

with n_{c1} and n_{c2} the Cooper pair density and φ the phase difference across the barrier. Now, substituting equations (2.53a) and (2.53b) into the coupled wave equations (2.52) and equating the imaginary and real parts separately, the following coupled equations are obtained:

$$\frac{d}{dt}n_{c1} = \frac{2K}{\hbar}\sqrt{n_{c1}n_{c2}}sin\varphi, \tag{2.55a}$$
$$\frac{d}{dt}n_{c2} = -\frac{2K}{\hbar}\sqrt{n_{c1}n_{c2}}sin\varphi, \tag{2.55b}$$

$$\boxed{\frac{d}{dt}\varphi = \frac{2e}{\hbar}V.} \qquad \text{(AC Josephson effect)} \tag{2.56}$$

Taking the difference of the time derivatives of the superconducting electron densities, a current density caused by these tunneling superconducting electrons can be obtained:

$$J = e\frac{d}{dt}\left(n_{c1} - n_{c2}\right), \tag{2.57}$$

which can be written as

$$\boxed{J = J_0 sin\varphi} \qquad \text{(DC Josephson effect)} \tag{2.58}$$

with

$$J_0 = \frac{4eK\sqrt{n_{c1}n_{c2}}}{\hbar}. \tag{2.59}$$

As a result, the two Josephson relations (equations (2.56) and (2.58)) are derived for this simple case. This elegant derivation by Feynman grasps the essence of the physics of two weakly coupled superconductors described by a coupling constant K. Since the current flowing through the junction

is equal to the current density times the cross section of the junction, equation (2.58) can be written as

$$I = I_0 sin\varphi \tag{2.60}$$

where $I_0 = J_0 S$, with S the junction cross section.

To end this derivation of Feynman, it is noted that equation (2.56) is derived from the main principles of quantum mechanics. It corresponds to experiments to a high degree of accuracy. It is no surprise that the National Institute of Standards (NIST) makes use of Josephson junctions to define the voltage standard. Equation (2.58) on the other hand is an approximate relation. Nevertheless, the current phase relation given by equation (2.58) is observed for various geometric structures of two weakly connected superconducting baths. Finally, note that (2.54) is not gauge invariant. The gauge invariant phase difference, φ^*, will be introduced when deriving the SQUID equations in Section 2.2.6.

Weak Links

A weak link is an electrical contact between superconducting electrodes which exhibit direct (non-tunnel-type) conductivity. A collection of weak links with various geometries is presented in Figure 2.5. An extensive review paper written by K. K. Likharev is dedicated to these superconducting weak links [33].

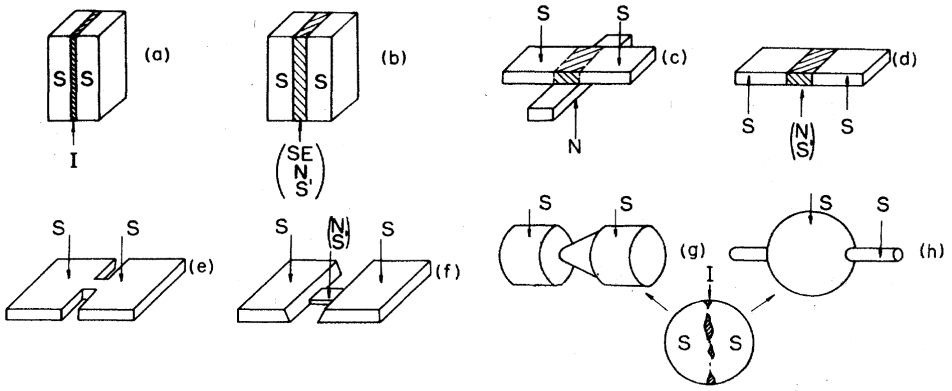

Fig. 2.5: *Various types of structures where the Josephson effect can take place.* ***(a)*** *tunnel junction considered in Feynman's derivation, with S a superconductor and I an insulator. The junctions from* ***(b)*** *to* ***(f)*** *have direct (non-tunnel) conductivity.* ***(b)*** *sandwich,* ***(c)*** *proximity effect bridge* ***(d)*** *ion implanted bridge,* ***(e)*** *Dayem bridge,* ***(f)*** *variable thickness bridge,* ***(g)*** *point contact and finally,* ***(h)*** *blob type contact. Figure taken from [33].*

From Figure 2.5 it is clear that there exists a broad spectrum of weak links connecting two superconductors. Each of these structures can exhibit the Josephson effect given in equations 2.58 and 2.56. The type of junction used in this work is classified as a Dayem bridge illustrated in Figure 2.5 **(e)**.

2.2.6 SQUID

The device under investigation in this thesis is a thin film aluminum direct current superconducting quantum interference device (DC SQUID). Combining two junctions that exhibit the Josephson effect in parallel as illustrated in Figure 2.6, a DC SQUID is obtained. This versatile device can measure any physical quantity that can be converted into a magnetic flux. In its essence, the SQUID is a flux to voltage converter, with a period of one flux quantum. Its working principle relies on two previously discussed phenomena, namely the Josephson effect and flux quantization in superconducting loops. Figure 2.6 illustrates a typical DC SQUID, where the two Josephson junctions, indicated in green, lie in parallel. This section discusses the classical DC SQUID derivation found in many textbooks.

Rewriting equation (2.23) using the definition of the flux quantum (2.48) and the London coefficient $\Lambda = m/(|\psi|^2 q^2)$, the gradient of the phase can be written as:

$$\boldsymbol{\nabla}\theta = \frac{2\pi}{\Phi_0}(\Lambda \boldsymbol{j_s} + \boldsymbol{A}). \tag{2.61}$$

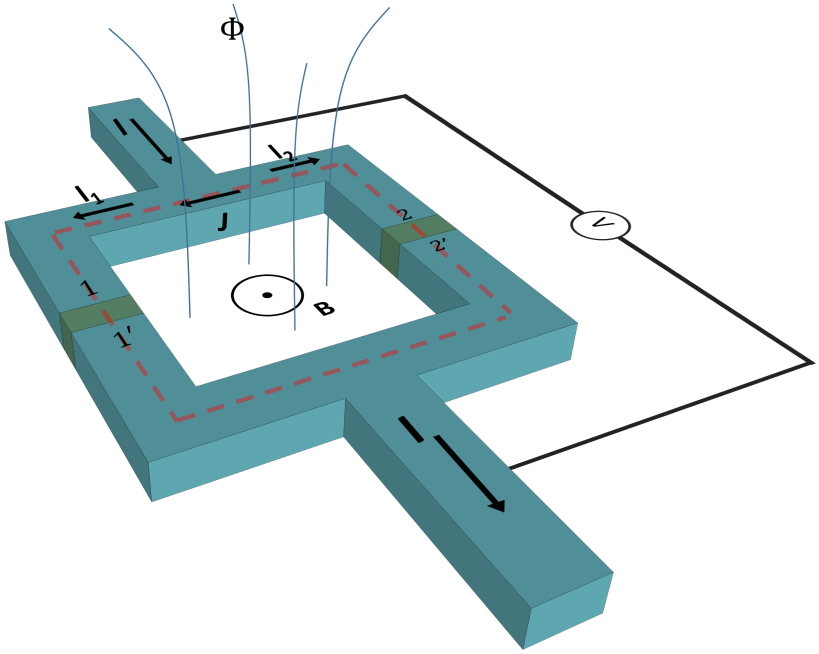

Fig. 2.6: *Schematic illustration of the DC-SQUID formed by two Josephson junctions in parallel.* $\boldsymbol{I}$ *presents the total current across the SQUID,* $\boldsymbol{J}$ *the circular current, anticlockwise along the red dashed path. The total current splits into two currents* $\boldsymbol{I}_1$ *and* $\boldsymbol{I}_2$*, going to the left and right Josephson junction, respectively. The interface locations of the Josephson junctions and superconductor are labeled as* 1*,* $1'$*,* 2 *and* $2'$*.* Φ *is the flux threading the SQUID,* $\boldsymbol{B}$ *the magnetic field and* V *the measured voltage across the SQUID.*

As discussed in the Section 2.2.4, the total phase change along a closed contour in a superconductor must be an integer multiple of 2π. By taking a path integral of the phase gradient (equation (2.61)) along the superconducting loop (dashed line in Figure 2.6), the phase difference between the starting

and end point of the path integral is found. Recalling the discussion on fluxoid quantization, the complex order parameter must be single valued: The total phase change along the closed contour is $2\pi n$, with n an integer.

$$\oint_C \boldsymbol{\nabla}\theta d\boldsymbol{l} = 2\pi n \tag{2.62}$$

$$= (\theta(1') - \theta(1)) + (\theta(2') - \theta(1')) + (\theta(2) - \theta(2')) + (\theta(1) - \theta(2)) \tag{2.63}$$

Introducing the gauge invariant phase difference $\varphi^* = \theta_b - \theta_a - \frac{2\pi}{\Phi_0}\int_a^b \boldsymbol{A}\cdot d\boldsymbol{l}$, the terms $\theta(1') - \theta(1)$ and $\theta(2) - \theta(2')$ in equation (2.63) can be written as:

$$\theta(1') - \theta(1) = \varphi_1^* + \frac{2\pi}{\Phi_0}\int_1^{1'} \boldsymbol{A}\cdot d\boldsymbol{l}, \tag{2.64}$$

$$\theta(2) - \theta(2') = -\varphi_2^* + \frac{2\pi}{\Phi_0}\int_{2'}^{2} \boldsymbol{A}\cdot d\boldsymbol{l}, \tag{2.65}$$

$$\tag{2.66}$$

where φ_1^* and φ_2^* are the gauge invariant phase differences over the first and second junction, respectively. The other terms in (2.63) are worked out using (2.61):

$$\theta(2') - \theta(1') = \int_{1'}^{2'} \boldsymbol{\nabla}\theta\cdot d\boldsymbol{l} = \frac{2\pi}{\Phi_0}\int_{1'}^{2'} \Lambda\boldsymbol{j}_s\cdot d\boldsymbol{l} + \frac{2\pi}{\Phi_0}\int_{1'}^{2'} \boldsymbol{A}\cdot d\boldsymbol{l}, \tag{2.67}$$

$$\theta(1) - \theta(2) = \int_{2}^{1} \boldsymbol{\nabla}\theta\cdot d\boldsymbol{l} = \frac{2\pi}{\Phi_0}\int_{2}^{1} \Lambda\boldsymbol{j}_s\cdot d\boldsymbol{l} + \frac{2\pi}{\Phi_0}\int_{2}^{1} \boldsymbol{A}\cdot d\boldsymbol{l}. \tag{2.68}$$

By substituting equations (2.64) - (2.68) into (2.63), one finds:

$$\varphi_1^* - \varphi_2^* = 2\pi n - \frac{2\pi}{\Phi_0}\oint_C \boldsymbol{A}\cdot d\boldsymbol{l} - \frac{2\pi}{\Phi_0}\int_{1'}^{2'} \Lambda\boldsymbol{j}_s\cdot d\boldsymbol{l} - \frac{2\pi}{\Phi_0}\int_{2}^{1} \Lambda\boldsymbol{j}_s\cdot d\boldsymbol{l}. \tag{2.69}$$

Recalling Stokes' theorem (equation (2.46)), previous equation reads:

$$\varphi_2^* - \varphi_1^* = 2\pi\frac{\Phi}{\Phi_0} + \frac{2\pi}{\Phi_0}\int_{1'}^{2'} \Lambda\boldsymbol{j}_s\cdot d\boldsymbol{l} + \frac{2\pi}{\Phi_0}\int_{2}^{1} \Lambda\boldsymbol{j}_s\cdot d\boldsymbol{l}, \tag{2.70}$$

where n has been set to 0 for convenience and Φ is the flux in the superconducting loop. The integration of the current density is along the red path excluding the insulating barrier. If the path can be chosen such that the current density is evaluated sufficiently far from the surface ($\gg \lambda_{eff}$), the last two integrals can be neglected. This is the case if the superconducting loop consists of a superconducting material with a width and thickness large compared to the effective penetration depth. In this scenario, a restriction on the phase difference is found:

$$\varphi_2^* - \varphi_1^* = 2\pi\frac{\Phi}{\Phi_0}. \tag{2.71}$$

The above equation (2.71) expresses the link between the two phase differences over the junction in order to satisfy fluxoid quantization in a superconducting loop. Furthermore, this relation allows us to reduce the number of independent variables, since φ_2^* can be written as $\varphi_1^* + 2\pi\frac{\Phi}{\Phi_0}$.

In this classical derivation of the DC SQUID, it is assumed that the Josephson junctions are identical and obey the current phase relation as expressed in equation (2.60), but since there is a non-zero vector potential $\boldsymbol{A}$, the gauge invariant phase difference must be used. In case of identical Josephson junctions, the critical currents are equal ($I_{0,1} = I_{0,2} = I_0$). Applying Kirchoff's law and using the DC Josephson relation (2.60):

$$I = I_1 + I_2 = I_0 \left[sin(\varphi_1^*) + sin(\varphi_2^*)\right] \tag{2.72}$$

$$= 2I_0 cos\left(\pi \frac{\Phi}{\Phi_0}\right) sin\left(\varphi_1^* + \pi \frac{\Phi}{\Phi_0}\right) \tag{2.73}$$

Inductance Parameter β_L

Due to the circular geometry characteristic to all SQUIDs, the superconducting loop has a non-zero self-inductance. As a consequence, the flux through the superconducting loop is not only the flux applied by the external field, but also the flux created by the circulating currents. Taking into account the finite inductance of the superconducting loop, the flux threading the loop is

$$\Phi = \Phi_{ext} + LJ, \tag{2.74}$$

$$\text{with } J = (I_1 - I_2)/2 \tag{2.75}$$

where L is the loop inductance and J the circulating current, defined as $(I_1 - I_2)/2$. The dimensionless parameter describing the impact of the SQUID's inductance is its inductance parameter β_L. It is defined as

$$\beta_L = \frac{2LI_0}{\Phi_0}. \tag{2.76}$$

This parameter expresses the ratio of the flux generated by the maximum circulating current, LI_0, over half a flux quantum $\Phi_0/2$.

In the special case, where $\beta_L \ll 1$, the flux generated by the circulating currents is small compared to the flux quantum. Therefore, the flux threading the superconducting loop is approximately equal to the applied flux. In this small inductance limit, $\Phi \approx \Phi_{ext}$ and equation 2.71 reads $\varphi_2^* = \varphi_1^* + 2\pi\frac{\Phi_{ext}}{\Phi_0}$. Recalling equation 2.73 and assuming identical Josephson junctions ($I_{0,1} = I_{0,2} = I_0$), the maximum critical current of the SQUID is found by maximizing equation 2.73 with respect to φ_1^* ($dI/d\varphi_1^* = 0$).

$$I_c(\Phi_{ext}) = 2I_0 \left| cos\left(\pi \frac{\Phi}{\Phi_0}\right) \right|. \tag{2.77}$$

In many other cases, where the induced flux generated by the circulating current J is not negligible (or equivalently, $\beta_L \gtrsim 1$), the flux threading the superconducting loop is expressed in equation (2.74). The total flux threading the loop can be written as a function of Φ_{ext} and φ_1^*. Again, assuming identical Josephson junctions, the flux is written as:

$$\Phi = \Phi_{ext} - LI_c sin\left(\pi \frac{\Phi}{\Phi_0}\right) cos\left(\varphi_1^* + \pi \frac{\Phi}{\Phi_0}\right). \tag{2.78}$$

The above equation (2.78), combined with equation (2.77), determine the behavior of the DC SQUID. In order to find the critical current as a function of the externally applied field, these equation need

to be solved self consistently. To work out the maximum super current that can be pushed through the SQUID structure as a function of the external field ($I_c(\Phi_{ext})$), one has to find the maximum of the total current I with respect to φ_1^*. However, one has to take into account the restriction imposed by equation (2.78). These equations were first solved by R. De Bruyn Ouboter and A. Th. A. M. De Waele [34]. In the next section, a more general version of the DC SQUID, the asymmetrical DC SQUID, will be examined in more detail.

2.2.7 Asymmetric SQUID

Going beyond the classical textbook derivation of the DC SQUID, this section introduces a model for a SQUID with asymmetric Josephson junctions. This model will be used to analyze the experimental data in section 5. Considering the discussion and results in Section 4.4, it is plausible to assume that the weak links will not reduce their dimensions exactly simultaneously. Introducing an asymmetry in the Josephson junctions is a key factor in understanding the behavior of the structure under investigation in this work. The circuit diagram for the asymmetric SQUID model is presented in Figure 2.7. This model is based on the works of [35].

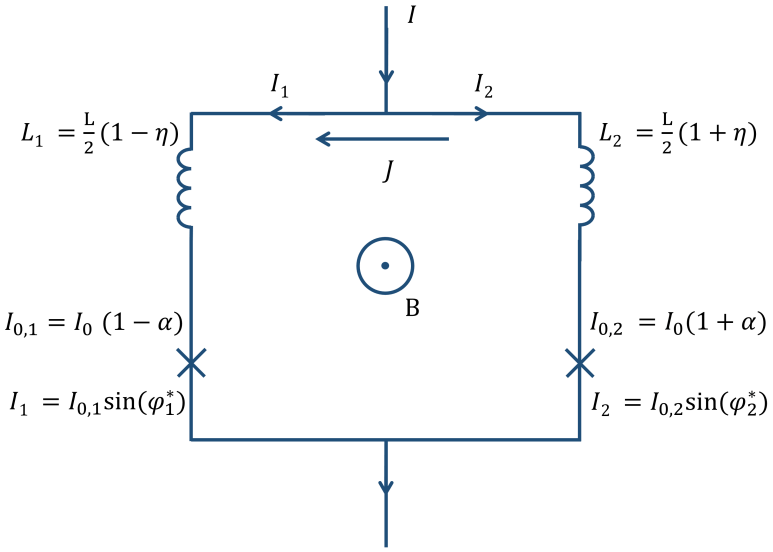

Fig. 2.7: *Circuit diagram of the asymmetric SQUID model. A current I is injected into the SQUID structure and splits into two currents, I_1 and I_2, going to the left and right Josephson junction, respectively. The α is the asymmetry parameter for the critical current, η is the asymmetry parameter for the difference in inductance between the left and right branch. B is the magnetic flux density in the loop of the SQUID. J is the circulating current. The total inductance L is the sum of the inductances in the branches.*

Using again Kirchoff's law, it is found that the the total current I is equal to the sum of the currents flowing through the branches: $I = I_1 + I_2$. In this model, ideal Josephson junctions are assumed. In the case of ideal junctions, the relation between phase and current is as depicted in Figure 2.7, where the current is proportional to the sin of the gauge invariant phase difference over the junction, φ_i^*. This circuit diagram will be the start of our model. The parameters of the model are the total

inductance of the loop L, its corresponding asymmetry parameter η, the critical current density of the junctions I_0 and its associated asymmetry parameter α. The total supercurrent through the SQUID is found to be:

$$I = I_1 + I_2 = I_{0,1}sin(\varphi_1^*) + I_{0,2}sin(\varphi_2^*) \tag{2.79}$$

$$I = I_0\left[(1-\alpha)sin(\varphi_1^*) + (1+\alpha)sin(\varphi_2^*)\right] \tag{2.80}$$

where, dependent on the α parameter, the left or right Josephson junction has a higher critical current. The α asymmetry parameter can take any value between -1 and 1, ranging from the extreme asymmetry cases for -1 and 1, with zero, the symmetrical SQUID, in between these extremes. The same principle applies for the η parameter. However, the η parameters expresses the asymmetry in the inductance in each branch.

To investigate the effect of these parameters on the critical current of the SQUID in applied field $(I_c(\Phi_{ext}))$, each parameter is examined in detail. The parameters introduced so far are the inductance parameter β_L, the critical current asymmetry parameter α and the inductance asymmetry parameter η. The investigation of their influence on the SQUID properties is started by taking a closer look in the limiting case of $\beta_L \ll 1$.

Small Inductance Limit $\beta_L \ll 1$

From the discussion in the previous section on this small inductance limit, the flux threading the SQUID was found to be approximately equal to the applied flux ($\Phi \approx \Phi_{ext}$). This approximation is valid due to fact that the circulating currents generate a flux small compared to the flux quantum. Furthermore, in this limit the inductance parameter η does not have a physical meaning. There is only a very small, negligible, inductance. It has no meaning to point out in which branch this negligible inductance is located. The only parameter left to discuss is the asymmetry parameter of the critical current α. Using the relation (2.71) where $\Phi = \Phi_{ext}$ and equation 2.80, one can find the maximum critical current through the SQUID by the condition $dI/d\varphi_1^* = 0$. The details of this calculation can be found in Appendix A. The result is the critical current of the SQUID as a function of the applied flux:

$$I_c(\Phi) = \sqrt{(I_1 - I_2)^2 + 4I_1I_2cos^2\left(\pi\frac{\Phi}{\Phi_0}\right)}, \tag{2.81}$$

$$= 2I_0\sqrt{\alpha^2 + (1-\alpha^2)cos^2\left(\pi\frac{\Phi}{\Phi_0}\right)}. \tag{2.82}$$

The above equation (2.82) is illustrated in Figure 2.8 for different values of α. The effect of α on the shape and depth of the modulation of $I_c(\Phi_{ext})$ is readily visible.
To understand the critical current behavior of the asymmetric SQUID in the small inductance limit, the critical current of the symmetrical SQUID is discussed first. Consider the purple curve in Figure 2.8. This curve corresponds to the symmetrical case where $\alpha = 0$ and the Josephson junctions are thus identical. The formula for this behavior has already been derived in equation (2.77) and is equivalent to equation (2.82) with $\alpha = 0$. In the more general case, where the Josephson junctions are not identical, α has a nonzero value. For example, if $\alpha = 0.5$ then, $I_{0,1} = 0.5I_0$ and $I_{0,2} = 1.5I_0$. The critical current of the asymmetrical SQUID with $\alpha = 0.5$ is plotted as the red curve in Figure 2.8.

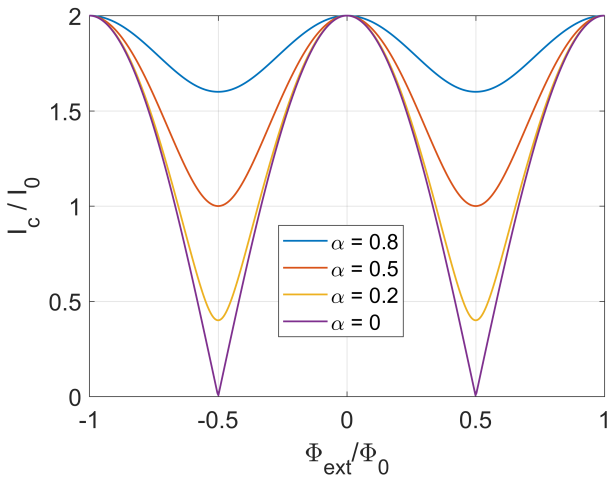

Fig. 2.8: *Effect of the critical current asymmetry parameter α on the critical current of the SQUID in externally applied field in the small inductance limit ($\beta_L \ll 1$).*

The impact of the asymmetry compared to the symmetrical SQUID curve ($\alpha = 0$ curve) can be seen from the shape and modulation depth. The $\alpha = 0.5$ curve is smooth and does not go to zero in case of half integer values for the flux quanta applied. Formula (2.82) provides the value of the critical current at any value for the applied flux and α in the small inductance limit. Note that equation (2.82) produces the same behavior for α and $-\alpha$.

Non-negligible Inductance $\beta_L \gtrsim 1$

When the flux generated by the circular supercurrent, J, is of the same order of the flux quantum (or equivalently: $\beta_L \gtrsim 1$), the flux threading the SQUID is no longer equal to the externally applied flux as was assumed in the previous section. The flux in the superconducting loop obeys the relation presented in equation (2.78). Analyzing the circuit diagram, the effective flux threading the superconducting loop is found using equation (2.75) and the relations defined in Figure 2.7.

$$\Phi = \Phi_{ext} + LJ - \frac{\eta}{2} LI \tag{2.83}$$

$$= \Phi_{ext} + \frac{\beta_L}{4}[(1-\eta)(1-\alpha)sin(\varphi_1^*) - (1+\eta)(1+\alpha)sin(\varphi_2^*)]. \tag{2.84}$$

Equations (2.80) and (2.84) combined with the fluxoid quantization restraint (equation (2.71)) determine the behavior of the critical current of the asymmetrical SQUID in an applied field. For a given externally applied flux, there exist a set of solutions consisting of couples $\{(\varphi_1^*, \Phi)\}$ which satisfy equation (2.84). The correct solution is that particular couple, (φ_1^*, Φ), having the maximum supercurrent through the SQUID with respect to the supercurrent found from the other solutions in $\{(\varphi_1^*, \Phi)\}$.

The solving technique of equations (2.80) and (2.84) presented above correspond to the methods implemented in a script written in Matlab. Using numerical methods, i.e. Matlab, the $I_c(\Phi_{ext})$ plots are made and the effect of the parameters is investigated. In case of a symmetrical SQUID, the effect of the β_L parameter is illustrated in Figure 2.9. The modulation depth ΔI_c illustrated in Figure 2.9

(b) is defined as $2I_0 - I_c(\Phi_0/2)$.

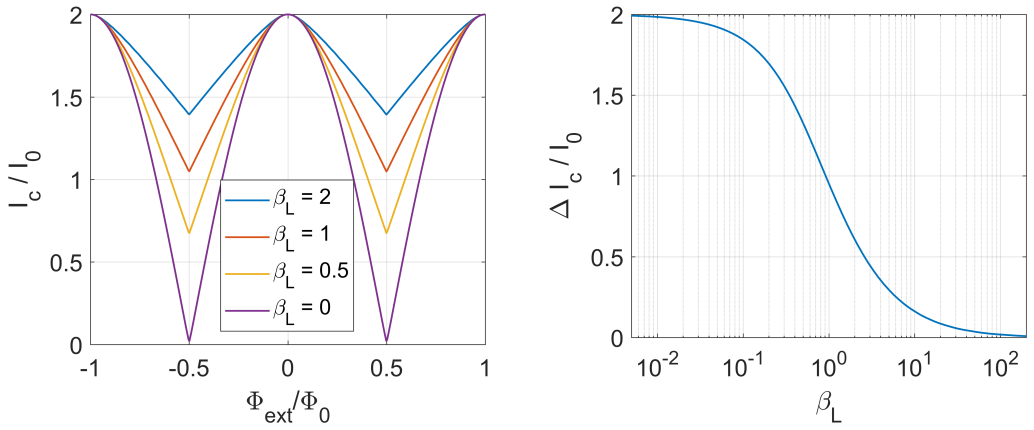

Fig. 2.9: ***(a)*** *Effect of the inductance parameter β_L on the critical current of the SQUID in externally applied field in the case of a symmetrical SQUID ($\alpha = 0$ and $\eta = 0$).* ***(b)*** *Modulation depth of the critical current oscillations as a function of β_L in a symmetrical SQUID.*

Curves of I_c as a function of the external flux Φ_{ext} for variable α and η with $\beta_L = 1$ appear in Figures 2.10 **(a)** and **(b)**, respectively. One can see from the plots presenting the effect of the parameters that the maximum current flowing through the SQUID remains at $2I_0$, whatever the value for α, β_L and η. Note that to achieve this maximum current $2I_0$, equation (2.80) implies that both phases, φ_1^* and φ_2^*, must be equal to $\pi/2$. As a consequence, the circulating current (2.75) is $J = -\alpha I_0$ and the maximum current $2I_0$ occurs at $\Phi_{ext} = \beta_L(\alpha + \eta)/2$. Hence, the maximum of the characteristic $I_c(\Phi_{ext})$ is shifted along the Φ_{ext}-axis compared to the symmetric SQUID, where I_c is maximum at $\Phi_{ext} = 0$.

2.2.8 Phase Slips

The discussion above is restricted to the zero voltage state of the SQUID. Below the critical surface (i.e. in the superconducting state), it was told that a superconductor has zero resistance in this zero voltage state and currents can flow without dissipation. However, certain phenomena exist which can cause premature destruction of the condensate even below this critical surface. An example of such a phenomenon are phase slips. By temporarily breaking op the superconducting condensate, the phase of the superconducting condensate varies by 2π and due to the Josephson relation defined in (2.56), a voltage appears over the superconductor. The phase slip event causes a premature suppression of the superconducting properties, since it breaks the long-range order of the phase. A phase slip event in a superconductor is schematically illustrated in Figure 2.11.

Thermally Assisted Phase Slips (TAPS)

The occurrence of these 'superconducting fluctuations' can partly be attributed to thermal excitations, partly to quantum tunneling through a barrier, depending on the cross section of the wire. The

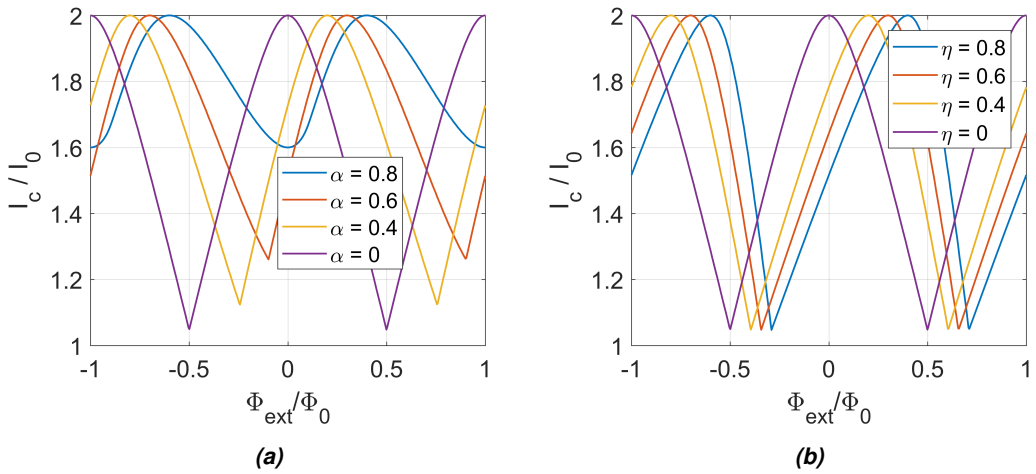

Fig. 2.10: ***(a)*** *Effect of the asymmetry parameter α on the critical current of the SQUID in externally applied field with $\beta_L = 1$ and $\eta = 0$.* ***(b)*** *Asymmetry parameter η influence on the critical current of the SQUID in externally applied field with $\beta_L = 1$ and $\alpha = 0$.*

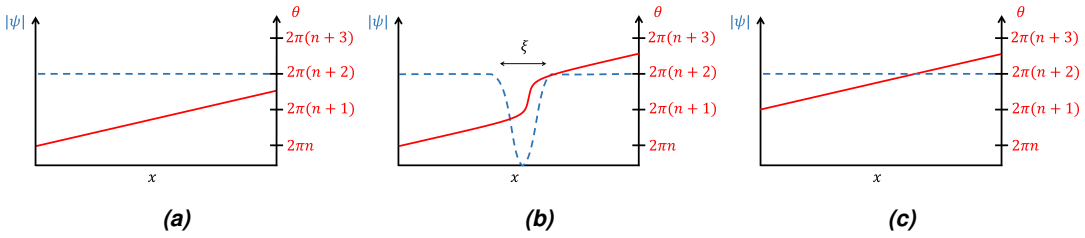

Fig. 2.11: *A phase slip event in a current carrying wire. Spatial variation of the wave function ψ is presented in blue, phase θ in red.* ***(a)*** *illustrates the phase and amplitude of the wave function before the phase slip event,* ***(a)*** *presents the situation during the event and* ***(c)*** *after the phase slip event. Figure reconstructed from [36].*

slippage of the superconducting phase is accompanied by the local suppression of the superconducting condensate. When a thermal excitation excites the quasiparticles in a region of dimensions ξ and effectively suppresses the superconducting state, the phase is unrestricted and can jump by the value $2\pi n$, where n is an integer. After this phase slip event, the superconducting state condenses again to the more energetically favorable state. The phase is stitched back together again to form a constant gradient. However, the net shift of the phase with respect to the time before the phase slip event is $2\pi n$. Each such a phase slip event creates a non-zero voltage over the superconductor according to the Josephson relation (2.56). In the absence of a bias current, there is a zero phase gradient (recall equation (2.23), from which can be seen that $\boldsymbol{I} \propto |\psi|^2 \boldsymbol{\nabla}\theta$). Without any phase gradient, the probability for a 'positive phase slip' ($n = +1$) is equally large as a 'negative phase slip' ($n = -1$) to occur. The net voltage over the superconductor is thus zero. When a bias current is present, or equivalently, a non-zero phase gradient exists, an asymmetry arises in the probability for the type of

phase slip to occur. As a result, a non-zero voltage drop is measured over the superconductor due to TAPS.

When these phase slips are thermally activated, the measured resistance can quantitatively be described by the theory of Lamber-Ambegaokar-McCumber-Halperin for a one dimensional wire ($\sqrt{S} < \xi(T)$, with S the cross section of the wire). The resistance due to TAPS is in this theory:

$$R \propto \Omega exp\left(-\frac{\Delta F(T)}{k_B T}\right), \tag{2.85}$$

where $\Omega \propto [L/\xi(T)]\left[\Delta F(T)/k_B T\right]^{1/2}(T_c - T)^{-1}$ is the attempt frequency, L is the length of the constriction and $\Delta F(T) \propto H_c^2(T) S\xi(T)$ is the free energy barrier which needs to be surmounted to suppress superconductivity in a volume $S\xi(T)$. Little was the first to point out a non-zero resistance of a quasi one-dimensional superconducting wire below the critical surface due to the mechanism of phase slips [37].

These thermally assisted phase slips also cause broadening of the superconducting phase transition measurements in systems of reduced dimensions. Since TAPS occur more frequently close to T_c, the broadening dominates near the critical temperature and fades away as the temperature is decreased. This dissipation effect below the critical surface and the broadening of the superconducting transition are only a few examples of how these phase slips manifest themselves. These and other effects are studied in the paper of Baumans et al. [38], where phase slips in superconducting junctions similar to the weak links used in this work are investigated.

Quantum Phase Slips (QPS)

It was shown by Baumans et al. [38] that for free energy barriers which are sufficiently small, the TAPS model does not reproduce their measurements. The mechanism responsible for the resistance measured below the critical surface was attributed to quantum phase slips (QPS). Once this barrier $\Delta F(T)$ is sufficiently reduced, instead of overcoming this barrier by thermal excitations, the laws of quantum mechanics allow the phase to tunnel through the barrier. It was shown that the condition on the energy barrier to be 'sufficiently' small is a cross section of the superconducting wire less than ~ 150 nm^2. The reduction of the free energy barrier $\Delta F(T)$ was achieved by reducing the cross section via electromigration.

Chapter 3

Experimental Details

This chapter briefly discusses the experimental methods and devices used in the current work. First, the sample fabrication techniques are discussed. These fabrication techniques include Electron Beam Lithography (EBL) to fabricate the mask and Molecular Beam Epitaxy to deposit the aluminum. EBL is described in Section 3.1.1 and Molecular Beam Epitaxy (MBE) is described in Section 3.1.2. Second, the sample characterization methods are discussed. Atomic Force Microscopy is discussed in Section 3.2.1 and the Scanning Electron Microscope (SEM) in Section 3.2.2. Third, the setup and methods used for controlled electromigration are introduced. These consist of sample mounting, discussed in Section 3.3.1, a layout of the measurement scheme, discussed in Section 3.3.2, the electromigration software discussed in Section 3.3.3 and the Physical Property Measurements System (PPMS), discussed in Section 3.3.4. Lastly, the devices for characterizing the superconducting properties of the SQUID are discussed. The Heliox ^{3}He cryostat is discussed in Section 3.4.1, the techniques for transport measurements are discussed in Section 3.4.2.

3.1 Sample Fabrication

The samples under investigation consist of either a gold (Au) or aluminum (Al) nanostructures on top of a Si/SiO_2 substrate (7×7 mm^2). The top SiO_2 layer has a thickness of (300 ± 25) nm. The Si layer has a thickness of (750 ± 50) µm. The Au nanostructures were fabricated by Au deposition on a mask provided by imec. These Au nanostructures are used to demonstrate the power and flexibility of the electromigration software. The Al nanostructures are designed and fabricated in house using the techniques described below.

3.1.1 Electron Beam Lithography (EBL)

The first step towards the fabrication of an Al nanostructure is the creation of a mask. Since EBL has the required high resolution needed to fabricate nanoscale structures, it is an appropriate choice.

The working principle of EBL can be summarized as follows [39]: A highly focused electron beam scans the sample covered with resist material according to a predefined two dimensional pattern. The exposure of this resist material to the electron beam dramatically changes its solubility in a subsequent development bath. This process is illustrated schematically in (a), (b) and (c) of Figure 3.1.

The resist layers are classified as positive for increasing solubility and negative for decreasing solubility

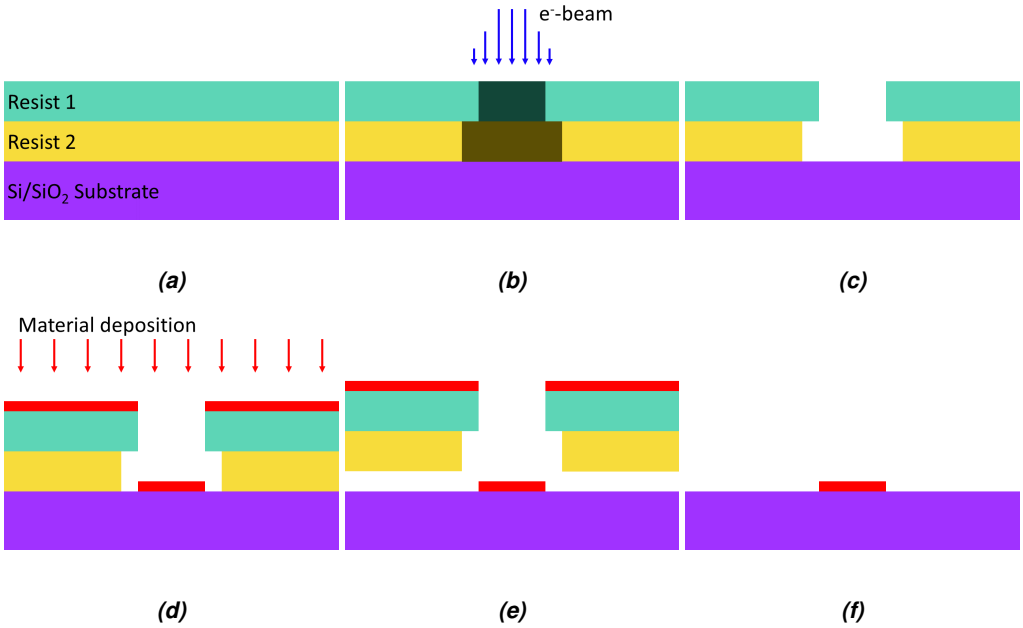

Fig. 3.1: *Electron Beam Lithography (EBL) and material deposition for creating nanostructured thin films.* ***(a)*** *Resist layers (yellow and green) are spin-coated on the substrate.* ***(b)*** *An electron beam writes the desired structures in the resist layers, inducing changes of their chemical properties.* ***(c)*** *After development the exposed area's are removed.* ***(d)*** *The desired material (red) is deposited on the resist layers and substrate.* ***(e)*** *Lift-off removes the remaining resist.* ***(f)*** *Only the structures remain on the substrate.*

as a result of the electron beam exposure. In the case of positive resist layers, these layers are removed during the development process from the area's corresponding to the predefined pattern, leaving the substrate exposed. After the development process, the desired material is deposited on the patterned mask. The final step is to remove the trilayer consisting of the two resist layers and the deposited material in a chemical bath. After this so-called lift-off process, the nanostructured thin film remains solely on the sample. These last three steps are illustrated in (d), (e) and (f) of Figure 3.1.

The mask fabrication was executed in the clean room of Leuven NanoCentre using the Raith eLine Plus [40]. Positive resist layers were spin-coated and subsequently baked ($130°C$ for 2 min.) on the substrate. The thickness of the resist bilayer is approximately 300 nm. The upper and lower resist layers (i.e. Resist 1 and Resist 2 in Figure 3.1 (a)) correspond here to PMMA and PMMA-MA, respectively, with PMMA consisting of polymers approximately 20 times longer than PMMA-MA. Due to this difference in polymer length, the PMMA-MA resist layer has increased solubility sensitivity to the electron beam. This difference in e-beam sensitivity can be seen in (b) and (c) of Figure 3.1 as the formation of an upside down mushroom-like gap. The developer used to remove the exposed resist was a 1:1 mixture of MIBK and IPA. The choice of this bilayered resist and subsequent mushroom formation facilitate the lift-off process, performed using an ultrasound acetone bath. The material deposition technique was performed using MBE and is discussed in the following section (3.1.2).

3.1.2 Molecular Beam Epitaxy (MBE)

Molecular beam epitaxy is a high purity material deposition technique. It allows to grow epitaxial thin films using atomic and molecular beams in ultra high vacuum. Evaporation of the solid targets create a molecular beam in which material is transported to the substrate. It is capable of single monolayer deposition. The employed system for molecular beam epitaxy is the RIBER SDS 32 [41]. It is located in the KU Leuven Ion and Molecular Beam Lab (IMBL) [42]. Here, it is used to deposit a few tens of nm thick Al on the patterned masks.

Since MBE requires ultra high vacuum, the deposition chamber is connected to the IMBL's UHV transport system. The base pressure in this system is typically $5 \cdot 10^{-11}$ Torr. This UHV system consists out of several preparation and surface analysis facilities. The masks are loaded into the UHV system by means of a load-lock. After mounting the samples on specialized sample holders, the load-lock is depressurized by a combination of a scroll pump and a turbo pump. Magnetically guided trains transport the mask to the deposition chamber of the MBE.

This MBE system has several Knudsen cells and two electron beam guns installed, giving the possibility to evaporate a wide variety of materials. The Knudsen effusion cell heats the containing solid material, which will form the molecular beam due to melting and vaporization or sublimation. In the electron beam gun cells, the molecular beam is formed in a similar manner. In this case however, the desired material is heated by means of electron bombardment. Electrons are released from a current carrying wire and guided on the target material using electric and magnetic fields. This second type of cell is used to create the aluminum molecular beam.

The beam current and composition is monitored before the start of deposition by a quadrupole mass filter. The growth rate is monitored using a quartz microbalance. The desired thickness of the nanostructured thin film can thus be achieved by tuning the deposition time and beam current.

3.2 Sample Characterization

The results of the fabrication process are investigated using two complementary surface characterization techniques: Atomic force microscopy (AFM) and scanning electron microscopy (SEM). The AFM technique allows to determine the surface topography of the nanostructure to the nanometer level. However, its lateral resolution lacks this precision and is of the order of ten nanometer. While the thickness of the nanostructure cannot be measured using SEM, its lateral resolution exceeds that of the AFM by an order of magnitude. Combined, these techniques provide high precision information on the geometry of the fabricated nanostructures.

3.2.1 Atomic Force Microscopy (AFM)

Scanning probe microscopy (SPM) incorporates a large assortment of techniques for investigating properties at or near the sample surface. In SPM techniques, a sharp tip mounted on a cantilever probes a sample surface. Forces acting on the tip are detected and mapped into a 2D image. Different modes of SPM are available which map different interactions. These techniques can examine surface topography, adhesion, elasticity, surface charge, piezoresponse, etc. AFM is an example of such a surface characterization technique to determine surface topography.

The basic components of a scanning probe microscope are the cantilever with tip, the position

sensitive photodetector (PSPD) and a laser. The laser beam is reflected on the back of the cantilever while the tip is scanning the surface. Due to the interaction between tip and sample, the cantilever deflects and changes the direction of the laser's reflection. Consequently, the laser signal on the photodetector changes it's position on the sensor. This position sensitive photodetector is able to determine the position change caused by cantilever deflection. Depending on the SPM technique applied, the PSPD can measure direct deflection or vibration amplitude, frequency and phase using a Lock-in Amplifier (LIA). Based on these measured quantities, a feedback signal can be applied to the Z-scanner. Finally, these feedback signals and measured quantities determine the topography or the relevant interaction strengths.

The scanning motion is provided by piezocrystals. High resolution actuators can position the cantilever's tip with nanometer lateral precision. The actuators move the probe over the sample in a back and forth raster scanning method. The deflection (and/or torsion) of the cantilever due to tip-sample interaction is recorded for each X,Y pair. The collection of data points form a SPM image. The actual lateral resolution is limited by the radius of the tip, which is typically less than 10 nm. The height resolution is far more superior and can go to sub-nanometer resolution.

An AFM can operate in three different modes: Non-contact, tapping (or intermittent) and contact mode. The dominant forces in AFM are the Van der Waals force and the force due to the Pauli exclusion principle. In this work, the topography of the nanostructured thin film is mapped in the non-contact (NC) operational mode of the AFM, where the attractive forces are dominant.

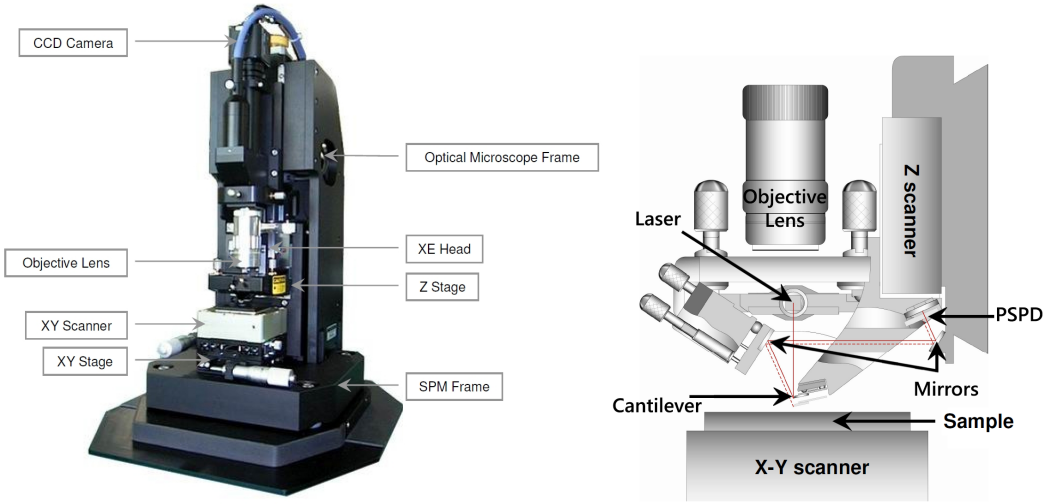

(a) ***(b)***

Fig. 3.2: ***(a)*** *Park Systems XE-100 scanning probe microscope.* ***(b)*** *A schematic illustration of the main components of the XE-100 SPM. The separation of the Z scanner from the X-Y scanner, a distinctive feature of the XE-series, is readily visible. Figures taken from [43].*

As the name suggests, the distance between tip and sample during scanning is relatively large in NC mode. The advantage of the NC mode over contact is that there are no significant changes occurring to the sample as a result of tip-sample interaction. The tip lifetime is also considerably

higher in NC mode. NC AFM cantilevers typically have a resonant frequency between 100 kHz and 400 kHz. The oscillations are driven using a bimorph, mechanically attached to the cantilever. Due to the attractive forces between tip and sample, the resonant frequency shifts. An effective spring constant $k_{eff} = k_0 - F'$ can be introduced, with k_0 the intrinsic spring constant and F' the force gradient. Note that the effective spring constant shifts to lower values for decreasing sample-tip distance, because the force gradient is larger for shorter distances in NC mode.

Since the resonance frequency of the cantilever is intimately linked with its spring constant, the resonance peak shifts to lower values when the sample-tip distance decreases. This behavior can be seen from the resonance frequency of a 1D harmonic oscillator $f = \sqrt{k/m}$, with k the spring constant and m the oscillating mass. Choosing a driving frequency halfway down on the right side of the resonance peak (amplitude vs. frequency), a high sensitivity to the attractive forces is realized. In this manner, a small shift in resonance frequency due to sample-tip forces results in a significant change in vibration amplitude. This vibration amplitude and frequency shift is measured with the PSPD. When operating in amplitude modulation, a feedback system controls the z-scanner to keep the vibration amplitude constant. This feedback signal is the requested topography signal.

The employed scanning probe microscope is the Park Systems XE-100 [43], presented in Figure 3.2. The AFM was configured in non-contact, amplitude modulation mode to characterize sample topography.

3.2.2 Scanning Electron Microscopy (SEM)

Scanning electron microscopy is a nanometer resolution imaging technique based on a highly focused high energy electron beam scanning the specimen [44]. Free electrons are typically generated by a tungsten filament, LaB_6 or Schottky emitter, or a tungsten field-emission tip and is commonly called the electron gun. These free electrons are then accelerated, condensed into a narrow beam, focused and scanned over the sample surface by means of condensers and electromagnetic lenses. Since the mean free path of the electrons must be larger than their traveling distance from e-gun to sample, the lens column and sample chamber are held in vacuum. In order to create an image, raster scanning of the electron beam sequentially covers a rectangular area on the specimen. Intensities of X-rays and electrons emitted from each spot are then stored as pixels in a 2D image. A beam diameter of the order of 10 nm is typical and 1 nm is possible with a field-emission source. This parameter is a crucial factor to the SEM's resolution limit. The main elements of a SEM are presented schematically in Figure 3.3.

When the high energy electrons, typically 1 to 100 keV, enter the solid both elastic and inelastic scattering occurs. An incident electron has a small probability of colliding head-on (low impact parameter) with an atomic nucleus. Due to the low electron mass relative to the mass of the nuclei, energy and momentum conservation dictates that these primary electrons are backscattered and have only lost a fraction of their initial kinetic energy. These backscattered electrons are collected by a detector and their intensity is called the backscattered electron (BSE) signal. Since the inelastic scattering mean free path length (or escape depth) is only a few tens of nanometer, the elastically backscattered electrons provide information on the surface. When an incident electron collides with an atomic electron, the primary (incoming) electron can release the secondary electron from its bound orbit. Additional energy transferred from the incoming to the secondary electron besides the orbital binding energy is the final kinetic energy of the secondary electron. This allows the secondary electrons to travel through the solid. Upon their escape from the solid into the vacuum, these secondary electrons are collected and labeled as the secondary electron (SE) signal.

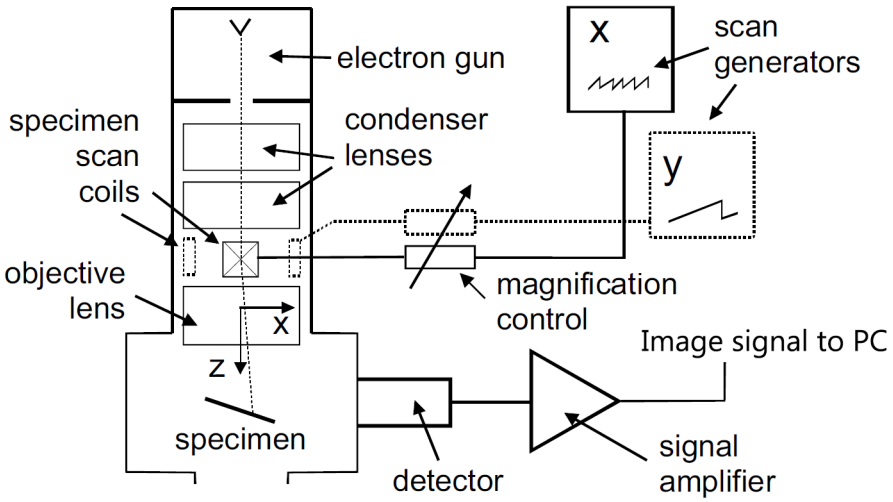

Fig. 3.3: *Schematics of a Scanning Electron Microscope (SEM). On the left the sample chamber and lens column are illustrated. The right side illustrates the scanning controls and detection setup. Figure taken from [44].*

After the collision with the primary electron, the secondary electron has an energy of typically 100 eV. The range of the electrons can be expressed as a function of initial energy E_0 [45]:

$$R = \frac{K}{\rho} E_0^{\gamma} \tag{3.1}$$

where ρ is the density, K is a material-independent constant, and γ varies from 1.2 to 1.7. This range is defined as the distance the electron can travel in the sample along a trajectory. Ranges of the high energy incident electrons are generally of the order of a micron, depending on the specimen material and electron energy. However, the electrons detected as back scattering electrons are the electrons which have only lost a fraction of their initial kinetic energy. Any inelastic collisions within the specimen will remove electrons from the group of backscattered electrons. These backscattered electrons penetrated the specimen and have collided only a few tens of nm deep into the solid. The BSE signal thus provides information of the specimen near its surface. Channeling can cause these collisions to occur deeper into the solid. Secondary electrons have an even smaller range. Typical escape depths of the low-energy secondary electrons in Si and Al for example are on the order of 1 nm. This implies that the collected secondary electrons were created just below or at the surface. Imaging of these secondary electrons thus provide information of the surface of the sample. The SE image is said to display topographical contrast.

Contrast in an SE image is due to modulation of the number of electrons created in a certain area. This modulation originates from any property that alters its response to the electron beam. The secondary electron yield (the average number of escaping secondaries over incident electrons) changes with chemical composition and the angle between incident beam an surface normal. Since the SE yield determines the SE intensity, these two factors govern the contrast of the SE SEM image.

In practice however, the secondary electron collector is located to one side of the column, giving an

asymmetry to the SE SEM setup. Surfaces tilted towards the detector appear at a higher intensity than other surfaces, due to electrons emitted from these surfaces having a greater probability of reaching the detector. This also affects contrast modulation and creates a shadow effect, which can facilitate the interpretation of the 2D image as a 3D surface topography.

The employed SEM is the same device as the EBL device discussed in Section 3.1.1, that is the Raith eLine Plus located at Leuven NanoCentre. Since SEM and EBL rely on an high energy electron nanoprobe, both techniques can be integrated in a single device. This SEM is capable of secondary electron detection and backscattered electron detection to characterize sample topography. Its sensitivity to chemical composition allows to observe contrast between the SiO_2 substrate and the Al thin film, producing a nanometer lateral resolution image of the nanostructure. Due to channeling effects, grains are also visualized.

3.2.3 Liège Collaboration: In-Situ Electromigration

Supplementary to the electromigration performed at the KU Leuven laboratories, in-situ electromigration was performed in Liège. The research group in Liège, led by Alejandro Silhanek, is in the possession of Raith Pioneer Two SEM [46], similar to the one located in Leuven NanoCentre. However, the SEM located in Liège is modified to electrically connect a sample in the imaging chamber to external sources and meters. This setup allows to perform electromigration and to simultaneously image the process, giving valuable information on the dynamics of the electromigration process.

Regarding the details of these measurements, they are very similar to the setup and procedures practiced at KU Leuven. Mounting procedures such as wirebonding and ESD precautions described in Section 3.3.1 differ in Liège only by the sample holder and the contact box used to safely connect equipment to the sensitive sample. The wirebonder used there is also similar as the one used in Leuven. Concerning the electromigration software and devices, it is exactly the same. The same software drives the same voltage source, voltage meter and current meter (Keithley 2612). The electromigration setup will be further elaborated in the following section.

3.3 Controlled Electromigration

Controlled electromigration is performed using specialized software, capable of decreasing the junction conductance and therefore the junction cross section in a gradual and controlled manner. This software, the sample mounting procedure and the layout of the measurement scheme are described in the following sections.

3.3.1 Mounting Sample

To connect the nanostructured thin films to voltage/current sources and meters, the sample is mounted on a sample holder and connected electrically with a techniques called wirebonding. Since the thin film constrictions are fabricated to be (gradually) broken down by current, these constrictions are extremely fragile to electrostatic discharge (ESD). Necessary precaution steps were taken to avoid uncontrolled electromigration (i.e. breaking) while handling the samples.

Wirebonding

Before the sample can be placed in a purged and cryogenic environment, the sample is mounted on the sample holder by means of silver paste. Figure 3.4 (a) shows the (purple) square silicon sample containing the Al structures. The silver paste applied between the sample and sample holder provides thermal contact between the two. The silver paste is also capable of maintaining its strength at low temperatures. The bonding pads of the nanopatterned Al thin film are also visible and can be seen in the figure as a grid of 5×5 crosses. The nanostructures itself are located at the center of each cross. The bonding pads of these nanostructures are then electrically connected to this sample holder, which can in turn be mounted on conductive pins inside the cryogenic environment. In Figure 3.4 (a), two structures are electrically connected to the sample holder by means of thin wires. For one of these two structures, the connected copper bonding pads on the sample holder are highlighted in red, the wires in green. Applying ultrasound wedge wirebonding, the nanostructured thin film samples were connected to external transport measurement equipment. The wirebonding process is presented in Figure 3.4 (b).

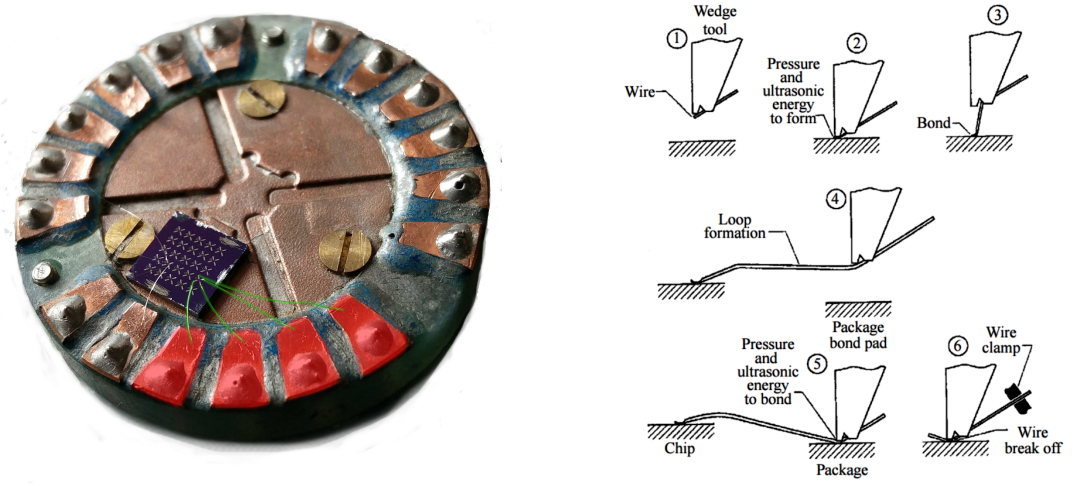

(a) ***(b)***

Fig. 3.4: (a) *Bonded sample mounted on sample holder* ***(b)*** *Main procedures of the ultrasound wedge bonding technique. Steps are further elaborated in the text. Figure (**b**) taken from [47].*

The first step in Figure 3.4 (b) illustrates the wire and the wedge bonding tool. Wedge bonding is performed using a wedge-shaped bonding tool. The wire is guided into the rear of the wedge at an angle of typically 30 to 60 degrees and fed to the foot of the wedge. Step 2 illustrates the first bond. With the wire located between bonding pad and wedge-foot, pressure and ultrasonic energy are applied to bond wire and pad. Step 3 illustrates the retraction of the wedge to a set height in order to move to a new bonding location. During this lift-off, the wire slides through the wedge's capillary holes. The next step illustrates the loop formation during re-locating to the next bond pad. This loop lifts the wire off of the sample surface and prevents direct electrical contact to unwanted area's. Step 5 and 6 illustrate the second bond making procedure. Pressure and ultrasonic energy is again applied while the wire is squeezed under the foot. During wedge lift-off however, a clamp through which the wire is fed into the wedge closes, immobilizing the wire. As the wedge retracts,

the connection between bond and wire is teared, leaving the bond in place. An electric connection between two pads has been made.

The employed wirebonder is the Kulicke and Soffa (K&S) Model 4526 Manual Wire Bonder [48]. It is a wedge bonder using ultrasound to weld a 25 µm diameter, 1% silicon-doped, aluminum wire between sample holder contacts and thin film bonding pads. Bonding parameters for each bond (1^{st} and 2^{nd}) such as vibration amplitude (power), pressure applied (force) an ultrasound duration (time) can be independently optimized to achieve the highest bonding strength.

ESD Precautions

The ubiquitous menace of electrostatic charge buildup and subsequent sudden release of this charge imposed a real threat to the vulnerable nanostructures. Electrostatic discharge could induce currents of high enough density to cause uncontrolled electromigration with dramatic consequences for the thin film constriction. The necessary precautions were made to avoid these scenarios.

These safety measures include shorting the sample holder connections to a common ground during bonding and grounding the experimentalist while handling the sample. During bonding, the sample is connected through a mega ohm resistor to the ground circuit of the wirebonder. The experimentalist is directly connected to the ground by means of a conducting wristband. The mega ohm resistor ensures that any potential difference occurring between ground and some contact on the sample, in spite of the precautions, will be removed slowly. After bonding, the sample is transported in a conductive box, shorting all the connections pins on the sample holder. When connecting the sample to measurement setup, the experimentalist is again connected to ground. Before electrical connection is made between any device and the sample, everything is connected to ground. Then, the ground contact is released, leaving the measurement devices connected to the sample. This procedure is based on the 'make-before-brake' principle. Furthermore, an ionizing fan blowing on the sample ensured that a potential difference between sample and other contacts is removed during sample transport disconnected from its shorting box. These precautions assured a high success rate of delivering a live sample into the measurement setup.

3.3.2 Layout of the Measuring Scheme

In order to measure the resistance of the nanoconstriction, a technique similar to the four point probe measuring scheme is employed. A current is applied through the constriction by means of a voltage source. By measuring the voltage drop on the constriction, the resistance of the constriction is calculated. This technique removes the dependence of the lead resistances on the constriction resistance measurements.

Figure 3.5 presents a false-colored SEM image of a typical nanoconstriction. A layer superpositioned on this image illustrates the equivalent schematic circuit of the nanostructure. Depicted in this schematic is a voltage source U_0 providing the current measured by I through the junction, wires and leads connected in series, indicated as R_j, R_W and R_L respectively. The smaller loop measures the voltage drop over the junction and wires. Since the voltage meter U has a very large internal resistance, no current is flowing through the voltage contacts and the resistance of the structure in between the voltage contacts can be calculated. The measured resistance of this structure is defined as r, equal to $R_W + R_j$.

In contrast to what is depicted in the schematic layer of Figure 3.5, wires and constriction are spatially

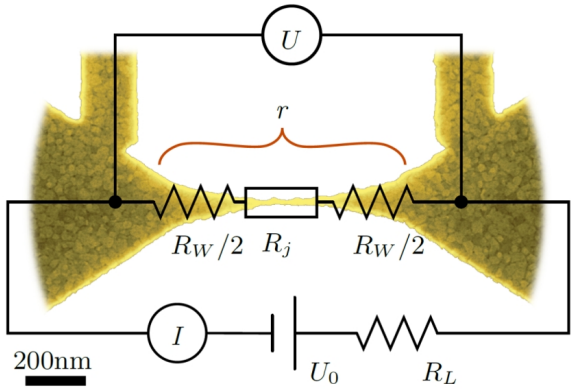

Fig. 3.5: *Equivalent schematic circuit superpositioned on a false-colored SEM image of a typical nanoconstriction. R_W denotes the wires resistance, R_j the junction resistance, R_L the leads resistance, I the measured current, U the measured voltage over the voltage probes and U_0 the applied voltage. Figure provided through the courtesy of my supervisor, Vyacheslav Zharinov.*

not exactly defined. The junction resistance R_j is located in the region where electromigration takes places. The parts of the conductor between the voltage probes which are not affected by the electromigration account for the wires resistance. The schematic layer over the SEM image is a simplification of the actual situation.

The resistance measurements provided the necessary feedback to control the increase of the junction resistance. The voltage source, voltage meter and current meter were all provided from a single device: Keithley 2612. These configurations can be independently chosen for 2 channels. The two loops in Figure 3.5 represent the two channels and are configured as depicted schematically: One channel measures the voltage drop U over the junction and wires, the other channel applies a voltage U_0 and measures current I.

3.3.3 Controlled Electromigration Software

The heart of the controlled electromigration procedure is the EM software, created by my daily supervisor, Vyacheslav Zharinov. The algorithm is written in Labview (Laboratory Virtual Instrument Engineering Workbench), capable of interfacing with devices such as the Keithley 2612 via a GPIB (General Purpose Interface Bus) connection.

Considering the discussion on electromigration in the theoretical introduction chapter, the rate of this process depends on temperature and current density. Simply applying a voltage or current over the junction will result in uncontrolled electromigration due to a positive feedback processes. At the onset of electromigration, lattice ions are removed from the constriction at the cathode side, decreasing the constriction cross section. This cross section decrease increases current density and local Joule heating, which in turn increases local temperature and accelerates the rate of electromigration and furthermore decreases cross section. An increase of current density also accelerates the rate of electromigration. This positive feedback is responsible for uncontrolled and an exponentially increasing rate of electromigration. This snowball effect is illustrated schematically in Figure 3.6. The above mentioned arguments indicate the need for an advanced control algorithm to gradually

reduce the constriction size using electromigration.

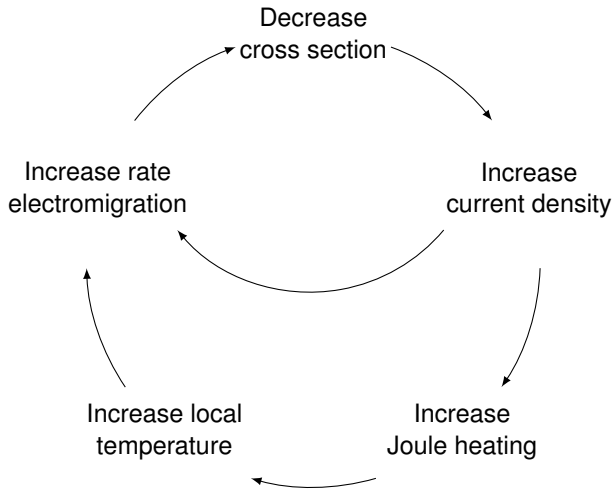

Fig. 3.6: *Snowball effect of uncontrolled electromigration.*

General Overview Software

The algorithm implemented here can be subdivided into two main parts. A widely used linear Proportional-Integral-Derivative (PID) control algorithm and a non-linear 'fast algorithm'. These two components try to maintain the decrease of the conductance to a predefined constant value ($dg/dt = \dot{g} = Constant$) with g defined as the conductance of junction and wires ($g := 1/r$). They provide controlled constriction breakdown by keeping this conductance decrease constant. This is achieved by controlling the applied voltage over the structure (depicted as U_0 in Figure 3.5). A general overview of the software is presented in Figure 3.7.

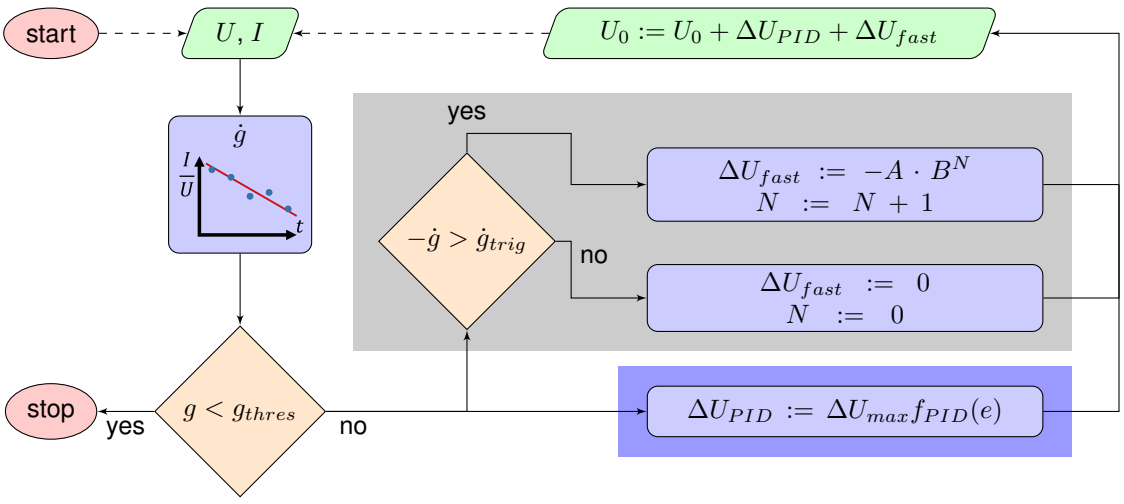

Fig. 3.7: *Flowchart controlled electromigration software.*

The PID algorithm is highlighted in the blue rectangle, the 'fast algorithm' in the gray rectangle. At the beginning of each iteration, the software calculates g and $\dot{g}$ from the measured U and I and checks if the conductance is below a given threshold g_{thres}, i.e. if the conductance goal is reached and the electromigration has finished. When the conductance goal is net yet reached, the PID controller calculates the necessary change in applied voltage to minimize the error $e(t)$ (equation (3.3). If triggered by a too fast decrease of conductance, the 'fast algorithm' acts to decrease the applied voltage exponentially. A corrected U_0 is applied to the structure and the cycle is repeated. Each iteration of the cycle requires approximately 50 ms.

General Proportional-Integral-Derivative (PID) control

PID control is by far the most common method of providing feedback regulated control in engineering systems [49]. In general, a system can be abstractly defined as a black box, with an input or actuation command u and an output y or process variable. Since the black box's response has unknown or complex behavior, the relation between input and output is not exactly known. This is where the PID controller comes in. It attempts to maintain the process variable (output) on a set reference value r by controlling the actuation (input) command. The error $e(t) := r - y$ is defined as the difference between process variable and reference value. The working principle of the PID controller is based on linear operations on this error. The sum of these linear operations is the actuation command presented in equation (3.2).

$$u(t) = k_p e(t) + \int_0^t e(\tau)d\tau + k_d \frac{de(t)}{dt} \tag{3.2}$$

The PID control action is located in the sum of three terms, which can be seen in equation (3.2): The proportional term, the integral term and the derivative term. Each term has its own proportionality constant, k_p, k_i, and k_d for the proportional, integral and derivative term respectively. A typical example used to describe the working principle of these three terms is temperature control. In this example, the black box is a room, which has a temperature and can be heated by a heating element. The output here is the temperature of the room and the actuation command is related to the power applied to the heating filament. The reference value is the temperature setpoint on the thermostat. The proportional term provides a feedback action depending on the instantaneous value of the error. The integral term produces a correction term by considering the error up to time t. In some cases, additional refinement is provided by implementing the derivative term. The error rate of change provides an error growth estimate, allowing feedback action based on an estimated future error.

Process Variable

The input of the algorithm is the process variable. Depending on its current value and history, the appropriate actions are taken. The measured conductance decrease, $\dot{g}(t) = d\left(\frac{I(t)}{U(t)}\right)/dt$, is called the process variable. The $\dot{g}$ is calculated as the linear fit slope of five consecutive measurements of g in time. The reference value is the setpoint decrease in conductivity $\dot{g}_{Setp}$. The PID control algorithm works to minimize the difference between process variable and reference value, defined as the error:

$$e(t) = \dot{g}_{Setp} - \dot{g}(t). \tag{3.3}$$

Linear PID Voltage Control

A PID algorithm is used to maintain $\dot{g}$ to a set value. The input of the PID controller is solely the error of the measured conductance decrease with respect to setpoint value (equation (3.3)) and the history of this error. The linear PID operations on this error are collected in the PID function f_{PID}:

$$f_{PID}(e) = \left(k_p \int_{t-\tau_p}^{t} \frac{e(t')}{\dot{g}_{Setp}} dt' + k_i \int_{t-\tau_i}^{t} \frac{e(t')}{\dot{g}_{Setp}} dt' + k_d \dot{e}(t) \right). \tag{3.4}$$

The working principle of the implemented PID algorithm here is described as follows: The change in voltage ΔU_{PID} is calculated for each iteration step (measuring change of conductance) and added to the previous applied voltage U_0. This change in voltage ΔU_{PID} is proportional to the actuation command f_{PID}. The proportionality constant is a parameter of the algorithm and is of the order of 10^{-4} V. The PID algorithm implemented here differs from the textbook example of PID control (3.2). In practice, noise hinders the measurements and thus reliable feedback control to the system. False signals such as noise entering the PID control input are interpreted as true signals and acted upon. Additional parameters are introduced to minimize the noise influence. Parameters τ_p and τ_i in equation 3.4 represent the time windows in which the proportional and integral terms are calculated. In the textbook PID algorithm, the proportional term is only dependent on the instantaneous error value. Due to measurement errors, some $e(t)$ history is also incorporated in the calculations of the proportional term. τ_p has a value of 2.5 s and τ_i 7.5 s.

Non-Linear Voltage Control

The second main component of the electromigration software is the 'fast algorithm', capable of exponentially decreasing the applied voltage. While the PID control is constantly regulating the applied voltage required to maintain a constant decrease of constriction conductance, the 'fast algorithm' lies dormant 99.9% of the time. Even though the PID does most of the work, the fast algorithm is essential to a controlled breakdown of the constriction. As described above, uncontrolled electromigration causes exponential decrease of conductance due to the positive feedback processes (Figure 3.6). The PID based on linear operations alone can not stop this exponential runaway situation.

The 'fast algorithm' is only activated when a certain condition is met. If the decrease in conductance exceeds a threshold value $\dot{g}_{trig}$, the 'fast algorithm' is triggered. Since the noise level of the measured conductance change in time, the threshold value is calculated on the fly using the root-mean-square (RMS) value of the previous 150 measurements of $\dot{g}$. Upon triggering, an additional change in voltage ΔU_{fast} next to the ΔU_{PID} is added to the currently applied U_0. Equation (3.5) presents this additional change in applied voltage upon triggering. Parameter A is on the order of 10^{-4} V, B represents a dimensionless parameter of value 2. N counts the number of consecutive times the 'fast algorithm' has been triggered.

$$\Delta U_{fast} = -A \cdot B^N \tag{3.5}$$

3.3.4 Physical Property Measurements System (PPMS)

The Quantum Design Model 6000 PPMS (Physical Property Measurement System) [50, 51] offers a tremendous flexibility to perform various kinds of measurements. Versatile sample mounts couple to the 12 electrical leads built into the cryostat insert. External instruments may be electrically connected to perform various types of measurements. Atmospheric conditions and temperature

can be regulated with this instrument. Operating temperatures range from 1.9 to 400 K, including a smooth temperature transitions when warming and cooling through 4.2 K. Magnetic fields up to 9 T can be applied. However, since the magnetic field is not used in the current work, it is not further elaborated here. The Physical Property Measuring System's main components and controllers are schematically illustrated in Figure 3.8. In the current work, this device is employed to electromigrate at low temperatures.

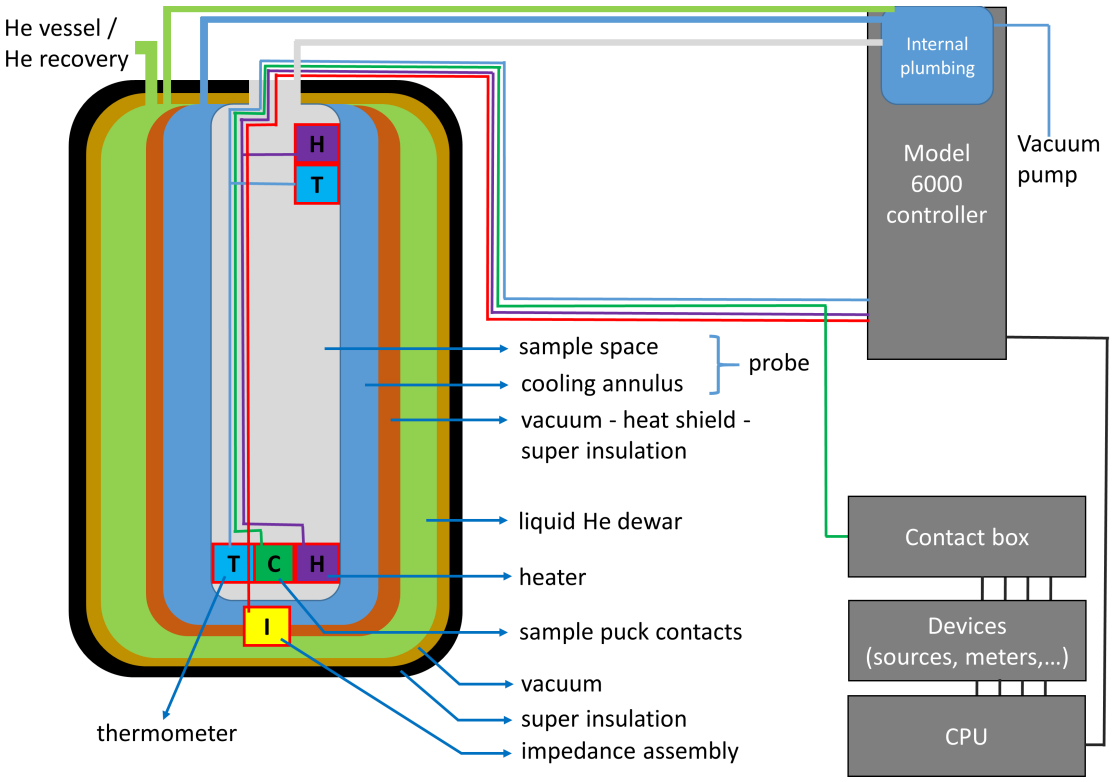

Fig. 3.8: *Schematic illustration of the PPMS setup. The left side of the figure presents the cryostat environment for the sample, the right side illustrates the controllers and sample contacts to devices such as sources and meters. Further details are elaborated in the text. Figure adapted from [52].*

PPMS Probe

The sample chamber together with the cooling annulus form the PPMS probe. The sample fitted on the sample puck is mounted on the 12 pin connectors on the bottom of the sample space. Heaters and temperature sensors are located below these puck contacts and at the top of the sample chamber. An impedance assembly controls the flow of He gas or liquid into the cooling annulus. The assembly consists of a narrow tube (the impedance), a heater that warms the impedance, and a thermometer that indicates when the impedance is warm. When the impedance is warm, a bubble forms inside the tube, blocking the flow of liquid helium. With the impedance heater turned off, the liquid helium cools the impedance tube and flows into the cooling annulus, where it either vaporizes or fills the annulus, depending on the pressure inside the annulus.

Atmospheric Control

Inside the cryostat's sample chamber, the pressure and gases can be regulated with the Model 6000 controller. In the standard operation configuration, the sample chamber is kept at a few tens Torr with gaseous helium vapor supplied by the dewar or the He recovery system of the physics department. The PPMS is thus capable of a purged He low pressure atmosphere, even with an empty dewar. A solid-state silicon pressure sensor located within the Model 6000 provides the sample chamber pressure readout.

Temperature Control

A vacuum and 'super insulation' material minimize thermal contact between the liquid He dewar and the outside world. Another vacuum, heat shield and 'super insulation' shield the PPMS probe, consisting of the sample chamber and cooling annulus, from the He dewar. At sample chamber temperatures above 4.2 K, heating elements and impedance regulated He gas flow from the dewar into the cooling annulus control the temperature of the sample chamber. For lower temperatures, the system fills the cooling annulus with a controlled amount of liquid helium and manipulates the boiling point of the liquid helium. In this regime, temperature is controlled by heaters in the probe and by valves regulating the annulus pressure in located in the Model 6000 controller. Using this technique, the system can maintain a temperature of 1.9 K for hours. Sample temperature is monitored by a platinum resistance thermometer and a negative temperature coefficient (NTC) thermometer, mounted directly beneath the sample puck. Temperatures ranging from 400 K to 80 K are read by the platinum thermometer. Lower temperatures are measured by the NTC thermometer. Another NTC thermometer is mounted at the top of the sample chamber to monitor temperature uniformity. The low pressure He vapor provides thermal contact between sample chamber wall and the sample itself.

Measurement Setup

The 12 pins on the bottom of the sample chamber are connected to the contact box. The contact box is fitted with resistances and ground switches for ESD protection, as discussed in section 3.3.1. The contact box connects to devices such as the Keithley 2612. This device in turn is controlled by the EM Software (Section 3.3.3) via GPIB. Constriction resistance measurements are discussed in section 3.3.2.

In the current work, the PPMS is used to perform and monitor the electromigration process. Since it is not capable of temperatures lower than the critical temperature for superconductivity of aluminum, the superconducting phase can not be reached in this instrument. This instrument is thus used only for electromigration. Superconductivity characterization is performed in a different cryostat (discussed in section 3.4.1), which is capable of cooling the aluminum below its critical temperature. However, since the PPMS does not require elaborate procedures to insert the sample compared to the Heliox, it is still a valuable instrument to perform low temperature electromigration.

3.4 Superconductivity

As discussed in the superconductivity section in the theoretical background chapter, the superconducting state only exists below a certain critical temperature, critical magnetic field and critical current. In

order to explore the superconducting critical surface in this 3D parameters space (temperature, current, magnetic field) of the aluminum nanostructure, advanced equipment is needed. This section describes the employed equipment to characterize the nanostructure's superconducting properties.

3.4.1 Heliox ^{3}He Cryostat

To provide temperatures lower than the critical temperature of aluminum, the Heliox ^{3}He cryostat [53, 54] is used. With a base temperature of 300 mK, it is well suited to bring the aluminum structures to the superconducting state. Furthermore, this cryostat is equipped with a superconducting coil to apply a magnetic field.

The ^{3}He cryostat consist of a Heliox ^{3}He refrigerator stick inserted in an Oxford Instruments ^{4}He dewar. This dewar is kept at atmospheric pressure and contains the superconducting magnetic coils to apply a magnetic field to the aluminum structures. The coils are capable of applying field up to 5 T, with a magnetic constant of 69 mT/A. The Keithley 2440 is used as a current source to push current through these coils. At the center of the ^{4}He dewar, the Heliox stick is inserted from the top. The Heliox refrigerator stick contains the valuable ^{3}He in a closed circuit. An overview of the Oxford Instruments ^{4}He dewar and the Heliox ^{3}He refrigerator stick is presented in Figure 3.9. The left side of the figure illustrates the Oxford Instruments ^{4}He dewar, inserted with the Heliox stick. The right side presents a more detailed illustration of the components inside the inner vacuum chamber (IVC).

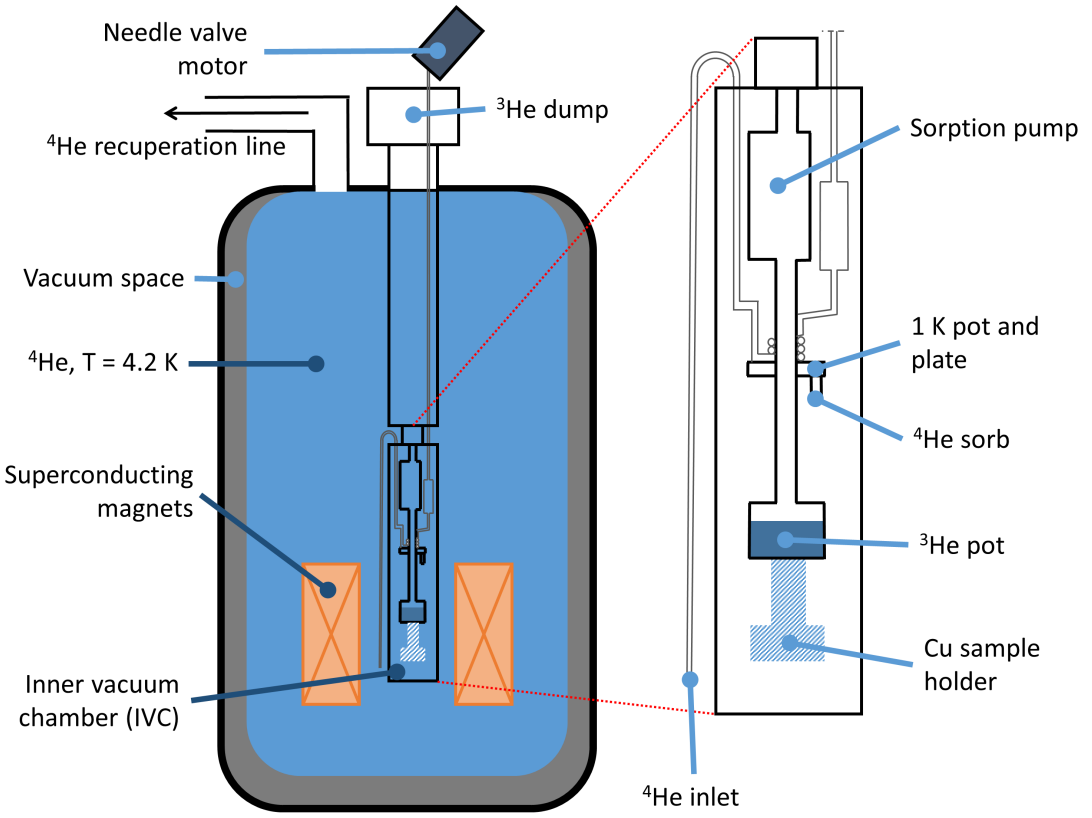

Fig. 3.9: *Schematic overview of the ^{4}He dewar with the Heliox ^{3}He stick inserted (left) and a zoom in on the inner vacuum chamber (IVC) (right).*

A schematic illustration of the Heliox refrigerator stick is presented in Figure 3.10. The sample is mounted below the ^{3}He pot. After mounting, the inner vacuum chamber (IVC) is pumped and filled with a small amount of exchange gas (^{4}He). During insertion of the stick into the ^{4}He dewar, this exchange gas cools the sample space. A gas sorb, mounted on the 1 K plate, is used to absorb the exchange gas from the IVC automatically during the cooling process. Once the IVC reaches a temperature of 4.2 K, ^{4}He is pumped by a rotation pump through the 1 K plate, with the needle valve slightly opened. This is the initiation of phase I of the cooling procedure. When the 1 K plate cools down to a temperature below 1.5 K, the sorb is warmed to 30 K by the sorb heater, releasing ^{3}He gas. The ^{3}He gas is now free to condense in the 1 K plate region of the central tube and collects at the bottom in the ^{3}He pot. After approximately 20 minutes, most of the gas has been condensed and the ^{3}He pot is nearly full of liquid ^{3}He at approximately 1.5 K. In phase II, the sorb heater turns off, the sorb cools down, starts to absorb ^{3}He and begins to reduce the vapor pressure above the liquid ^{3}He. Since the sorption pump is in thermal contact with the 1 K plate, it can be cooled to temperatures below 4.2 K. By cooling the sorption pump to below 3 K, the ^{3}He pot is pumped and the base temperature of 300 mK is reached. Intermediate temperatures between base temperature and 1.5 K can be set by changing the sorb temperature. Temperature stability of the Heliox cryostat is a few mK.

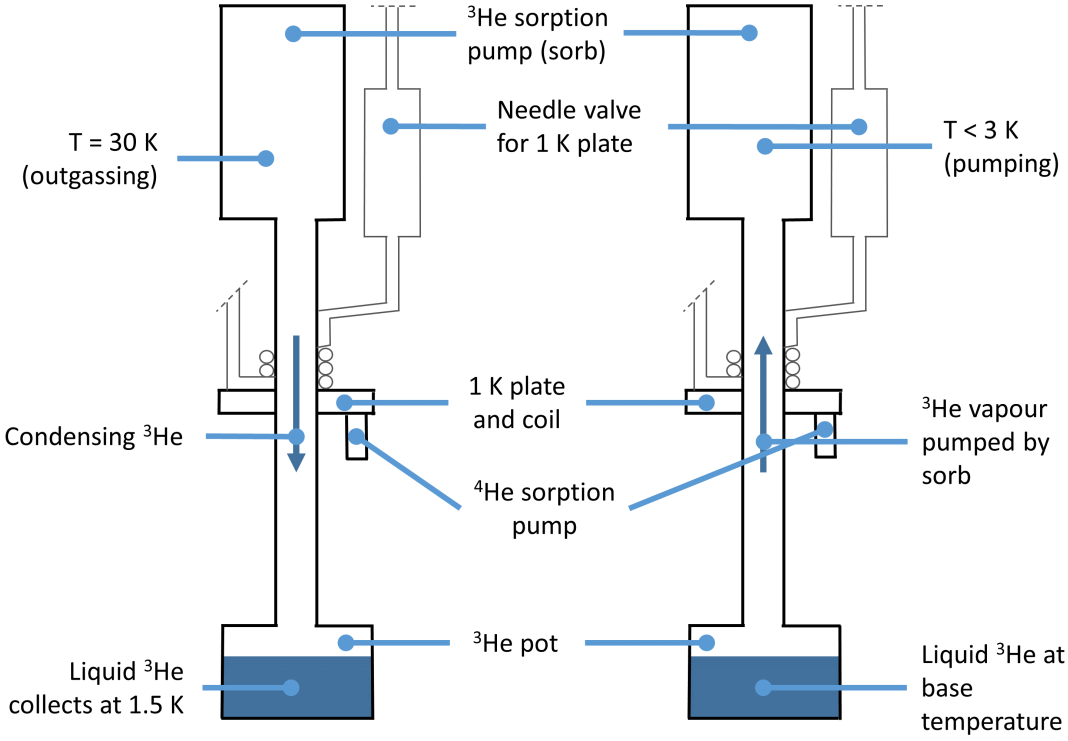

Fig. 3.10: *Schematic illustration of the operating principle of the Heliox cryogenic cycle. The left side presents the first phase of the cooling cycle, the right side the second phase.*

3.4.2 Electrical Measurements

Previous section described the environment in which the sample is residing, particularly the temperature and the applied magnetic field. This section discusses the methods and devices used to measure electrical quantities. Such quantities give information on the superconducting state of the nanostructure.

Common for all electrical measurements performed on superconducting devices is the high frequency filtering. Without this filtering, external (high frequency, gigahertz range) noise would enter the sample via the leads and excite quasiparticles, breaking up the Cooper pairs. This would prevent accurate measurements of the superconducting state. Special care has been taken to avoid the high frequency noise signal (above 1 MHz) using a capacitor-input filter or pi-filter.

Lock-In Amplifier

One of the devices used to measure these electrical quantities is a lock-in amplifier, more specifically, the Signal Recovery 7225 Dual Phase DSP Lock-in Amplifier. The use of these lock-in techniques are essential in order to measure weak signals compared to the noise. Since some of the electrical measurements on the superconducting devices requires a small probing current, the voltage drop measured over the structure is low compared to the background noise. This is where the lock-in

techniques are applied.

Lock-in amplifiers [55] are capable to detect and measure AC signals all the way down to the nanovolt regime. By making use of a technique called phase-sensitive detection (PSD) to single out a specific reference frequency and phase, accurate measurements can be made even when the noise obscures the signal by several orders of magnitude. Noise signals at frequencies different than that of the reference signal are filtered out and do not affect the measurement. This method makes the lock-in amplifier a powerful instrument in any lab.

The phase-sensitive detection technique excites an experiment at a fixed frequency, the lock-in detects the response of the experiment at the reference frequency. The signal exciting the experiment can either be generated by an external function generator or by the lock-in amplifier itself. Either way, the lock-in amplifier generates its own internal reference signal, which is phase-locked to the possible external function generator (using the sync output of the function generator for example). This internal reference has a sine waveform and can be written as $V_L sin(\omega_L t+\theta_{ref})$, where V_L is the reference signal amplitude, ω_L the reference frequency and θ_{ref} its phase. Suppose the response of the experiment is also a sine, written as $V_{sig} sin(\omega_r t + \theta_{sig})$, with V_{sig} the signal amplitude, ω_r the signal frequency and θ_{sig} the signal's phase. Next, the lock-in amplifier multiplies the signal with the lock-in reference. The output of the PSD is simply the product of the two sine waves:

$$\begin{aligned} V_{PSD} &= V_{sig} V_L sin(\omega_r t + \theta_{sig}) sin(\omega_L t + \theta_{ref}) \\ &= \frac{1}{2} V_{sig} V_L cos\left([\omega_r - \omega_L]\, t + \theta_{sig} - \theta_{ref}\right) \\ &\quad - \frac{1}{2} V_{sig} V_L cos\left([\omega_r + \omega_L]\, t + \theta_{sig} + \theta_{ref}\right). \end{aligned}$$

The output of the PSD is a superposition of two sine waves, one at frequency equal to the difference between reference and response $(\omega_r - \omega_L)$ and one equal to its sum $(\omega_r + \omega_L)$. This PSD output is passed through a low pass filter, removing the AC signals. However, if ω_L equals ω_r, the filtered PSD output will be:

$$V_{PSD} = \frac{1}{2} V_{sig} V_L cos\left(\theta_{sig} - \theta_{ref}\right),$$

which is a DC signal proportional to the signal voltage V_{sig}. However, it also depends on the phase difference between the signal and the reference $\theta = (\theta_{sig} - \theta_{ref})$. In order to eliminate this phase difference dependence, a second PSD can be added. If the second PSD multiplies the signal with a reference signal shifted 90° with respect to the first PSD, it's output will be

$$V_{PSD2} = \frac{1}{2} V_{sig} V_L sin\left(\theta_{sig} - \theta_{ref}\right).$$

There are two output PSD's: One is proportional to $sin(\theta)$ and the other to $cos(\theta)$. By defining the quantities X and Y from these PSD outputs as

$$X := V_{sig} cos(\theta), \qquad Y := V_{sig} sin(\theta),$$

the phase independent magnitude defined as $R = \sqrt{X^2 + Y^2}$ can be calculated. This magnitude is equal to V_{sig}.

The performance of the lock-in amplifier depends on the choice of the reference frequency and the parameters of the low pass filter. Suppose that instead of being a pure sine wave, the input is made up of signal plus noise. The PSD and the low pass filter are only sensitive to signals with frequencies close to the reference frequency. Noise components with frequencies vastly different from the reference frequency (neither $(\omega_{noise} - \omega_L)$ nor $(\omega_{noise} + \omega_L)$ produces a DC signal) are attenuated. However, noise components with frequencies close to the reference signal survive the low pass filter and are detected by the lock-in. The attenuation of these noise signals depends upon the low pass filter bandwidth and rolloff. Choosing the correct reference frequency, bandwidth and rolloff is key to the performance of the lock-in detector.

In traditional analog lock-ins, the signal and reference signals are analog voltage signals. The signal and reference are multiplied in an analog multiplier, and the result is filtered with one or more stages of RC filters. In a digital lock-in, such as the SR 7225 [56] employed here, the signals are represented by a sequence of numbers. Multiplication and filtering are performed by a digital signal processing (DSP) chip.

DC Sources and Meters

Besides the lock-in amplifier, DC instruments are also employed to characterize the superconducting phase. Typical measurements making use of DC instruments include the determination of the critical current. The selected devices are the Agilent 34420A Nanovoltmeter and the Keithley 6221 current source.

Chapter 4

Electromigration

This chapter discusses the results of the fabrication process and demonstrates the capabilities of the electromigration software. The design of the micro-SQUID is discussed first followed by the fabrication results, both presented in Section 4.1. Next, the electromigration software is demonstrated on the gold constrictions, given in Section 4.2. Also, in Section 4.3, bow-tie shaped, single, aluminum junctions are observed to reduce their cross section via electromigration. Lastly, in Section 4.4, the parallel weak links of the micro-SQUID are in-situ electromigrated and visualized using the SEM located in Liège.

4.1 Fabrication and Characterization

Before the results of the electromigration and the superconductivity measurements are presented (in this chapter and the next, respectively), the fabrication process of the three types of nanostructured thin films are discussed. These three types of structures consist of two aluminum structures and one gold structure. The gold structures were already available to use. The two aluminum structures, the SQUID and the single junction, are designed in the framework of this thesis. After fabrication, these structures were characterized by AFM and SEM.

4.1.1 Design SQUID and Junction

The first step to study the effects of electromigration on the SQUID properties is to design a SQUID structure compatible with controlled electromigration. Details of the design can be seen in Figure 4.1. The enclosed area at the center of the SQUID is $A = 0.34\ \mu\text{m}^2$. Considering that the magnetic flux quantum is of the order of 10^{-3} Tμm^2, the oscillation period in applied field is thus expected to be a few mT ($\Phi_0 = 2.07$ mTμm $= \boldsymbol{A}\Delta\boldsymbol{H}$).

The weak links of the SQUID are based on the 'bow-tie' design of Baumans et al. [38]. Simulations performed in this paper indicate a localized increase of temperature in the junction when a current is applied. This allowed them to decrease the junction cross section via electromigration. This junction design has proven itself to be a nucleation site for void formation. The difference with the aforementioned work is the parallel arrangement of two constrictions. Furthermore, current crowding effects are of no concern in [38], since there are no sharp angle bends in the current leads of the single junction geometry.

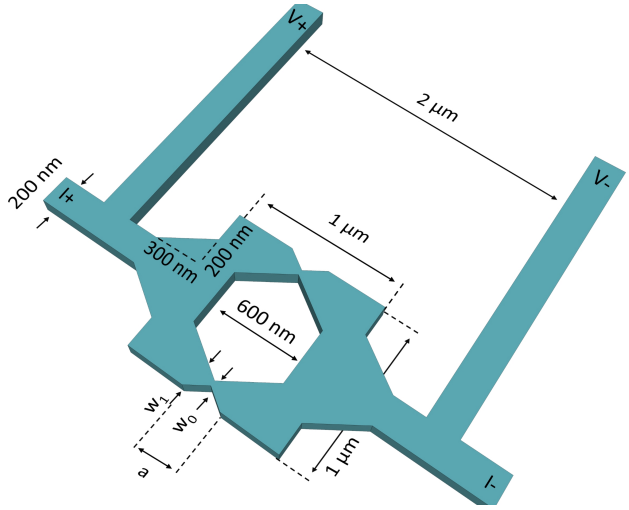

Fig. 4.1: *Details of the SQUID design. The bow-tie-shaped constriction has dimensions of* $a = 250$ *nm,* $w_1 = 200$ *nm and* $w_0 = 33$ *nm. The probing voltage leads, indicated as* $V+$ *and* $V-$*, and the current leads, indicated as* $I+$ *and* $I-$*, all have widths of* 200 *nm.*

The effect of current crowding in sharp angle bends has been taken into account when designing the micro-SQUID. Hagedorn *et al.* [57] reported an increase in current density up to a factor of 6 at the inner corner of a right-angle bend. Since the ratio of constriction width and width of the current leads is of the same order ($w_1/w_0 = 200/33$), the current density could become too high at locations other than the constriction. This leads to electromigration in undesired locations. Therefore, to avoid electromigration occurring in unwanted regions, sharp angle bends are not implemented in the design of the micro-SQUID. The final design is obtained from a combination of the bow-tie design and the considerations of the current crowding effect. The aluminum single junction structure is designed with the same parameters w_1, w_0 and a. The single junction design, used to characterize the properties of a single junction, is presented in Figure 4.2. Both designs allow four point probe measurements, with the leads indicated as $I+$, $I-$, $V+$ and $V-$.

4.1.2 Fabrication: EBL and MBE

The fabrication process starts in the cleanroom of Leuven NanoCentre. After cleaning the Si/SiO_2 substrates using acetone, rinsing it with isopropanol and drying using N_2, the e-beam resist layers are deposited via spin-coating. First, the copolymer PMMA-MA layer is spin coated at 4000 RPM. The PMMA-MA layer is baked for 2 min at $130°C$. Second, a PMMA layer is spin coated on top of the PMMA-MA at 7000 RPM. This second resist layer consists of longer polymers, counting approximately 950k monomers per polymer, almost a factor of 20 longer than the polymer length in the first resist layer. Finally, the second resist layer is again baked under the same conditions. The total thickness of the resist layers is approximately 300 nm. An AFM image of the mask and a line profile are presented in Figure 4.3.

The Si/SiO_2 substrate, covered with the resist bilayer, is placed into the vacuum chamber of the Raith eLine Plus by means of a load lock. Electrons are accelerated to 20 keV by the electron gun, focused into a beam of less than 2 nm in diameter and bombarded on the sample, changing the solubility of

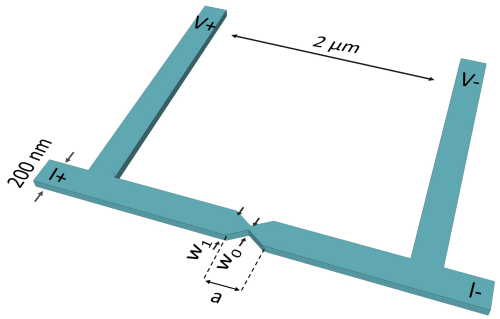

Fig. 4.2: *Details of the single junction design. The bow-tie-shaped constrictions have dimensions of* $a = 250$ *nm,* $w_1 = 200$ *nm and* $w_0 = 33$ *nm.*

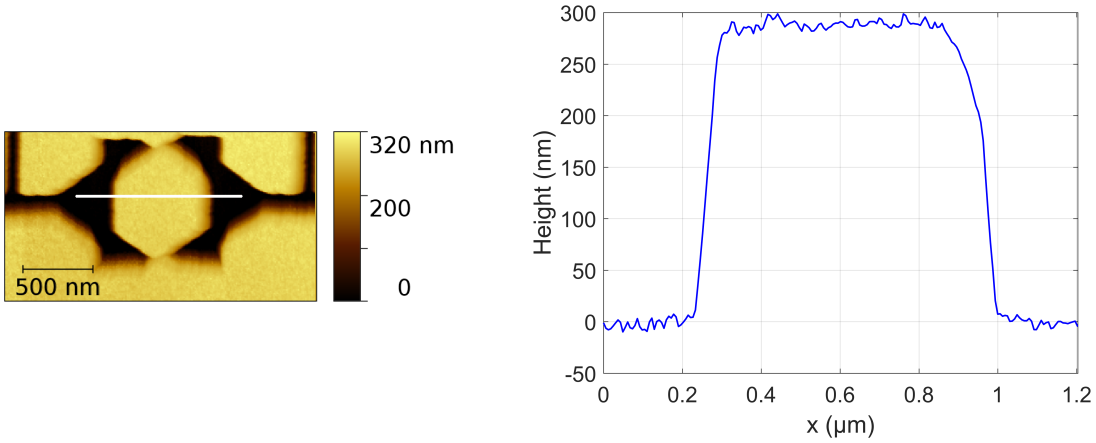

(a) ***(b)***

Fig. 4.3: ***(a)*** *AFM image of the mask after development.* ***(b)*** *Topography line profile of the white line in* ***(a)****.*

the resist layers in the developer. The beam current was 0.39 nA and the total dose applied to the exposed resist was 100 µC/cm^2. The sample is then developed for 10 seconds in a mixture of MIBK and IPA (1:1 ratio) to remove the exposed resist layers.

The following step is depositing aluminum on the mask. Considering similar electromigration and superconductivity measurements using micro and nanoscale structures, given in the paper of Baumans *et al.* [38] and in Moshchalkov's *et al.* paper [29], the desired thickness is 30 nm. The MBE-I located in KU Leuven's IMBL is used to deposit a thin film aluminum on the sample covered by the nanopatterned resist layers. The deposition rate is approximately 1 Å/s. The total deposition time is approximately 5 minutes.

4.1.3 Characterization: AFM and SEM

Atomic Force Microscopy

Figure 4.4 **(a)** presents an AFM image of the nanostructured thin film after the lift-off step presented in Figure 3.1 **(e)**. The lift-off step is performed in an ultrasound bath of acetone. The distinct geometry of the micro-SQUID in the AFM image can be readily seen. Lateral dimensions of the nanopatterned thin film will be further analyzed using SEM in the next section, for reasons mentioned in Section 3.2. Figure 4.4 **(b)** presents the height distribution of the SQUID structure calculated from the AFM image. The red dashed lines present Gaussian fits of the substrate and the thin film peaks. The thickness of the thin film is taken as the distance between these Gaussians and is (30 ± 2) nm. The error was calculated from the standard deviation of the substrate and Al peak. The standard deviation of the Al peak is 1.5 nm and provides information on the surface roughness of the Al thin film.

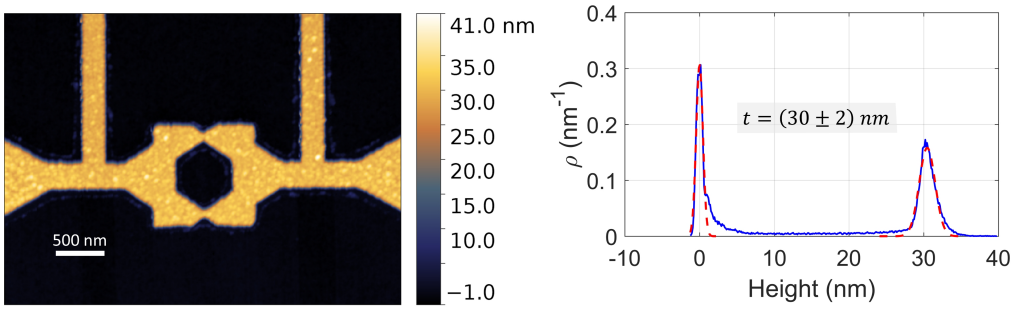

(a) ***(b)***

Fig. 4.4: ***(a)*** *AFM image of the thin film aluminum micro-SQUID.* ***(b)*** *AFM height distribution of the SQUID structure, where ρ represent a probability distribution.*

The thickness of single junction structure was determined in the same way. The value was found to be 30 ± 2 nm, similar to the value found for the SQUID structure, as is expected due to same batch in which these structures were made. The AFM image of the nanostructured single junction is presented in Figure 4.5 **(a)**. A height distribution is taken from a selection of data around the junction itself and plotted in Figure 4.5 **(b)**. The fitted Gaussian of the Al peak has a standard deviation of 1.6 nm. The parameters extracted from the single junction AFM scan (thickness, surface roughness) are similar to the parameters obtained from the SQUID structure AFM images (Figure 4.4).

Scanning Electron Microscopy

Figure 4.6 presents a SEM image of the aluminum thin film micro-SQUID. The distinct shape of the SQUID loop is readily visible. Analysis using ImageJ results in a hole area of 0.31 µm^2. Line profiles over the junctions result in junctions widths of 40 ± 10 nm. Voltage and current leads also show an approximate width of 200 ± 10 nm. The lateral dimensions obtained from SEM image analysis are in accordance with the design illustrated in Figure 4.1. A SEM image of the single junction structure is presented in Figure 4.7. The results of the AFM and SEM analysis present that 30 nm thick aluminum micro-SQUIDs and single junction structures have been fabricated successfully.

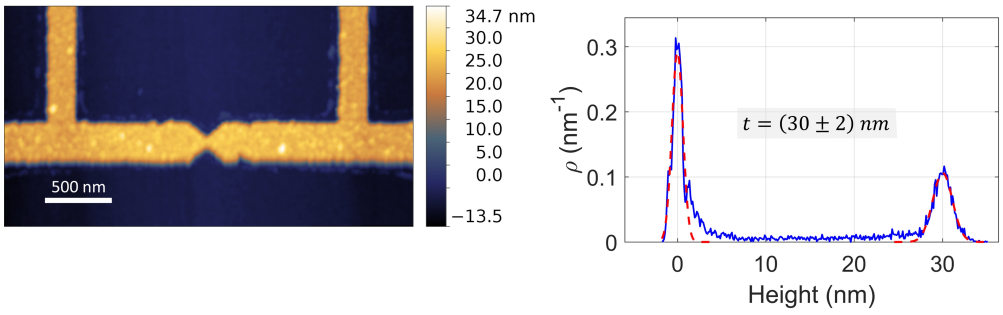

(a) ***(b)***

Fig. 4.5: ***(a)*** *AFM image of the nanostructured single junction.* ***(b)*** *Height distribution of the single junction AFM image obtained from AFM measurements.*

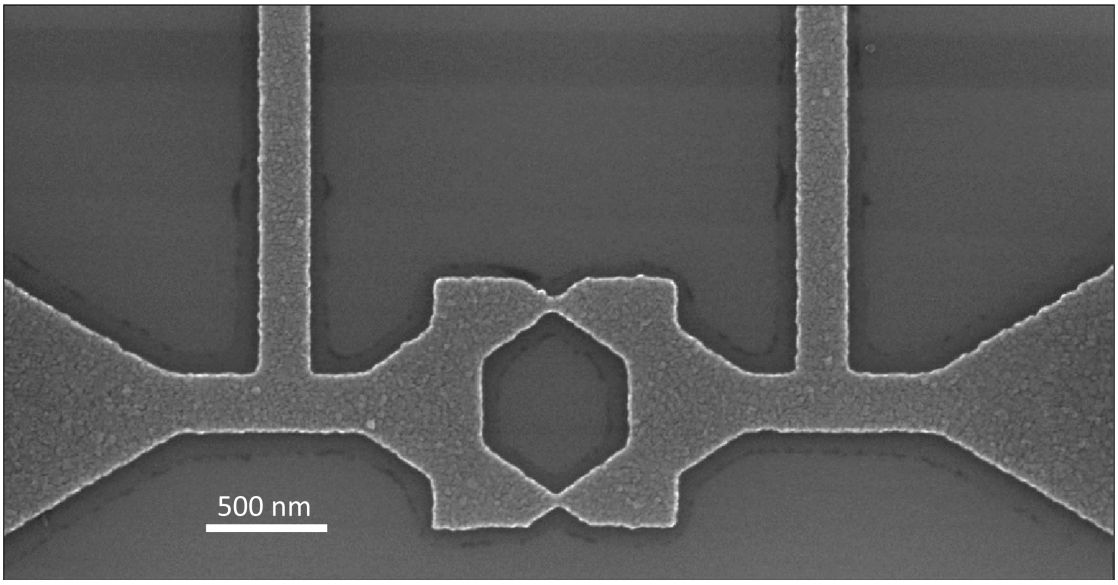

Fig. 4.6: *SEM image of the thin film aluminum micro-SQUID. The area of the hole is* $0.31\ \mu m^2$*. The junction widths are* 40 ± 10 *nm*

4.1.4 Gold Structure Geometry

The gold structures are not designed nor fabricated in the framework of this thesis. They are merely used to demonstrate the capabilities of the electromigration software. Furthermore, the sample containing the gold structure provided an abundance of junctions to train the experimentalist in using the electromigration software. A SEM image of the gold structure is presented in Figure 4.8. The current during the electromigration process flows from the bottom left electrode, makes a $\sim 300^\circ$ turn and exits the image via the left electrode (or vice versa). Note that this setup does not offer local voltage contacts enabling a four point contact measurement scheme. Some resist leftover due to an incomplete lift-off of the resist layers create the artifacts indicated in the figure. The gold structure thickness is 51 ± 2 nm, determined by AFM.

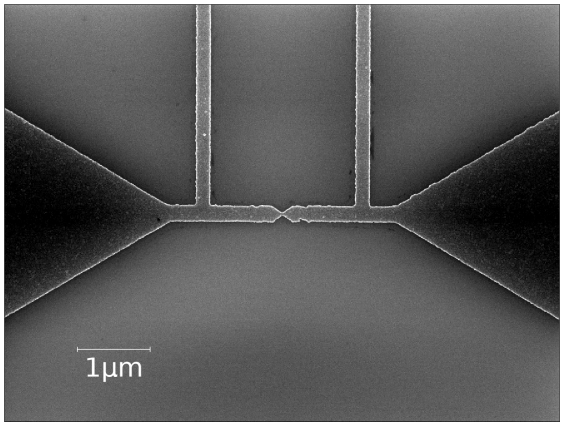

Fig. 4.7: *SEM image of the aluminum single junction structure. The junction has the same parameters as for the junction implemented in the SQUID.*

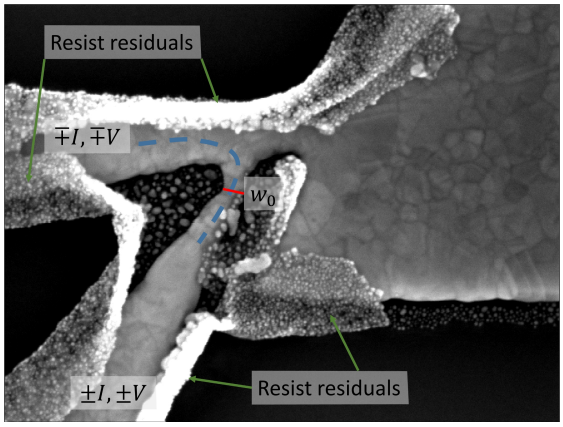

Fig. 4.8: *SEM Image of the gold structure. Thickness was found using AFM and is* 51 ± 2 *nm.* $V+$*,* $V-$*,* $I+$ *and* $I-$ *denote the voltage and current contacts. The width at the constriction is* $w_0 \approx 50$ *nm. The current path is indicated as the blue dashed line. The residuals of the resist layers are indicated by the green arrows.*

4.2 Electromigration of the Gold Structures

As mentioned above, the gold structures are used to demonstrate the power and flexibility of the electromigration software. One should view this section as a demonstration of the capabilities in employing electromigration as a 'tool' to reduce the junction cross section. Nevertheless, the physics of the electromigration process is not simply neglected. The electromigration results are analyzed and compared with the theory provided in Section 2.1. Performing electromigration on the aluminum SQUID samples requires delicate sample handling and software control compared with the gold structures. One slip-up in the electromigration process of the aluminum structures can mean several days of delay in the data acquisition due to the elaborate sample mounting procedure of the Heliox. Electromigration of the gold structures in low temperature achieved using the much more user-friendly PPMS allows for a steeper EM software learning curve. Furthermore, the number of SQUID

structures available is much smaller than the number of gold structures. The gold structures were fabricated with EBL techniques at imec and MBE using gold effusion cells described in Sections 3.1.1 and 3.1.2. Electromigration of the gold structures was performed at low temperature and in purged atmosphere as discussed in Section 3.3.4.

The conductance in time measured during the electromigration process of a gold structure is presented in Figure 4.9 **(a)**. The measured conductance is normalized to the quantum of conductance ($G_0 = \frac{2e^2}{h}$. The decrease in conductance setpoint, $\dot{g}_{Setp}$, is -0.1 G_0/s. From this plot it can be seen that the software does an excellent job in keeping the decrease of conductance constant. Figure 4.9 **(b)** presents the characteristic current as a function of voltage during the electromigration process.

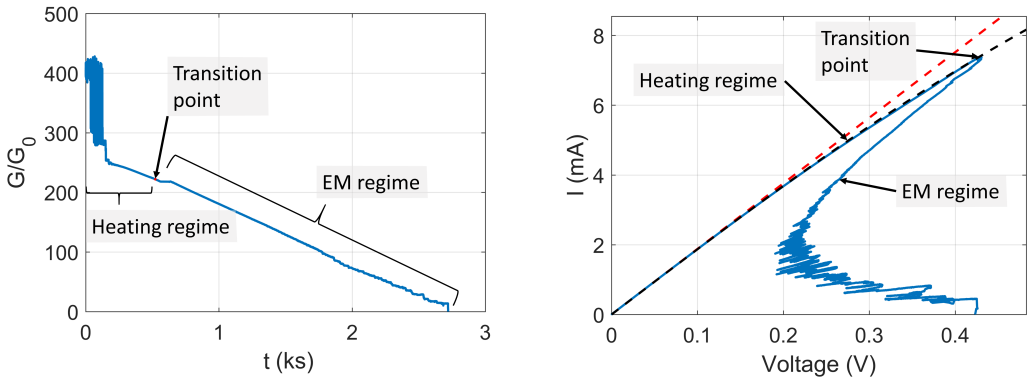

(a) ***(b)***

Fig. 4.9: ***(a)*** *Conductance as a function of time from start to end of the electromigration process. The measured conductance containing high levels of noise at the start of the electromigration is an artifact of the EM software.* ***(b)*** *Characteristic I(V) curve measured during the same electromigration process. The dashed red curve is plotted as $I = V/R_0$, with R_0 measured using a low probing current. The dashed black curve represents $I = V/R(I)$, with $R(I)$ calculated from the heating model given in equation (2.7) and fitted with the data using $(\alpha' R_\theta)$ as parameter.*

In both figures, two regimes are indicated: The heating regime and the electromigration regime. The physical origin of the measured decrease in conductance determines the separation of these regimes. When the software is started, it starts from a low applied voltage, and thus current. Next, it starts to ramp op the voltage to fix the decrease in conductance to a pre-set value (the $\dot{g}_{Setp}$ discussed in Section 3.3.3). During this initial ramp-up, the decrease in conductance is explained by an increase of junction temperature due to Joule heating. Since the current density in the junction is substantially higher compared with the surrounding electrodes, the increase in temperature is maximum in the narrowest region. Simulations performed in [38] present this localized increase in temperature. At a certain current, the temperature and current density are high enough to move atoms from the constriction elsewhere. This is the starting point of the electromigration region. The distinction between the different regimes is readily visible in Figure 4.9 **(b)**.

4.2.1 Heating Regime

Two arguments confirm that the measured data in the heating regime are indeed a result of the increase in temperature of the junction. The first and foremost argument is the fact that in this regime, the process is reversible. A second argument is the fact that the measured resistance fits the simple heating model provided by equation (2.7). The reversibility and fit with heating model is presented in Figure 4.10.

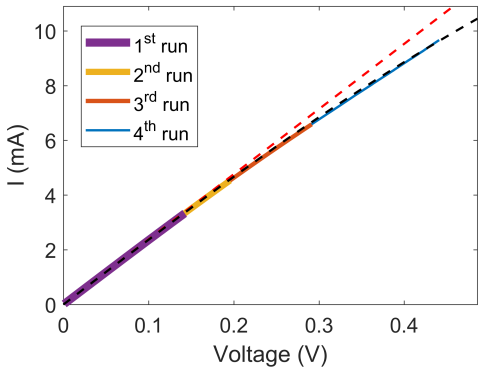

Fig. 4.10: *A few runs of ramping up the voltage in the heating regime. During each run the voltage is ramped up from zero to a maximum voltage, after which the voltage was set back to zero. The experimental data fit the simple heating model presented in equation (2.7). The black dashed line presents this heating model. The red dashed line assumes a constant resistance value.*

4.2.2 Electromigration Regime

In contrast with the heating regime, the electromigration regime is not reversible. Since this process induces a gradual displacement of atoms, the geometry is permanently altered. The resistance of an altered geometry is expected to be different. The voltage and current measured during the electromigration process provide information on the junction geometry. Since the measured resistance of the structure is not deterministic for a specific structure geometry, the exact geometry can not be found from resistance measurements alone (consider the integral to calculate the resistance from geometry given in equation (B.1)). However, it is plausible to assume that the width of the junction is reduced when the resistance increases due to the local action of electromigration.

The onset of electromigration is determined by a critical current density. This critical current density can be found from Figure 4.9 **(b)**. At the transition from the heating regime to the electromigration regime, the maximum (critical) current is reached. At the transition point between the two regimes regimes, the geometry has not yet been altered. This means that the critical current density can be calculated from this maximum current and the fabricated geometry of the junction. The critical current can be read from Figure 4.9 **(b)** and is $J^* = \frac{I^*}{S} \approx \frac{7.4}{51\times50}$ mA/nm$^2 \approx 3 \cdot 10^8$ A/cm^2, which corresponds to the value found in literature ([58], [59] and [60]). Due to variations in sample geometry and the ordering of grain boundaries in the junction (which provide the migration 'highways'), the measured critical current varies.

Once the electromigration regime is reached, the $I(V)$ curve is non-reversible due to the reduction of the junction's cross section. This non-reversibility in the electromigration regime is presented in Figure 4.11. This figure presents $I(V)$ curves measured during two electromigration runs performed on the same structure. For both runs, the two regimes (heating and electromigration regimes) are readily visible.

During the first run, the electromigration process was manually stopped at a measured conductance of the structure of about 50 G_0. After some time, the software was re-initiated. At the start of this second run, the heating regime occurs first while the current is ramped up. When the current and voltage reach the value at which the previous run was halted, the electromigration regime is again initiated and a gradual displacement of atoms occurs. This figure illustrates the 'Pause and Play' capability of the electromigration software, which will be extensively used in the next chapter. Another powerful capability of the software is that it can create junctions towards the quantum conductance limit.

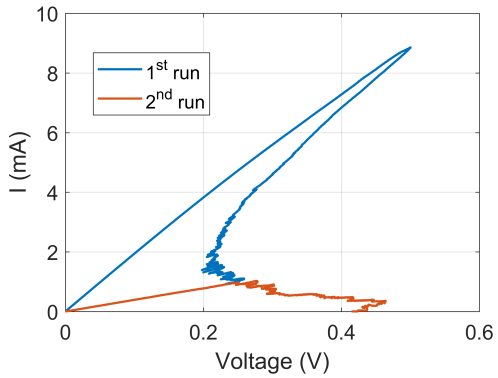

Fig. 4.11: *I(V) curves of two electromigration runs. The software was halted at a measured structure conductance of 50 G_0. At a later time, the software is restarted and the curve continues at the same point it was halted in the previous run.*

4.3 Electromigration of the Aluminum Single Junction

This section briefly presents experimental verification of reducing the bow-tie junction cross section via electromigration. A SEM micrograph of an electromigrated single junction is presented in Figure 4.12. Keeping in mind the goal of this thesis, this localization of the void formation in the constriction looks promising in terms of reduction of the weak link cross section. The $I(V)$ curve measured during the electromigration of these single junction aluminum structures is similar to the $I(V)$ curves measured during the electromigration of the gold structures, presented in Figure 4.11. However, the curve does not look as smooth for the aluminum structure.

4.4 Parallel Aluminum Junctions In-Situ SEM

In-Situ electromigration is performed on the SQUID structure using the SEM located in Liège ULg, discussed in Section 4.4. During the electromigration performed on the previously discussed samples, the only information on the junction geometry was provided by the current and voltage measurements.

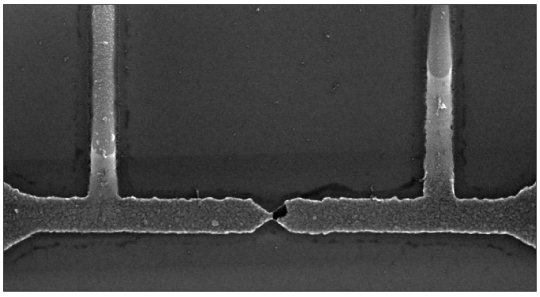

Fig. 4.12: *SEM image of a single junction aluminum structure after electromigration. The void formation is localized in the junction.*

Hitherto, this was our only 'window' to detect the structural changes of the junction during the electromigration process. However, with In-Situ EM performed in the imaging chamber of a SEM, the structural changes during the EM process can be obtained using high resolution images. Furthermore, the in-situ electromigration experiment serves as a crucial test to check if it is even possible to migrate two junctions in parallel using this SQUID design. Only then, after this check, is it possible to proceed and characterize the SQUID's superconducting properties. The in-situ electromigration SEM images of the two junctions in parallel are presented in Figure 4.13.

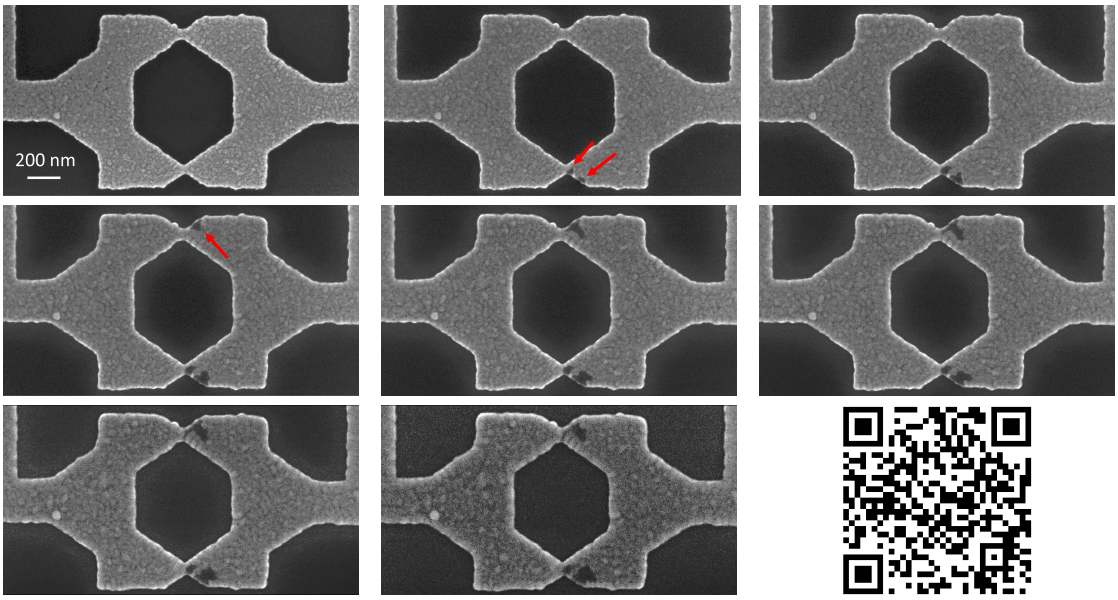

Fig. 4.13: *In-Situ electromigration imaged using the SEM located in Liège. The images are displayed chronologically from top left to bottom right. Void formation due to electromigration is observed in both junctions. The deterioration of the image quality over time is due to carbon contamination on the surface of the sample [61]. The QR-code contains a YouTube link presenting a video of the In-Situ electromigration experiment discussed here.*

The conductance in time during the electromigration process is presented in Figure 4.14 **(a)**, the I(V) curve is shown in 4.14 **(b)**. The times at which the SEM images, presented in Figure 4.13, were

taken are indicated as the colored dots in Figure 4.14.

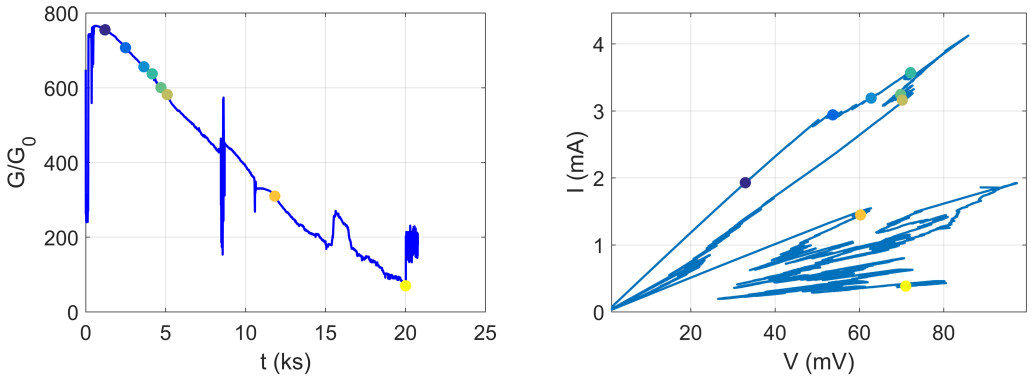

Fig. 4.14: ***(a)*** *Conductance as a function of time.* ***(b)*** *I(V) curve. In both figures, the times at which an image was taken is indicated as a colored dot.*

Compared with the gold structures, the $I(V)$ curve measured during the in-situ EM process does not look as smooth as the $I(V)$ measured for gold, presented in Figure 4.9 **(b)**. Reasons for this discrepancy are due to the difference in material. Material transport in Al is mostly along grain boundaries, due to immobilized atoms at the surface due to oxidation. Therefore, in Al, these grain boundaries introduce a more stochastic removal of material. This is not the case for gold. Furthermore, most likely due to the parallel arrangement, the start of electromigration is not characterized by the maximum current in the $I(V)$ curve. The electromigration regime starts when the initial voltage ramp-up does not follow the heating model, roughly just before the second image was taken. The first image does not show any sign of 'damage' and follows the heating model. Void formation can be seen in the lower junction in the second image. Also in the third image, the void is seen to grow. In the fourth image, the upper junction also starts to show void formation. Only when the upper junction also shows signs of electromigration, the maximum current or 'transition point' is reached. Hereafter, both junctions are seen to decrease their cross section.

During the parallel junction electromigration process presented here, one of the bonds connected to the current leads suddenly broke at $t \approx 20$ ks. The conductance value measured after this time, presented in Figure 4.14 **(a)**, is a false signal showing high levels of noise. However, this in-situ electromigration still presents a working tool to reduce the weak link cross section to a parallel conductance of less than 100 G_0.

This section presented experimental verification for parallel EM. It was observed that for the SQUID structures, designed in the framework of this thesis, the weak links could be gradually reduced in cross section via electromigration. Therefore, the investigation is proceeded to the next step in this thesis: Investigating the superconducting properties of the micro-SQUID.

Chapter 5

SQUID

This chapter deals with the low temperature measurements. First, the superconducting parameters of thin film aluminum are quantified from experiment in Section 5.1. Second, the superconducting properties of the 'as fabricated' or virgin SQUID are characterized in Section 5.2. Finally, the superconducting properties of the SQUID are determined after each electromigration step in Section 5.3.

5.1 Superconducting Parameters

Before the electromigration process is used to modify the weak links in a controllable manner, the virgin SQUID's superconducting parameters are characterized. Parameters such as critical temperature, resistivity and scattering length are extracted from the low temperature measurements of the SQUID and single junction structure. From the single junction measurements the coherence length is obtained.

5.1.1 Resistivity

The first electrical measurements performed on the SQUID determine its resistance as a function of temperature. Mounting the sample into the Heliox cryostat and taking into account the ESD precaution protocols, the voltage across the structure is measured with the lock-in amplifier (SR 7225) with a constant current of 100 nA applied. From these $R(T)$ measurements, the resistivity at low temperatures (but above the critical temperature) of the aluminum structures can be found. The resistance of a conductor with a spatially constant thickness and resistivity is calculated using the following formula:

$$R = \frac{\rho}{t} \int \frac{dx}{w(x)}, \tag{5.1}$$

where ρ is the thin film aluminum resistance, $w(x)$ the width of the strip at x, t the film thickness and x a dummy variable running over the structure in the direction of the current flow between the voltage contacts. Since the geometry of the structures is known, the integral in equation 5.1 has a numerical solution and is only dependent on the geometry. The value of this integral is worked out in Appendix B. The normal resistance, R_N, is calculated form the average of the resistance measured between 1.5 K and 1.6 K. Note that this is an arbitrary choice, but it will be upheld consistently throughout this chapter to define the resistance of the structure.

SQUID

A resistance value of $R_N = (7.99 \pm 0.05)\ \Omega$ is found for the SQUID structure. The error is calculated as the standard deviation on the mean while taking into account the accuracy of the lock-in. Consulting the value calculated in the appendix and the thickness found from AFM measurements, the resistivity is $\rho = 3.9 \pm 0.3$ µΩcm for the SQUID structure.

Single Junction

Using the same procedures, the resistivity of the thin film is also found from the single junction resistance measurement. The resistance of the single junction structure is $13.10 \pm 0.07\ \Omega$. Using similar calculations as presented in Appendix B, a resistance of $R_N = 11.43\rho/t$ is found for the single junction structures. The resulting resistivity measured for the single junction structure is 3.4 ± 0.2 µΩcm. The resistivity values measured for both structures correspond within their margin of error. The values are comparable to the ones found in literature [62], [28].

5.1.2 Critical Temperature

Critical temperature measurements, or $R(T)$ measurements, are performed on both the single junction and the SQUID structure. The SQUID measurement is discussed first.

SQUID

The resistance as a function of temperature, $R(T)$, of the virgin SQUID are presented in Figure 5.1

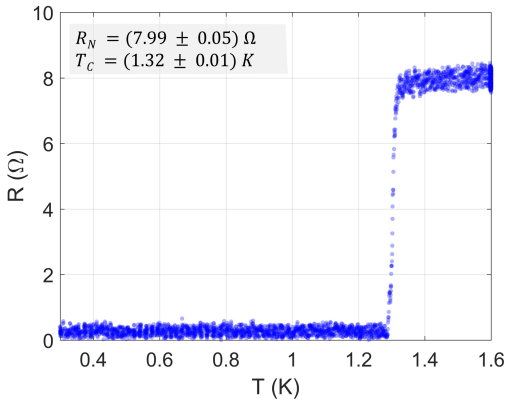

Fig. 5.1: *Resistance as a function of temperature of the virgin SQUID.*

The critical temperature of the SQUID structure is $T_c = 1.32 \pm 0.01$ K, determined by a 'superconducting resistance criterion' of $R < 0.9R_N$.

Single Junction

The same characterization procedure to determine the critical temperature is repeated for the single structure. The $R(T)$ measurement performed on the single junction is presented in Figure 5.2. The value for the normal resistance and critical temperature of the single junction, presented in Figure

5.2, are obtained from the 100 nA measurement.

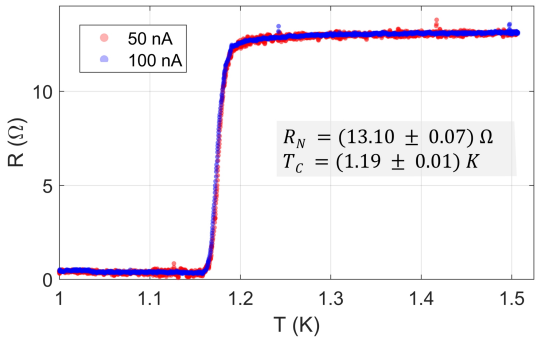

Fig. 5.2: *Resistance as a function of temperature of the single junction structure.*

To check if the applied current, 100 nA, is low enough to not disturb the critical temperature measurement, a $R(T)$ curve is measured at a lower applied current. The $R(T)$ measurement at a lower applied current, which is 50 nA, is also depicted in Figure 5.2. This measurements performed at lower current yields a normal resistance value of $13.07 \pm 0.07\ \Omega$ and the same value for T_c as the measurement at 100 nA. The only difference between the two measurements at different current is the increase in noise in the 50 nA measurement. The correspondence in measured R_N and T_c between the 100 nA and the 50 nA performed on the single junction structure indicates that the choice of current at 100 nA is low enough to not disturb the superconducting condensate while still large enough to have a strong signal with respect to the noise. The critical temperature of the single junction is 1.19 ± 0.01 K with a superconducting criterion of $R < 0.9R_N$.

Strikingly, T_c varies significantly between the critical temperature measurement performed on the SQUID structure and the single junction. Since both structures are located on the same sample, the fabrication process is identical to both. Therefore, the critical temperature is expected to be the same. This is not the case. Reasons for this discrepancy are not quite clear, especially since the resistivity is similar to both structures. One explanation attributes this difference to a possible difference in grain sizes of the structures. However, this was not investigated thoroughly.

5.1.3 Coherence Length

Coherence Length from Tinkham Formula

The coherence length of the thin film is found using the single junction structures. The choice to determine the coherence length using these single junction structures is due to the fact that the width of these structures is spatially constant (except in the junction itself), allowing us to apply the Tinkham formula (2.42). Since these structures consist of two rather long wires of width w_1 compared to the junction itself, the superconducting criterion of $R < 0.9R_N$ probes the transition when these wires become normal conducting at a certain temperature and applied field. Therefore, w is taken as w_1 in the Tinkham formula, given in equation (2.42).

From Figure 4.7 and similar SEM micrographs, the width of the thin strip is determined to be $(20 \pm 1) \cdot 10$ nm. The error is determined visually by considering the non-uniformity of the width of the thin strip

between the junction and the voltage contacts. Resistance measurements as a function of applied field and temperature were performed ($R(H,T)$). The experimental data are obtained by scanning over the applied magnetic field at a certain temperature. The steps in field are 0.2 mT and the stepsize in temperature is 2.5 mK.

A selection of these measurements are illustrated in Figure 5.3. These $R(H,T)$ measurements produce the $T_c(H_c)$ data presented in Figure 5.4 **(a)**, determined by the contour line at the same superconducting criterion as was used before ($R < 0.9R_N$). The measured phase boundary between the normal and superconducting state is presented in blue, the fit with the Tinkham formula is indicated by the dashed red line.

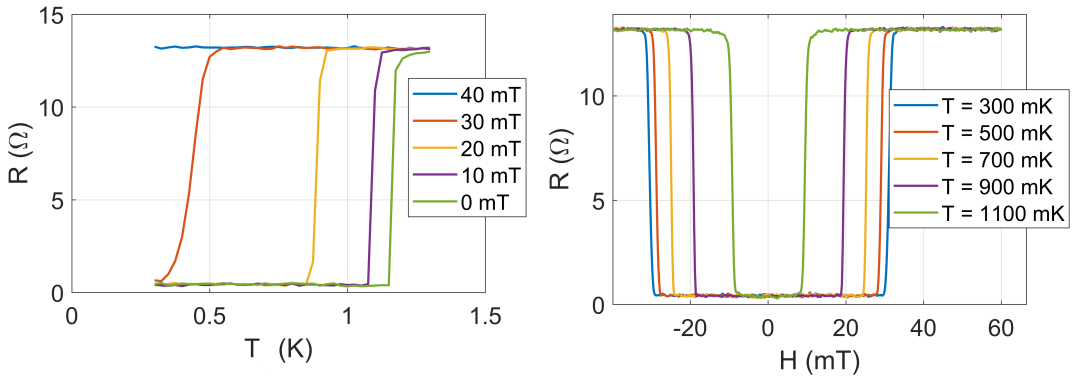

Fig. 5.3: ***(a)*** *Resistance of the single junction structure as a function of temperature for different applied field values.* ***(b)*** *Resistance of the single junction structure as a function of the applied magnetic field for different temperatures.*

The fit is taken of the form $f(H) = t_c\left[1 - c^2(\mu_0 H)^2\right]$, according to Tinkham's formula (2.42), with t_c and c the parameters of the fit, where t_c is the critical current at zero field. From the fitted value of c, the coherence length can be determined. Since the data do not exactly match the parabolic shape of the fit, a second fit attempt is made by only fitting the data at a temperature above 0.8 K. Only then is the condition set by the Tinkham formula valid, which is that the width of the strip must be smaller than the coherence length. At 0.8 K and higher temperature, the coherence length is at least 250 nm, making the use of the Tinkham formula justified. This second fit attempt is presented in Figure 5.4 **(b)**. Using the fit values for the second attempt and an error of ± 2 on the c parameter, a value for the coherence length $\xi(0) = (14 \pm 1) \cdot 10$ nm is obtained. This value is substantially smaller than the BCS coherence length ($\xi_0 \approx 1600$ nm [63]), thus indicating that the nanostructured superconductor falls in the dirty limit. The value found for the coherence length corresponds to literature [38], [28].

Coherence Length from Scattering Length

An alternative approach to determine the coherence length, besides the Tinkham formula, is by using equation (2.36b), which describes the coherence length for a superconductor in the dirty limit. To confirm that our nanostructured superconductor falls in the dirty limit, one needs to calculate the electron scattering length or mean free path length and compare this to the BCS coherence length. Using the relation $\rho l = 4 \cdot 10^{-6}$ μΩcm^2, valid for aluminum thin films [62], the mean free path length

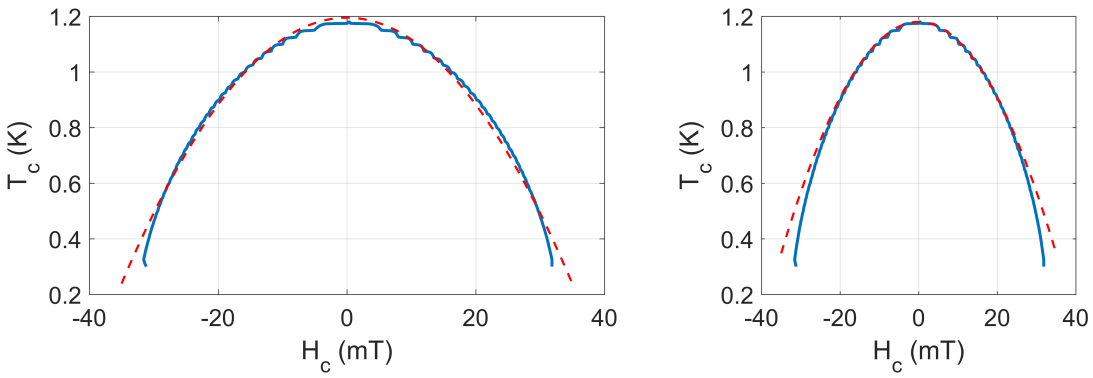

Fig. 5.4: ***(a)*** *Single junction critical temperature as a function of critical applied field (blue curve). The red curve represents the fit with Tinkham's formula (2.42). The fitted values are* $t_c = 1.20$ *and* $c = 25.5$. ***(b)*** *Second fit attempt with high temperature data (above* 0.8 *K). The fitted values are* $t_c = 1.18$ *and* $c = 24.0$. *Both plots are calculated as the* $0.9R_N$ *contour line from the* $R(H,T)$ *measurements presented in Figure 5.3.*

is found to be $l = 10 \pm 1$ nm, using the resistivity found in the SQUID structure. Using the resistivity found in the single junction geometry, the mean free path is found to be $l = 12 \pm 1$ nm. Recalling equation (2.36b) and evaluating at $T = 0$, one finds that $\xi(0) = 0.855(\xi_0 l)^{1/2} = (10 \pm 1) \cdot 10$ nm resulting from the SQUID structure measurements. $\xi(0) = (12 \pm 1) \cdot 10$ nm is found from the single junction measurements.

It should be pointed out that, for polycrystalline samples, the reported values of ρl, from which the scattering length is calculated, differ up to a factor of 4 [64]. The estimated values of the mean free path length are thus not accurate, but provide merely an order of magnitude. The coherence length calculated from the scattering length is indeed in the same order of magnitude as calculated in the previous section using the Tinkham formula. A final remark is made regarding the value of the scattering length. This corresponds to the grain size found from the SEM micrographs, in the sense that the scattering length is comparable, but smaller, to the grain size.

5.2 Virgin SQUID Characterization

5.2.1 $T_c(H)$ Oscillations

Figure 5.5 presents the superconducting $T(H)$ phase boundary of the SQUID structure, calculated from measurements scanning over the magnetic field at a certain temperature, similar to the procedure applied in Section 5.1.3. The step size in field is 0.1 mT. 2 mK is the step size in temperature. The oscillations visible in this figure marks the first manifestation of a macroscopic quantum phenomenon in this thesis. Its origin can be explained using the quantization of the fluxoid, presented in Section 2.2.4.

The physics governing this periodic critical temperature shift originates from the fluxoid quantization.

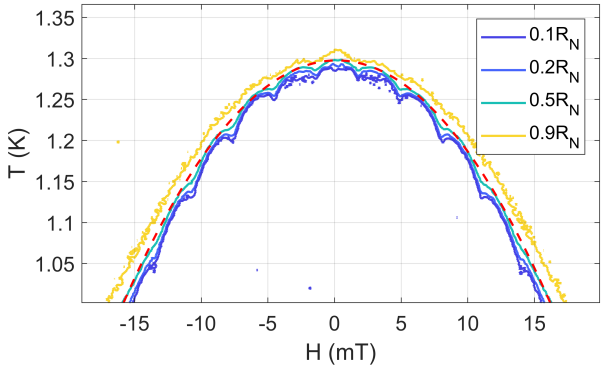

Fig. 5.5: *Resistance as a function of temperature and applied field of the virgin SQUID. The curves indicated in the legend represent the contour lines at various superconducting criteria. The dashed red curve is the fitted envelope of Tinkham's formula* (2.42)*. The applied current is* 100 *nA.*

The fluxoid quantization, discussed in Section 2.2.4, gives rise to circulating currents in the superconducting ring. Figure 5.6 presents the Cooper pair velocity, v_s, and kinetic energy, v_s^2, as a function of the flux enclosed in a superconducting ring. According to the free energy equation (2.15), the kinetic contribution term increases the free energy of the superconducting condensate. The circulating current, as a consequence of the fluxoid quantization, makes the superconducting state energetically less favorable. Hence, the critical temperature of the superconducting condensate decreases and the oscillations are periodic in the flux quantum Φ_0.

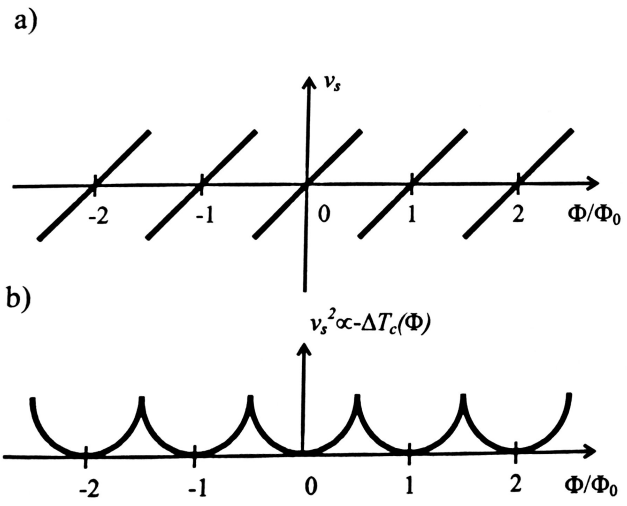

Fig. 5.6: *Variation of* ***(a)*** v_s *and* ***(b)*** v_s^2 *as a function of the flux threading a superconducting ring. Figure taken from [65]*

The critical temperature as a function of the applied field exhibits parabolic behavior, specific to thin strip conductors. Subtracting again the envelope of the form $f(H) = t_c\left[1 - c^2(\mu_0 H)^2\right]$, according to

the Tinkham formula (2.42), Figure 5.7 presents the shift in critical temperature between the envelope and the $0.5R_N$ contour line. Oscillations of the form $\Delta T_c \propto (n - \frac{\Phi_{ext}}{\Phi_0})^2$ [66] indicate the presence of currents flowing in a superconducting loop.

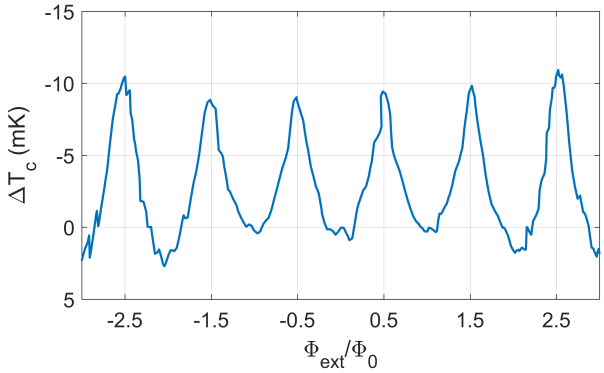

Fig. 5.7: *Shift of the critical temperature as a function of the applied flux Φ_{ext}. The period in field of the oscillation is found to be 3.10 ± 0.05 mT, resulting in an effective loop area of 0.67 ± 0.01 µm^2.*

The x-axis in Figure 5.7 is scaled to match the oscillation period of $T_c(\Phi)$, which is Φ_0 according to $\Delta T_c \propto (n - \frac{\Phi_{ext}}{\Phi_0})^2$, where n is an integer minimizing the shift in temperature. Matching the oscillations in applied field with integer and half integer values of the flux quanta allows us to calculate the effective area of the SQUID ($\Phi_0 = A_{eff}\Delta H$, with ΔH the period in the applied field). This procedure revealed an effective loop area of 0.67 ± 0.01 µm^2. Note that the area obtained from measurement is larger than the area obtained from the SEM image analysis (which was 0.31 ± 0.01 µm^2). This discrepancy can be explained by the fact that the dimensions of the nanopatterned loop structure are comparable to the penetration depth λ. It is an effect arising from to the mesoscale dimensions of our structure. Since the circulating supercurrents decay over a characteristic length scale λ, the currents are distributed over the whole width of the thin strip forming the loop. At the temperatures where the oscillations are observed, the penetration depth is much larger than the nanostructure, making the current density homogeneous over the width of the loop. A rough estimate of the effective area is found by averaging the area of the hole, or 'inner path' of the current, and an area representing the 'outer path' of the current. Considering the design of the micro-SQUID, the area enclosed by the 'outer path' is taken as 1×1 µm^2. The average of these area's (hole area and 'outer path' area) produce an estimate on the 'effective area' of 0.66 µm^2, in close agreement with the effective area used to match the measurement's periodicity to Φ_0 in Figure 5.7.

5.2.2 Critical Current

This section presents the experimental results of the virgin SQUID's critical current as a function of external field. All critical current data presented below are determined by taking $V(I)$ curves at different values of the applied magnetic field. The critical current of the SQUID as a function of externally applied field for different temperatures is presented in Figure 5.8 **(b)**, calculated as the contour line from the voltage versus applied current, $V(I)$, measurements presented in Figure 5.8 **(a)**.

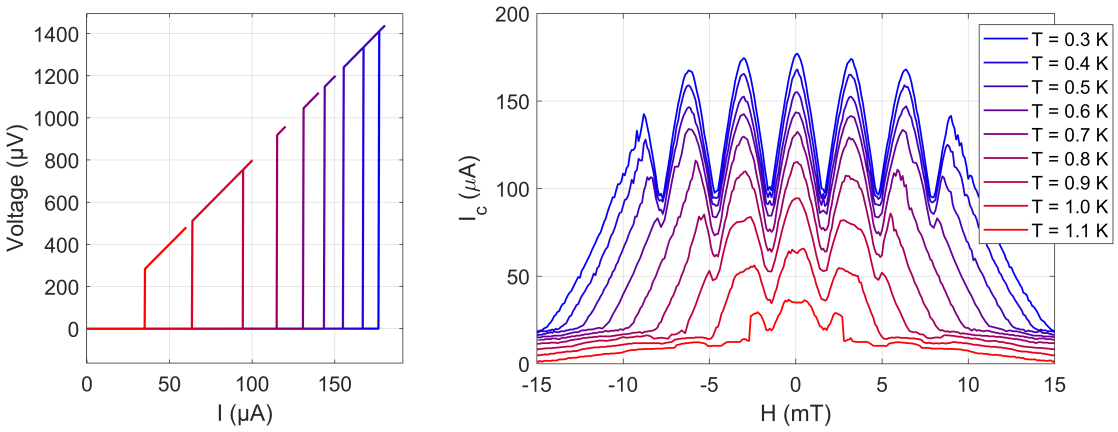

(a) ***(b)***

Fig. 5.8: ***(a)*** *$V(I)$ curves measured at zero applied magnetic field. The $I(V)$'s measured are performed while ramping up the current.* ***(b)*** *Critical current of the virgin SQUID as a function of externally applied field at different temperatures.*

Examples of the measured curves producing the contour lines in Figure 5.8 **(b)** are presented in Figure 5.8 **(a)**, without a magnetic field applied. These $V(I)$ show a sharp transition from superconducting to normal phase. This sharp transition is due to an avalanche effect of junction self-heating after a single phase slip event. The occurrence of a phase slip induces a voltage over the junction. Therefore, dissipation temporarily heats the junction, making the probability for a second phase slip to occur higher. The consequence is sharp transition due to an avalanche effect of phase slips, dissipating heat in the junction and suppressing the superconducting state. Statistical distributions of phase slip occurrence in 'bow-tie' junctions are extensively studied in [67].

The periodic behavior of the SQUID's critical current as a function of applied field is readily visible in Figure 5.8 **(b)**. The critical current is seen to oscillate with a period of 3.12 ± 0.04 mT. Furthermore, the critical current displays a parabolic envelope over the oscillations and a temperature dependent 'window'. Other interesting features include the 'flattening' of the peaks at lower temperatures.

Model Fitting

In order to compare the experimental data to the asymmetric model presented in Section 2.2.7, the measured data needs to be normalized. Figure 5.9 presents the same experiment as depicted in Figure 5.8 **(b)**. However, the critical current and applied field are normalized in Figure 5.9. To characterize the properties of the SQUID, the normalized measurements are fitted using the asymmetric SQUID model. Figure 5.10 **(a)** presents a fit example of the 0.3 K measurement of the virgin SQUID. From this fit, the oscillation period is 3.12 ± 0.04 mT, the alpha parameter $\alpha = 0.03 \pm 0.02$, $\beta_L = 1.02 \pm 0.04$ and $\eta = 0.01 \pm 0.03$. An envelope of the form $I_c(H) \propto (1 - cH^2)$ was multiplied with the model before fitting, with $c = 1.4 \cdot 10^3$. The errors are obtained using the χ^2 method.
The asymmetric SQUID model, given in Section 2.2.7, is fitted with the virgin SQUID data obtained at different temperatures, presented in Figure 5.8 **(b)**. The temperature dependence of the parameters are presented in Figure 5.10 **(b)**. The experimental data used to fit the model is taken in the interval

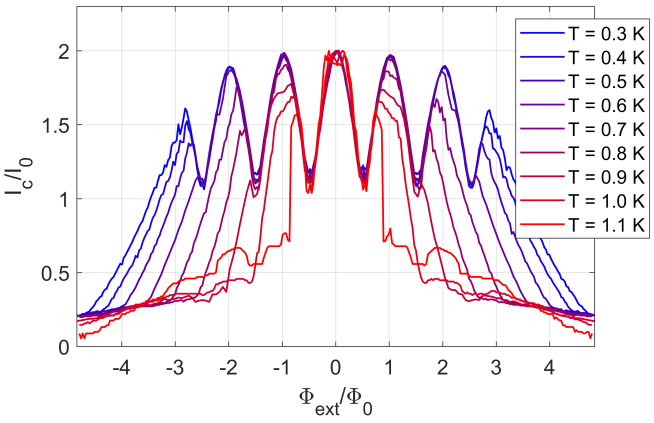

Fig. 5.9: *Normalized critical current of the virgin SQUID as a function of normalized applied flux threading the SQUID at different temperatures. The critical current of the SQUID is normalized to* I_0*. The flux was normalized using the effective area of the SQUID determined by the oscillation period. The oscillation period is* 3.12 ± 0.04 *mT, resulting in an effective area,* A_{eff}*, of* 0.66 ± 0.01 μm^2 *using* $\Delta \boldsymbol{H} \boldsymbol{A}_{eff} = \Phi_0$*.*

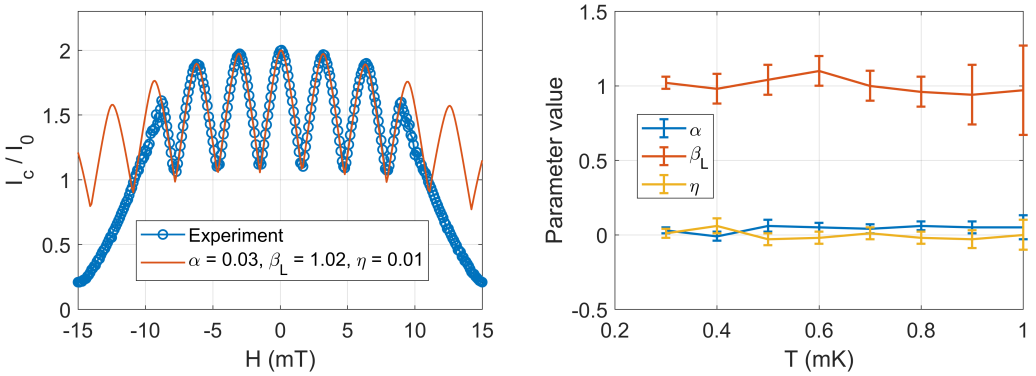

Fig. 5.10: ***(a)*** *Example of experimental data fitted with the asymmetric SQUID model. The experimental data are obtained from the virgin SQUID at* 0.3 *K.* ***(b)*** *Temperature dependence of the model parameters fitted with the critical current data obtained from the virgin SQUID. The fitting parameters are* $\alpha = 0.03$*,* $\beta_L = 1.02$ *and* $\eta = 0.01$

$[-\Phi_0; \Phi_0]$ to limit computation time and to exclude the temperature dependent window.

The simple model describing the asymmetric SQUID fits the experimental data well. All three parameters do not show any significant temperature dependency. Since the asymmetry parameters, α and η, are approximately zero, the SQUID, as fabricated, is symmetrical in its branches. Considering the in-situ electromigration experiment, discussed in Section 4.4, the asymmetry parameters will deviate from zero due to the asymmetrical void formation in the weak links. The next step in this investigation is to characterize the SQUID behavior after electromigration modifies the weak links.

5.3 Electromigrated SQUID Characterization

The previous chapter, Chapter 4, presented experimental evidence of localized void formation due to electromigration and hence reduction of the cross section in bow-tie shaped junctions. Even a parallel arrangement of bow-ties junctions, given in Section 4.4, demonstrated a reduction of the cross section in two bow-ties in parallel. In the context of the SQUID as a device, the electromigration process thus allows us to tune the weak links of our micro-SQUID. Applying the 'Pause and Play' feature of the electromigration software, the electromigration process was halted at certain values of resistance. Hereafter, the superconducting properties of the micro-SQUID were analyzed. Alternating between electromigration and characterizing the SQUID device allows us to study the effect of void formation in the weak links of the micro-SQUID.

5.3.1 Electromigration

Figure 5.11 **(a)** demonstrates the pause and play feature of the EM software. After each electromigration step, the SQUID's superconducting properties were characterized. A total of 10 electromigration steps were performed on one SQUID structure. The fifth electromigration shows two runs. However, it should be seen as one EM step, since SQUID characterization was only performed after the second EM5 run. Figure 5.11 **(b)** presents the measured conductance of the SQUID after each EM step.

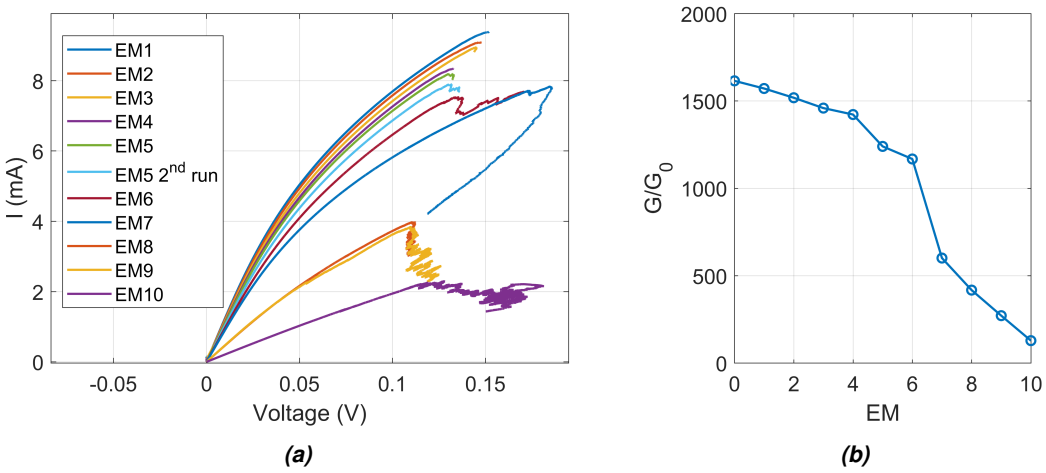

Fig. 5.11: (a) *$I(V)$ curve measured during each electromigration.* ***(b)*** *Conductance value measured after each EM step. EM0 corresponds to the virgin SQUID.*

The resistance values at which the software is halted, are chosen to create equidistant data points for the critical current of the micro-SQUID. However, this is not always achieved. The drop in conductance between EM6 and EM7 is an example of when this was not achieved. Examining the $I(V)$ curve, presented in Figure 5.11 **(a)**, the 'transition point', discussed in Section 4.2, is only seen in EM7. Considering the in-situ EM discussed in Section 4.4, it is plausible that only after the transition point in EM7, both weak links migrate simultaneously.

5.3.2 R(T) Measurements

After each electromigration step, resistance as a function of temperature is measured. These measurements are presented in Figure 5.12. The transition region in Figure 5.12 is observed to widen after each EM step. The phase slips introduced in Section 2.2.8 create this widening of the transition region. The electromigration process reduces the junction cross section, and hence the energy ΔF needed to induce a phase slip (equation (2.85)) is reduced.

These resistance as a function of temperature measurements confirm that the junctions' cross sections are indeed reduced. This can be seen in the increased resistance of the structure and the decrease of ΔF. Furthermore, the onset of superconductivity remains at the same critical temperature, indicating that the only the junction geometry is altered, not the superconducting parameters of aluminum.

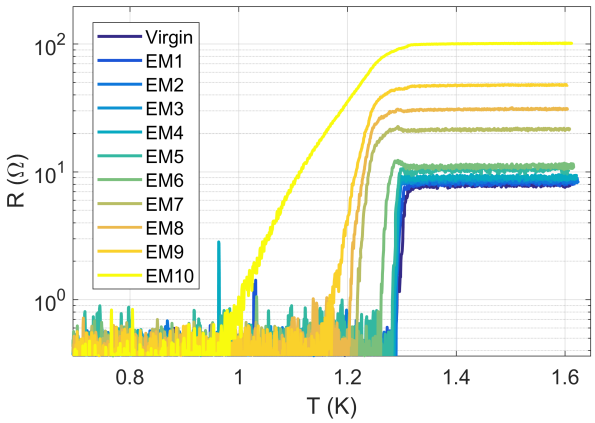

Fig. 5.12: *Measured resistance of the SQUID structure as a function of temperature.*

5.3.3 Critical Current

Figure 5.13 **(a)** presents the critical current as a function of field. The general trend after each EM step is the decrease in the overall critical current of the SQUID. Or, considering our asymmetric SQUID model, given in Section 2.2.7, a decrease in the Josephson junction critical current I_0. To characterize how our micro-SQUID evolves after each electromigration step, the experimental data are compared with the asymmetric SQUID model. The data presented in Figure 5.13 **(a)** are obtained at the lowest stable temperature of the Heliox, which is 0.3 K. Examples of the $V(I)$ curves measured at zero field are presented in Figure 5.13 **(b)**. Note that only after several electromigration steps, namely EM8, EM9 and EM10, the $I(V)$ curves become less sharp, indicative of low self-heating after a phase slip event due to a reduction in critical current; a single phase slip does not dissipate enough energy to create an avalanche of subsequent phase slips. Since for these last few electromigration steps there is no sharp transition observed in the $V(I)$ curves, special care has to be taken when defining the criterion for superconductivity. Figure 5.13 **(a)** presents the critical current with a criterion of $0.1R_N$.

Since the measurements from EM0 to EM7 present sharp transitions from superconducting to the

normal state, these will be examined first. For these superconducting measurements after EM0 to EM7, the choice of the superconducting resistance criterion does not influence the calculation of the critical current, due to the sharp transition. The EM8 to EM10 experimental data will be examined later in this chapter.

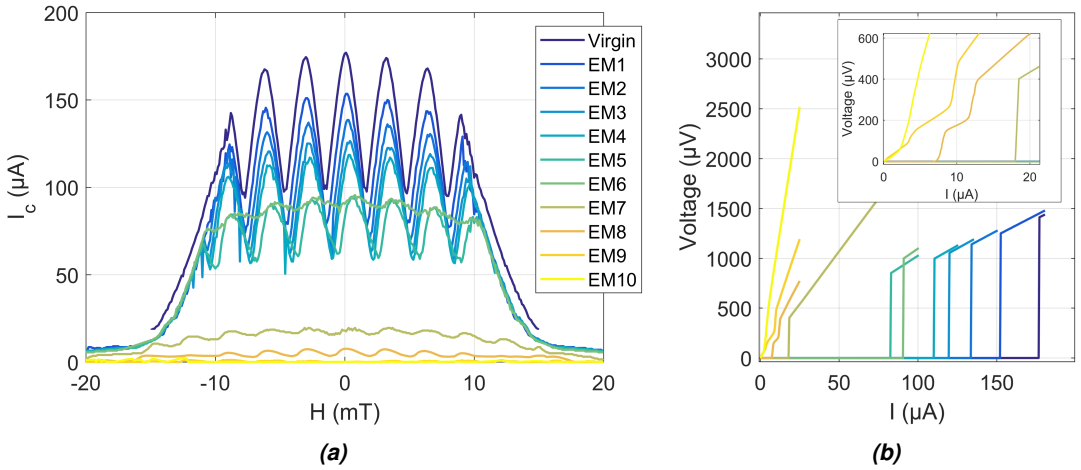

Fig. 5.13: ***(a)*** *SQUID critical current as a function of applied magnetic field.* ***(b)*** $I(V)$ *curves measured at zero applied magnetic field. The* $I(V)$*'s measured are performed while ramping up the current. The inset shows a zoom of the* $I(V)$*'s measured after EM7, 8, 9 and 10. Both figures make use of the same color code to indicate the EM step.*

Model Fitting

The results of the fitting parameters are presented in Figure 5.14 **(a)** after EM0 to EM7. An example of the model fit after EM5 is presented in Figure 5.14 **(b)**.

Critical Current After EM8, EM9 and EM10

Some interesting, color plots of the SQUID resistance as a function of applied magnetic field and current are presented in Figure 5.15. Interesting features to point out are the differences in shape of the oscillations at a low criterion (i.e. from blue to green regions) and at higher resistance criterion (i.e. from green to yellow). Also, considering $R(I)$ curves, a plateau can be seen, which was also visible in the $V(I)$ curves presented in the inset of Figure 5.13 **(b)**. The plateau's are also observed in the paper of X. Baumans *et al.* [67].

The broad transition region from the superconducting to the normal state complicates the interpretation of the critical current oscillations in field. Note that for a low criterion, about $0.1R_N$, the oscillations are still visible even for EM10, where the conductance of the weak links are only ~ 50 G_0. At a higher criterion the oscillations remain, but become more complex. In this dissipative, non-zero voltage, state, the presence of oscillations indicate there is still quantum interference in the SQUID. However, the analysis in the dissipative state, is beyond the scope of this thesis.

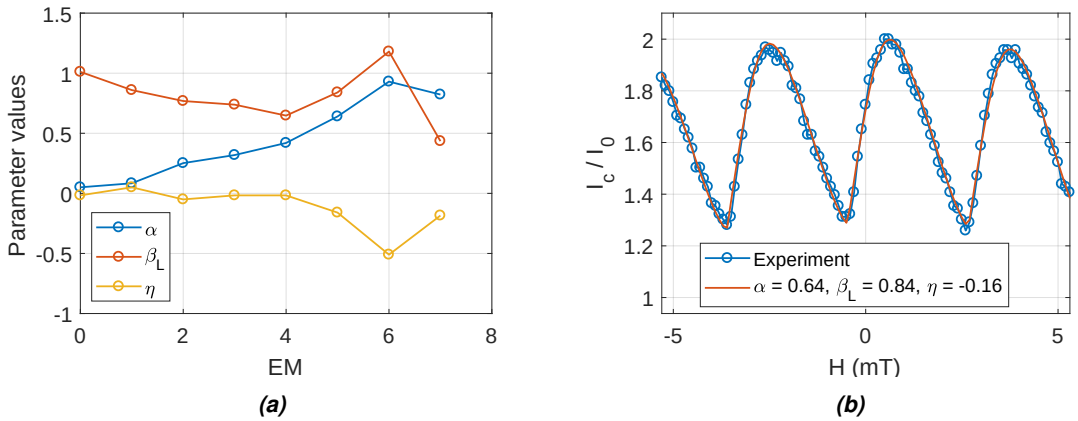

Fig. 5.14: ***(a)*** *Fitted parameters of the asymmetric model fit after EM step 0 through 7.* ***(b)*** *Example of a fit with the experimental data after EM5.*

SQUIDs in magnetometer applications are usually in the dissipative state, where they are used as a flux-to-voltage transducer. Using electromigration, a SQUID has been modified to be used in the dissipative state.

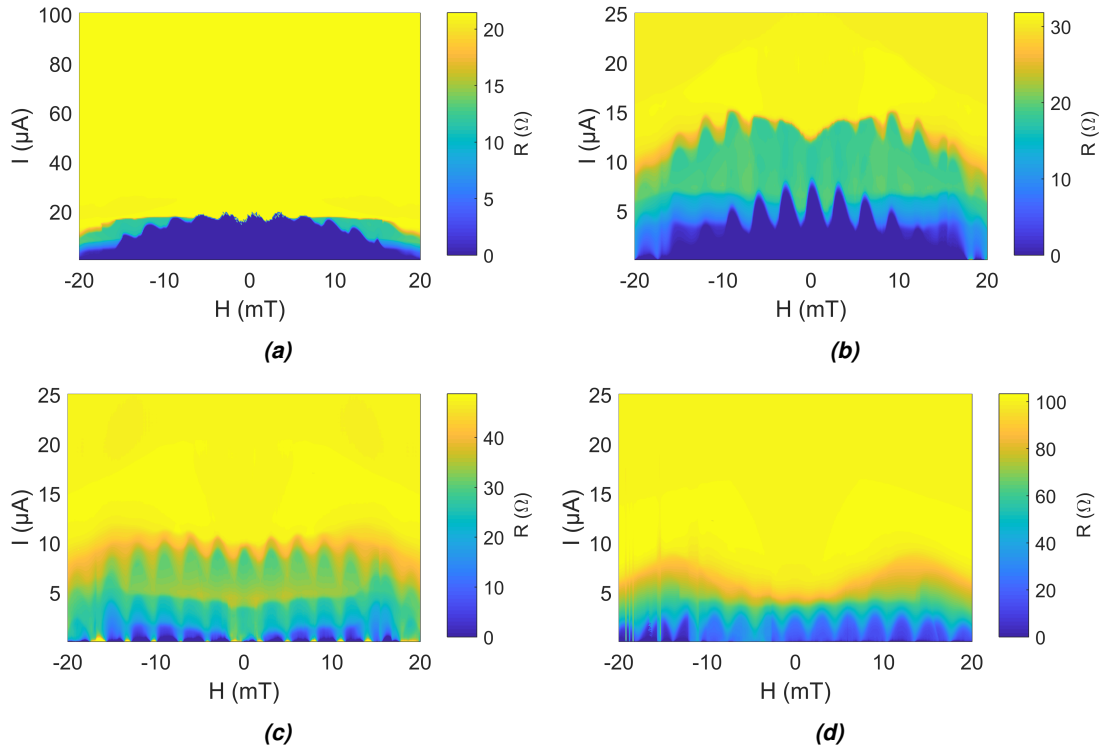

Fig. 5.15: *Color plots of the resistance as a function of applied magnetic field and current after* ***(a)*** *EM7,* ***(b)*** *EM8,* ***(c)*** *EM9 and* ***(d)*** *EM10.*

5.3.4 Critical Current Measurements and Model Comparison

Illustrated as an example in Figures 5.14 **(b)** and 5.10 **(b)**, the experimental data seems to fit the model well. However, one should interpret these fitted values with care.

An example of the pitfalls of fitting with a three parameter model is presented in Figure 5.16. Illustrated here are alternative values for α, β_L and η, fitting equally well to the experimental data after EM5 with respect to the fit presented in Figure 5.14 **(b)**. The conclusions taken from these fits have to be interpreted with care. Nevertheless, considering the gradual change in the weak link after each EM step, it is reasonable to fit the data and selecting a fit that does not significantly change all parameters from one step to the next. Furthermore, the asymmetry in α en η are expected to show opposite asymmetry; when the critical current of one junction is low with respect to the other junction, the inductance in that branch is high with respect to the other branch. This link between α en η will be explained further on in this discussion.

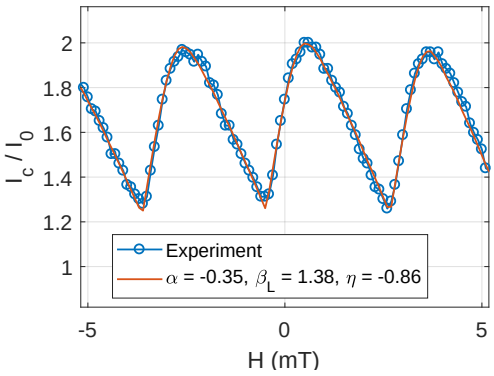

Fig. 5.16: *Alternative fit of the $I_c(H)$ curve after EM5.*

The gradual increase in asymmetry observed in the in-situ EM is also observed in measured $I_c(H)$ curves. The shift of the maximum in the $I_c(H)$ curves is an indicator of the presence of asymmetry. The fitted values for α and η quantify this asymmetry. This correspondence is another reason to have confidence in the fitted parameter values and the interpretation of the SQUID's evolution after each EM step.

5.3.5 Inductance Temperature Dependence

From Figure 5.10 **(a)**, presenting the model fit on the virgin SQUID at different temperatures, α and η remain constant around zero. This comes to no surprise since the asymmetry parameters are not expected to change when varying the temperature. Also, the SQUID was designed to be symmetrical. Remarkably, the β_L parameter also stays constant. Considering the definition of the inductance parameter given in equation 2.76, the inductance increases as the Josephson critical current, I_0, decreases with increasing temperature for a constant β_L. The critical current of the virgin SQUID as a function of temperature is plotted in Figure 5.17 **(a)**. From the definition of β_L, given in equation (2.76), the inductance of the SQUID can be calculated.

The temperature dependence of the inductance is presented in Figure 5.17 **(b)**. A rough calculation of the magnetic self inductance of a loop of similar size results in an estimated inductance value of 1 pH.

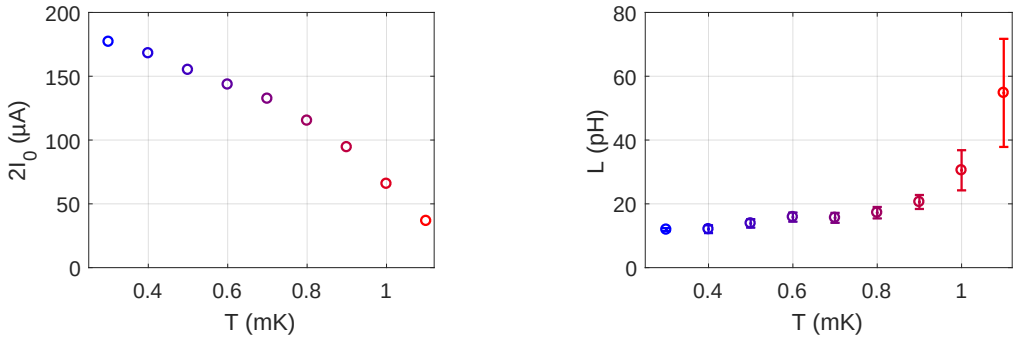

(a) ***(b)***

Fig. 5.17: ***(a)*** *Critical current of the SQUID as a function of temperature. These data are extracted from measurements presented in Figure 5.8* ***(a)****.* ***(b)*** *Inductance calculated from the β_L parameter fit and the critical current shown in* ***(a)****.*

The measured inductance cannot be explained by the geometric inductance alone on account of its temperature dependence and the discrepancy in quantitative value of an order of magnitude. There is another mechanism responsible for the SQUIDs inductance value and temperature dependence.

5.3.6 Mesoscale and Kinetic Inductance

The discussion held in Sections 2.2.6 and 2.2.7 regarding the equations determining the behavior of an (asymmetric) SQUID, started from the assumption to drop the last two integrals in equation (2.70). This is valid in the assumption that there exists a path in interior of the superconductor sufficiently far (with respect to the effective penetration depth λ_{eff}) from the surface. However, this is not the case in mesoscale structures, since its dimensions are on the order of quantities such as the penetration depth. The effective penetration depth in our device is on the order of a few microns, which is clearly larger than the thin strips forming the micro-SQUID Therefore, the integrals can not be neglected when dealing with mesoscale devices. These integrals contain the 'kinetic inductance' term.

Kinetic Inductance

In contrast to the magnetic self-inductance of a conductor as a consequence of Faraday's law, the kinetic inductance results from the inertia of a superconducting condensate resisting to a change of momentum. The magnetic self-inductance arises from the energy stored in the magnetic field created by a current. On the other hand, the kinetic inductance, L_K, arises form the kinetic energy stored in the motion of the superconducting electrons. Considering a superconducting wire, the kinetic inductance is calculated by equating the kinetic energy of the superfluid to an equivalent kinetic inductance, L_K [68]:

$$\frac{1}{2}(mv^2)(n_c l S) = \frac{1}{2}L_K I^2, \tag{5.2}$$

with n_c the Cooper pair density, v their velocity, l the length of the superconducting wire and S its cross section. The current can be written as $qn_c\boldsymbol{v}S$ and is found from the current density derived

earlier in this work (2.23). The kinetic inductance can thus be written as:

$$L_K = \frac{m^*}{2e^2 n_c}\frac{l}{S}, \tag{5.3}$$

where e is the charge of the electron and m^* its mass. Recalling the London coefficient, $\Lambda = m/(|\psi|^2 q^2)$, one can see that the kinetic inductance can be written as $L_K = \Lambda\frac{l}{A}$ or $L_K = \mu_0\lambda^2\frac{l}{A}$. One can note that the integral neglected in (2.70) are of the form L_K times a current.

The introduction of this kinetic inductance reveals the reason for the installation of the inductance asymmetry parameter, η, in the SQUID model. Electromigration of the weak links will significantly alter their geometry. According to equation (5.3), a change in length and cross section will affect the inductance of the SQUID. As a consequence, the process of electromigration introduces an asymmetry in the inductance in the two branches of the SQUID. Furthermore, the sign of α and η is expected to be opposite, since a decrease in cross section lowers the critical current but increase the kinetic inductance. Finally, note that the kinetic inductance, given in formula (5.3), shows temperature and current dependence arising from the density of Cooper pairs n_c.

Besides the temperature dependence, an order of magnitude estimate of the kinetic inductance produces a value on the order of 10 pH. This estimate is found using the London penetration depth for Al, $\lambda_L(0) = 16$ nm, the relation $\lambda(0) = \lambda_L(0)\sqrt{\xi_0/l}$, the scattering length found in section 5.1.3 and the estimated width and thickness of the SQUID loop. Both the order of magnitude and the temperature dependence of the inductance indicate the kinetic inductance dominates over the geometric.

Asymmetric SQUID Model with Dominating Kinetic Inductance

The integral terms in equation 2.70 contains the kinetic inductance. Since it was demonstrated from experiments and rough calculations of the upper limit of the geometric inductance value, that the geometric inductance is negligible compared to the kinetic inductance. The following equations describe an asymmetric SQUID where the geometric inductance, but not the kinetic, is negligible. Similar derivations as the asymmetric SQUID derivation performed in Section 2.2.7 are presented here. The main difference is the constraint between the phase differences used previously (equation (2.71)) and the true phase difference where the integrals are not neglected, given in equation 2.70. Equation 2.70 is rewritten using the definition of the kinetic inductance. These equations are derived by C. D. Tesche and J. Clarke [69].

$$\varphi_2^* - \varphi_1^* = 2\pi\frac{\Phi_{ext}}{\Phi_0} + \frac{2\pi}{\Phi_0}L_1 I_1 - \frac{2\pi}{\Phi_0}L_2 I_2 \tag{5.4}$$

Note that when the geometric inductance is negligible ($\beta_L \ll 1$), the external flux is the applied flux, which is directly implemented in the first term on the right hand side of equation (5.4). By introducing a similar β parameter, in this case due to the kinetic inductance, the equation giving the constraint on the phase difference across the junctions is obtained:

$$\varphi_2^* - \varphi_1^* = 2\pi\frac{\Phi_{ext}}{\Phi_0} + \pi\frac{\beta_K}{2}\left[(1-\alpha)(1-\eta)sin(\varphi_1^*) - (1+\alpha)(1+\eta)sin(\varphi_2^*)\right], \tag{5.5}$$

with the kinetic inductance parameters, β_K, defined as

$$\beta_K = \frac{2L_K I_0}{\Phi_0}. \tag{5.6}$$

The equation for the total current remains the same with respect to the model derived in Section 2.2.7:

$$I = I_1 + I_2 = I_{0,1} sin(\varphi_1^*) + I_{0,2} sin(\varphi_2^*) \,. \tag{5.7}$$

The two highlighted equations above (equations (5.5) and (5.7)) determine the behavior of SQUID featuring asymmetric Josephson junctions where the geometric inductance is negligible and the kinetic inductance dominates.

Solving these equations in Matlab produces exactly the same behavior for the SQUID's critical current in field as was presented in Section 2.2.7. All three parameters influence the $I_c(H)$ curves in exactly the same way as was illustrated in Figures 2.9 and 2.10. However, the difference between these models is their interpretation of the inductance origin and how these terms enter the SQUID equations. In this case, and in general, where the geometric inductance is negligible and the kinetic dominates, the model presented here in the discussion is a more correct interpretation. The temperature dependence of the inductance and the 'missing inductance' when only the geometric was considered, confirm that the kinetic inductance dominates in the micro-SQUID investigated here.

Chapter 6

Conclusion

This thesis is dedicated to the investigation of a thin film aluminum micro-SQUID, where its weak links are gradually broken down using controlled electromigration. The first step in this investigation is the design of the micro-SQUID. The design of the weak links, the main elements of a SQUID, are chosen to be of the same form as in the paper of Baumans *et al.* [38], in which these 'bow-tie' constrictions were already proven to be compatible with electromigration. Furthermore, no sharp corners were implemented to avoid electromigration at locations other than the constrictions. The main result for this particular design is that it is compatible with local void formation located at the constrictions due to EM.

The compatibility of the design with local electromigration is experimentally verified by in-situ electromigration experiments performed at L'Université de Liège, in the group of Alejandro V. Silhanek. Furthermore, these experiments revealed an asymmetry in the void formation; void nucleation is not observed simultaneously in the two junctions.

Besides the in-situ experiment, a second series of experiments were conducted. The superconducting phase boundary was probed by varying temperature, applied magnetic field and current. The observed asymmetry measured in these low temperature measurements corresponds to the observed asymmetry in the in-situ EM measurement. Furthermore, the behavior of the SQUID's critical current in field can be understood from the numerical calculations of the asymmetric SQUID model while taking into account the kinetic inductance.

The aforementioned low temperature measurements indicated that the properties of a SQUID can be modified via electromigration. Such modifications include the reduction of the weak link critical current, the introduction of asymmetry and the modification of the inductance parameter, an important parameter describing the SQUIDs performance. Moreover, it is observed that when electromigration has sufficiently reduced the junction cross section, thermal effects are reduced and the SQUID can be operated in the dissipative state, where magnetic flux readout from voltage is possible. Hence, electromigration provides a 'knob' to tune the SQUID's parameters.

Outlook

Sparked by the pioneering work performed in this thesis, theoretical simulations, performed at the University of Antwerp, will provide a better insight into the behavior of the SQUID as the junctions cross sections is reduced. Furthermore, niobium micro-SQUIDs are being investigated at the time

of writing by Joseph Lombardo, a PhD student at L'Université de Liège. The design used for these niobium micro-SQUIDs is the design created in the framework of this thesis. Since niobium and aluminum have vastly different superconducting parameters, it is interesting to compare these two experiments and observe how these parameters affect the SQUID's behavior. To quantify the noise, performance and sensitivity of these SQUIDs and how this evolves as the EM process modifies the weak link is, in my humble opinion, the next topic that would be interesting to investigate.

Moreover, when the center of interest is pivoted from superconductivity to electromigration, superconductivity provides an interesting and powerful method to study the physics of parallel electromigration. Using the interference effect of the SQUID, the evolution of both junctions after an electromigration step can be investigated. Here, superconductivity is viewed as a 'tool' to study electromigration.

Appendices

Appendix A

Asymmetric SQUID with $\beta_L \ll 1$

Described in this appendix is a short analytical derivation of the critical current dependence on the applied field for an asymmetric SQUID with small inductance parameter ($\beta_L \ll 1$). From this 'small β_L' condition follows that the flux through the SQUID loop is approximately equal to the externally applied flux ($\Phi \approx \Phi_{ext}$). The critical currents of the Josephson junctions are labeled as $I_{0,1}$ and $I_{0,2}$. The total current flowing across the SQUID in the zero voltage state can be written as

$$I = I_{0,1}sin(\varphi^*) + I_{0,2}sin(\varphi^* + 2\pi\frac{\Phi_{ext}}{\Phi_0}), \tag{A.1}$$

with φ^* the gauge invariant phase difference over one junction and Φ_{ext} the applied flux.

In order to find the maximum supercurrent across the SQUID, one can find the maximum of equation (A.1) with respect to φ^*. Therefore, the derivative $dI/d\varphi^*$ must equal zero. This condition produces a second equation.

$$I_{0,1}cos(\varphi^*) + I_{0,2}cos(\varphi^* + 2\pi\frac{\Phi_{ext}}{\Phi_0}) = 0, \tag{A.2}$$

A possible first steps towards solving this problem is squaring the two equations (A.1),(A.2). This produces

$$I^2 = I_{0,1}^2sin^2(\varphi^*) + 2I_{0,2}I_{0,1}sin(\varphi^*)sin(\varphi^* + 2\pi\frac{\Phi_{ext}}{\Phi_0}) + I_{c2}^2sin^2(\varphi^* + 2\pi\frac{\Phi_{ext}}{\Phi_0}) \tag{A.3}$$

and

$$I_{0,1}^2cos^2(\varphi^*) + 2I_{0,2}I_{0,1}cos(\varphi^*)cos(\varphi^* + 2\pi\frac{\Phi_{ext}}{\Phi_0}) + I_{0,2}^2cos^2(\varphi^* + 2\pi\frac{\Phi_{ext}}{\Phi_0}) = 0 \tag{A.4}$$

Next, using the Pythagorean trigonometric identity, $cos^2(\alpha)$ in the last term of equation (A.4) is written as $1 - sin^2(\alpha)$. Using this identity, (A.4) reads

$$I_{c2}^2sin^2(\varphi^* + 2\pi\frac{\Phi_{ext}}{\Phi_0}) = I_{0,1}^2cos^2(\varphi^*) + I_{0,2}^2 + 2I_{0,2}I_{0,1}cos(\varphi^*)cos(\varphi^* + 2\pi\frac{\Phi_{ext}}{\Phi_0}). \tag{A.5}$$

The equation above can now readily be substituted in the last term of equation (A.3). Performing the substitution and using the trigonometric identity $cos(\alpha-\beta) = cos(\alpha)cos(\beta)+sin(\alpha)sin(\beta)$, equation

(A.3) reads

$$I^2 = I_{0,1}^2 + I_{0,2}^2 + 2I_{0,1}I_{0,2}cos(2\pi\frac{\Phi_{ext}}{\Phi_0}). \tag{A.6}$$

By using a second trigonometric identity, namely $cos^2(\alpha) = \frac{1+cos(2\alpha)}{2}$, previous equation is written as

$$I^2 = I_{0,1}^2 + I_{0,2}^2 + 4I_{0,1}I_{0,2}cos^2(\pi\frac{\Phi_{ext}}{\Phi_0}) - 2I_{0,1}I_{0,2}, \tag{A.7}$$

which can be worked out further to yield the final result:

$$I = \sqrt{(I_{0,1} - I_{0,2})^2 + 4I_{0,1}I_{0,2}cos^2(\pi\frac{\Phi_{ext}}{\Phi_0})}. \tag{A.8}$$

Presented here in equation (A.8) is the maximum supercurrent across a 'small β_L' SQUID with asymmetric Josephson junctions at a given external field. The result agrees with the literature [70, 71].

Appendix B

SQUID Structure Normal Resistance

This appendix provides a method to estimate resistivity calculated from the measured normal resistance and thickness of the structure. From introductory physics textbooks, the resistance of a conductor in introduced as $R = \rho\frac{l}{A}$, with ρ the resistivity of the conductor, l its length and A its cross section, with respect to the current flow. Broadening this formula to an arbitrary geometry produces $R = \rho\int\frac{dx}{A(x)}$, integrating over the whole length of the conductor. In the context the thin films studied in this work, the thickness is constant. The resistance formula of a thin film calculated from geometry and resistivity is:

$$R = \frac{\rho}{t}\int\frac{dx}{w(x)}, \tag{B.1}$$

where t is the thin film thickness and w its width perpendicular to the current flow. Next step is to solve the integral in equation B.1. Since the geometry of the thin film structure is known (described in Section 4.1.1), the integral can be calculated and produces a dimensionless scalar. Figure B.1 presents the geometry of the structure schematically.

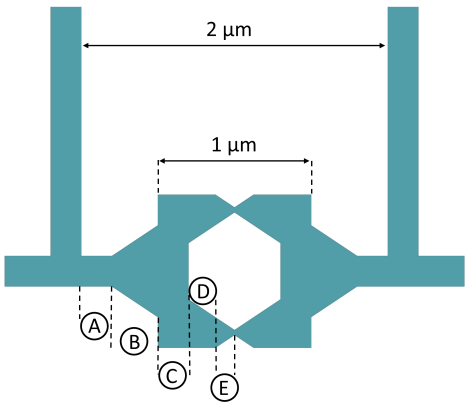

Fig. B.1: *Geometry of the thin film aluminum SQUID. The structure is fragmented into 5 pieces which are individually easy to integrate, labelled as* Ⓐ through Ⓔ.

Also indicated on Figure B.1 are the sections labelled protect Ⓐ through Ⓔ. The total resistance, taking into account the mirror symmetry around the central vertical line and the parallel connections Ⓓ and Ⓔ, reads

$$R = \frac{\rho}{t}\left(2\int_{Ⓐ} + 2\int_{Ⓑ} + 2\int_{Ⓒ} + \int_{Ⓓ} + \int_{Ⓔ}\right)\frac{dx}{w(x)}. \tag{B.2}$$

Substituting the correct $w(x)$ at each section allows to calculate the dimensionless integral. Doing these calculations using the geometry description in section 4.1.1, the resistance is found to be

$$R = (2 + 1.648 + 2/5 + 0.689 + 1.344)\frac{\rho}{t} = 6.081\frac{\rho}{t}. \tag{B.3}$$

The method to find the resistivity described above is similar to the method used in [38] to find the resistivity of single junctions. To demonstrate this similarity, a formula for the resistance of the junction itself will be calculated, where the junction resistance is defined as double the resistance in the region indicated by Ⓔ. The integral that is needed to solve in this situation is

$$\int_0^{a/2} \frac{dx}{w_0 + \frac{w_1 - w_0}{a/2}x}, \tag{B.4}$$

where the parameters a, w_1 and w_0 can be found in Figure 4.1. Solving the integral results in

$$R = \frac{\rho}{t}\left[\frac{a}{w_1 - w_0} ln\left(\frac{w_1}{w_0}\right)\right], \tag{B.5}$$

corresponding to the result found in [38]. Filling in the dimensions used in this work, the junction resistance is found:

$$R_j = 2.688\frac{\rho}{t}. \tag{B.6}$$

Bibliography

[1] R. C. Jaklevic, John Lambe, A. H. Silver, and J. E. Mercereau. Quantum interference effects in Josephson tunneling. *Physical Review Letters*, 12(7):159–160, 1964.

[2] D. Halbertal, J. Cuppens, M. Ben Shalom, L. Embon, N. Shadmi, Y. Anahory, H. R. Naren, J. Sarkar, A. Uri, Y. Ronen, Y. Myasoedov, L. S. Levitov, E. Joselevich, A. K. Geim, and E. Zeldov. Nanoscale thermal imaging of dissipation in quantum systems. *Nature*, 539(7629):407–410, 2016.

[3] B.D. Josephson. Possible new effects in superconductive tunnelling. *Physics Letters*, 1(7):251–253, 1962.

[4] H. D. Hahlbohm and H. LuÌĹbbig. *SQUID '80, superconducting quantum interference devices and their applications : proceedings of the Second International Conference on Superconducting Quantum Devices, Berlin (West), May 6-9, 1980*. W. de Gruyter, 1980.

[5] C. P. Foley and H. Hilgenkamp. Why NanoSQUIDs are important: an introduction to the focus issue. *Superconductor Science and Technology*, 22:064001, 2009.

[6] A. Scorzoni, B. Neri, C. Caprile, and F. Fantini. Electromigration in thin-film interconnection lines: models, methods and results. *Materials Science Reports*, 7(4-5):143–220, 1991.

[7] D.G. Pierce and P.G. Brusius. Electromigration: A review. *Microelectronics Reliability*, 37(7):1053–1072, 1997.

[8] R. L. de Orio, H. Ceric, and S. Selberherr. Physically based models of electromigration: From Black's equation to modern TCAD models. *Microelectronics Reliability*, 50(6):775–789, 2010.

[9] R. L. de Orio. *Electromigration Modeling andSimulation*. PhD thesis, TU Wien, 2010.

[10] P. Drude. Zur Elektronentheorie der Metalle. *Annalen der Physik*, 354(6):710–724, 1916.

[11] K. Sasagawa and M. Saka. *Metallic Micro and Nano Materials*. 2011.

[12] H.B. Huntington and A.R. Grone. Current-induced marker motion in gold wires. *Journal of Physics and Chemistry of Solids*, 20(1):76–87, 1961.

[13] J. R. Black. Mass Transport of Aluminum by Momentum Exchange with Conducting Electrons. *6th Annual Reliability Physics Symposium (IEEE)*, (7):1–6, 1967.

[14] J.R. Black. Electromigration - A Brief Survey and Some Recent Results. *IEEE Transactions on Electron Devices*, 16(4):338–347, 1969.

[15] D. E. Johnston, D. R. Strachan, and A. T. C. Johnson. Parallel fabrication of nanogap electrodes. *Nano Letters*, 7(9):2774–2777, 2007.

[16] P. Müller, I.V. Grigorieva, V.V. Schmidt, and A.V. Ustinov. *The Physics of Superconductors: Introduction to Fundamentals and Applications*. Springer Berlin Heidelberg, 2013.

[17] M. Tinkham. *Introduction to superconductivity*. McGraw Hill, New York, 1996.

[18] C.P. Poole, H.A. Farach, and R.J. Creswick. *Superconductivity*. Elsevier Science, 2013.

[19] W. Buckel and R. Kleiner. *Superconductivity: Fundamentals and Applications, a text book*. 2004.

[20] H. K. Onnes. The resistance of pure mercury at helium temperatures. *Commun. Phys. Lab. Univ. Leiden*, 12(120):1, 1911.

[21] W. Meissner and R. Ochsenfeld. Ein neuer Effekt bei Eintritt der Supraleitfhigkeit. *Die Naturwissenschaften*, 21(44):787–788, 1933.

[22] F. and H. London. The electromagnetic equations of the supraconductor. *Proc. Roy. Soc.*, A149(71), 1935.

[23] L. Landau V. Ginzburg. On the theory of superconductivity. *Zh. Eksp. Teor. Fiz.*, 20(1064), 1950.

[24] J. Bardeen, L. N. Cooper, and J. R. Schrieffer. Theory of superconductivity. *Physical Review*, 108(5):1175–1204, 1957.

[25] L. P. Gor'kov. Microscopic Derivation of the Ginzburg-Landau Equations in the Theory of Superconductivity. *Soviet Physics Journal of Experimental and Theoretical Physics*, 36(9):1364–1367, 1959.

[26] R. Doll and M. Näbauer. Experimental proof of magnetic flux quantization in a superconducting ring. *Physical Review Letters*, 7(2):51–52, 1961.

[27] B. S. Deaver and W. M. Fairbank. Experimental evidence for quantized flux in superconducting cyclinders. *Physical Review Letters*, 7(2):43–46, 1961.

[28] V. V. Moshchalkov and J. Fritzsche. *Nanostructured Superconductors*. 2010.

[29] V. V. Moshchalkov. Effect of sample topology on the critical fields of mesoscopic superconductors. *Nature*, 1995.

[30] R. B. Dingle. Some Magnetic Properties of Metals. I. General Introduction, and Properties of Large Systems of Electrons. *Proceedings of the Royal Society of London A: Mathematical, Physical and Engineering Sciences*, 211(1107):500–516, 1952.

[31] J. Pearl. Current distribution in superconducting films carrying quantized fluxoids. *Applied Physics Letters*, 5(4):65–66, 1964.

[32] R.P. Feynman. *THE FEYNMAN LECTURES ON PHYSICS, Vol III, Quantum Mechanics*. Addison-Wesley Publishing Company, Inc., 1965.

[33] K. K. Likharev. Superconducting weak links. *Reviews of Modern Physics*, 51(1):101–159, 1979.

[34] R. De Bruyn Ouboter and A. Th. A. M. De Waele. Superconducting point contacts weakly connecting two superconductors. *Revue de physique appliquée*, 5(1):25–31, 1970.

[35] G. J. Podd, G. D. Hutchinson, D. A. Williams, and D. G. Hasko. Micro-SQUIDs with controllable asymmetry via hot-phonon controlled junctions. *Physical Review B - Condensed Matter and Materials Physics*, 75(13):1–13, 2007.

[36] K. Yu Arutyunov, D. S. Golubev, and A. D. Zaikin. Superconductivity in one dimension. *Physics Reports*, 464(1-2):1–70, 2008.

[37] W. A. Little. Decay of persistent currents in small superconductors. *Physical Review*, 156(2):396–403, 1967.

[38] X. D. A. Baumans, D. Cerbu, O. Adami, V. S. Zharinov, N. Verellen, G. Papari, J. E. Scheerder, G. Zhang, V. V. Moshchalkov, A. V. Silhanek, and Joris Van de Vondel. Thermal and quantum depletion of superconductivity in narrow junctions created by controlled electromigration. *Nature communications*, 7:10560, 2016.

[39] S. K. Dew and M. Stepanova. *Nanofabrication: Techniques and Principles*. Springer-Verlag Wien, 1 edition, 2012.

[40] eline plus - electron beam lithography, imaging and nanoengineering| raith.com. https://www.raith.com/products/eline-plus.html. (Accessed on 12/29/2016).

[41] Molecular beam epitaxy, institute for nuclear and radiation physics. https://fys.kuleuven.be/iks/nvsf/experimental-facilities/molecular-beam-epitaxy. (Accessed on 12/30/2016).

[42] Experimental facilities, institute for nuclear and radiation physics. https://fys.kuleuven.be/iks/nvsf/experimental-facilities. (Accessed on 12/29/2016).

[43] AFM Manual Parks Systems. Xe-100. 2002.

[44] R. Egerton. *Physical Principles of Electron Microscopy An Introduction to TEM SEM and AEM*. Springer, 2008.

[45] J. W. Mayer T. L. Alford, L.C. Feldman. *Nanoscale Thin Film Analysis: Fundamentals and Techniques*. Springer, 1 edition, 2007.

[46] Pioneer - the perfect ebl sem hybrid | raith.com. https://www.raith.com/products/pioneer.html. (Accessed on 03/15/2017).

[47] W.D. Van Driel, R.B.R. Van Silfhout, and G.Q. Zhang. Reliability of wirebonds in micro-electronic packages. *Microelectronics International*, 25:15–22, 2008.

[48] Wire Bonder. Kulicke and Soffa Model 4526 Wire Bonder Users Manual. pages 1–16.

[49] R. M. Murray and K. J. Aström. *Feedback Systems: An Introduction for Scientists and Engineers*. 2010.

[50] Quantum Design. Physical Property Measurement System (PPMS®.) . http://www.qdusa.com/products/ppms.html. Accessed: 2016-11-15.

[51] CA 92121 Quantum Design. 6325 Lusk Boulevard, San Diego. Physical Property Measurement System: Hardware Manual. *Part Number 1070-150, B5*.

[52] J. Scheerder. Spin dynamics in non-local spin valves, 2014.

[53] Oxford instruments helium3 refrigerator with sorption pump helioxvl - oxford instruments. https://www.oxford-instruments.com/products/cryogenic-environments/dilution-refrigerator/3he-inserts/helium-3-refrigerator-with-sorption-pump-helioxvl. (Accessed on 01/30/2017).

[54] J. Van de Vondel. *Vortex dynamics and rectification effects in superconducting films with periodic asymmetric pinning*. PhD thesis, KU Leuven, 2007.

[55] SRS. About Lock-In Amplifiers. *Application Note*, (408):1–9, 2011.

[56] Ametek Signal Recovery. 7225 DSP Lock-in Amplifier, Manual.

[57] F. B. Hagedorn and P. M. Hall. Right-angle bends in thin strip conductors. *Journal of Applied Physics*, 34(1):128–133, 1963.

[58] W. Jeong, K. Kim, Y. Kim, W. Lee, and P. Reddy. Characterization of nanoscale temperature fields during electromigration of nanowires. *Scientific Reports*, 4:1–6, 2014.

[59] J. M. Campbell and R. G. Knobel. Feedback-controlled electromigration for the fabrication of point contacts. *Applied Physics Letters*, 102(2):1–5, 2013.

[60] M. L. Trouwborst, S. J. Van Der Molen, and B. J. Van Wees. The role of Joule heating in the formation of nanogaps by electromigration. *Journal of Applied Physics*, 99(11), 2006.

[61] A. E. Vladár, K. P. Purushotham, and M. T. Postek. Contamination specification for dimensional metrology SEMs. *Proceedings of SPIE*, 6922(or 50):692217, 2008.

[62] J. Romijn, T. M. Klapwijk, M. J. Renne, and J. E. Mooij. Critical pair-breaking current in superconducting aluminum strips far below Tc. *Physical Review B*, 26(7):3648–3655, 1982.

[63] P. G. De Gennes. *Superconductivity of Metals and Alloys*. Advanced book classics. Perseus, Cambridge, MA, 1999.

[64] F. R. Fickett. A review of resistive mechanisms in aluminum. *Cryogenics*, 11(5):349–367, 1971.

[65] D. Golubović. *Nucleation of superconductivity and vortex matter in superconductor/ferromagnet nanoconstrictions*. PhD thesis, KU Leuven, 2005.

[66] R. P. Groff and R. D. Parks. Fluxoid quantization and field-induced depairing in a hollow superconducting microcylinder. *Physical Review*, 176(2):567–580, 1968.

[67] X.D.A. Baumans, V.S. Zharinov, E. Raymenants, S.B. Alvarez, J.E. Scheerder, J. Brisbois, D. Massarotti, R. Caruso, F. Tafuri, E. Janssens, V.V. Moshchalkov, J. Van De Vondel, and A.V. Silhanek. Statistics of localized phase slips in tunable width planar point contacts. *Scientific Reports*, 7:1–12, 2017.

[68] A. J. Annunziata, D. F. Santavicca, L. Frunzio, G. Catelani, M. J. Rooks, A. Frydman, and D. E. Prober. Tunable superconducting nanoinductors. *Nanotechnology*, 21(44):445202, 2010.

[69] C. D. Tesche and J. Clarke. Dc squid: noise and optimization. *Journal of Low Temperature Physics*, 29(3):301–331, 1977.

[70] C. Granata and A. Vettoliere. Nano Superconducting Quantum Interference device: A powerful tool for nanoscale investigations. *Physics Reports*, 614:1–69, 2016.

[71] G Aviv. Superconducting Quantum Interference Devices 1. *SQUIDs- Superconducting Quantum Interference Devices*, pages 1–9, 2008.

DEPARTEMENT OF PHYSICS AND ASTRONOMY
Celestijnenlaan 200d bus 2412
3001 HEVERLEE, BELGIË
tel. + 32 16 32 71 24
fys.kuleuven.be